

EVALUATION OF SURFACE ROUGHNESS AND BOND-SLIP BEHAVIOR OF NEW
TEXTURED EPOXY-COATED REINFORCING BARS

BY

ZIGE ZHANG

THESIS

Submitted in partial fulfillment of the requirements
for the degree of Master of Science in Civil Engineering
in the Graduate College of the
University of Illinois at Urbana-Champaign, 2020

Urbana, Illinois

Adviser:

Professor Bassem Andrawes

ABSTRACT

Epoxy-coated reinforcing bars are widely used in bridge decks to mitigate the corrosion of reinforcing steel. Research and practical experience both showed that the smooth epoxy coating significantly reduces the bond between concrete and reinforcing steel, which often results in the early development of transverse cracks in bridge decks. To solve this problem, the Illinois Department of Transportation (IDOT) proposed a new type of textured epoxy-coated (TEC) reinforcing bars with applied roughness to improve the bond between concrete and steel while providing corrosion protection. This study investigates the surface roughness of different types of TEC bars and how it impacts the bar's bond-slip behavior with concrete, both experimentally and numerically. First, the surface roughness of the TEC bars is compared with that of uncoated black bars (BLK) using 2-D and 3-D roughness parameters. Second, direct pull-out tests are conducted on concrete specimens with embedded 1) BLK, 2) smooth epoxy-coated (SEC), and 3) different types of TEC bars to compare their bond characteristics. Then, multiple 3-D finite element models are developed and calibrated to simulate the bond-slip behavior of TEC bars embedded in concrete and to determine the development length of TEC bars. The numerical development length of the TEC bars is then compared with the values recommended by the American Concrete Institute and the American Association of State Highway and Transportation Officials for SEC and BLK bars. Finally, a large-scale laboratory control experiment is designed to observe the impact of the TEC bars on bridge deck shrinkage compared with that of the SEC bars.

ACKNOWLEDGEMENTS

First, I want to thank my advisor, Dr. Andrawes, for his continuous support during my two years of graduate thesis research at the University of Illinois at Urbana-Champaign. Two years ago I almost knew nothing about research, but now I have designed and conducted a series of experiments and studies, published a paper, and gained invaluable research experience. Without his support, none of these would have happened.

I also want to thank Dr. Greg Banas, Don Marrow, Jamar Brown, Tim Prunkard, and everyone else at the machine shop for assisting me in conducting laboratory experiments. I also acknowledge that the Illinois Department of Transportation funded this project.

In addition, I want to extend my gratitude to my colleagues Donghyuk(DK) Jung, Minsoo Sung, Pratik Deogekar, Ernesto Perez, and Isaias Colombani. I want to acknowledge here that DK contributed significantly to developing the quantification method of the rebar surface roughness discussed in Chapter 3. He also kindly provided me guidance in the first few months of my research. My two undergraduate assistants, Emma Sun and Ryan Halton, were also of great help for my research.

Finally, I want to sincerely thank my mom and all my friends who supported me during this chapter of my life with their encouragement, friendship, and love, including Aissa Maiga, Stephen Hsiao, Yen-Feng Chen, Jin Liu, Sherry Yang, Jingyi Yan, Abby Smith, Gloria Frank, Sunny Zhou, Samun Khalilian, and Vardhan Dongre.

TABLE OF CONTENTS

Chapter 1: Introduction	1
Chapter 2: Literature Review	5
Chapter 3: Characterization of the Surface Roughness of TEC Rebars	38
Chapter 4: Pull-Out Tests of Coated and Uncoated Bars	69
Chapter 5: Finite Element Analysis of Interfacial Bond between TEC Bars and Concrete	87
Chapter 6: Shrinkage Test Design of Bridge Deck Reinforced with TEC Bars	114
Chapter 7: Conclusions	135
References	138
Appendix A: Rebar Surface Roughness Parameter Values	146
Appendix B: Pull-Out Test Data	149

Chapter 1: Introduction

1.1 Motivation

The US bridges received a grade of C+ according to the American Society of Civil Engineer (ASCE)'s Infrastructure Report Card issued in 2017 (American Society of Civil Engineers, 2017). This grade indicated that the infrastructure had shown general signs of deterioration with some elements exhibiting significant deficiencies and being more susceptible to risk (American Society of Civil Engineers, 2017). Bridge deck cracking remains a major concern in the United States. Research showed that increased cracking was observed in recent years on newly constructed highway bridges (Lindquist et al, 2006; Bentz et al, 2012). Although structural cracking is common during construction, cracks caused by restrained shrinkage, and temperature gradient between the concrete and the supporting girders have detrimental effects on the structure. Bridge deck cracks increase the susceptibility of the deck to steel corrosion, resulting in a decrease of the serviceability and service life of bridges (Lindquist et al, 2006; Otieno et al, 2010; Hopper et al, 2015).

Despite the popularity of the use of epoxy-coated reinforcement as a corrosion mitigating measure, a major side effect of applying the epoxy coating is the considerable reduction in the bond strength between steel bars and surrounding concrete. This reduction is attributed to the smoother surface of the coated bar and the change of the originally sharp and well-defined corners of the rebar ribs to more rounded corners and edges due to the application of epoxy (Treece & Jirsa, 1989; Mathey & Clifton, 1976; Choi et al, 1991). Currently, the most prevalent solution to make up for the decreased bond strength is to adopt a modification factor to increase the reinforcement development length during the design phase (ACI Committee 318, 2019).

To protect the steel reinforcement more cost-effectively, without compromising the bond strength with concrete, the Illinois Department of Transportation (IDOT) started exploring the application of a new type of epoxy-coated rebars known as TEC rebars. TEC rebars are manufactured by applying an additional layer of polymeric powder, which roughens the surface of the epoxy coating. If the TEC reinforcement performs as expected, it can help save the cost of additional development lengths of reinforcement and control bridge deck cracking. However, in recently constructed TEC-bar-reinforced bridges in Illinois, transverse cracks developed through the entire deck width (see Fig 1.1). These cracks were observed at the early stages after construction. To investigate the cause of these cracks, the impact of the applied surface roughness of the rebars needed to be thoroughly investigated. A preliminary study was conducted by Kim and Andrawes (2019) compared the bond-slip behavior of No. 5 and No. 8 TEC rebars with that of black (BLK) bars and smooth epoxy-coated (SEC) bars through direct pull-out tests and flexure tests. However, despite the conclusions of the study by Kim and Andrawes (2019), it was still unclear how the surface roughness and profile of TEC bars impact their interfacial bond-slip behavior with concrete. This research aimed to address this issue experimentally and numerically.



Fig 1.1: Transverse cracks at the bottom of a bridge on Interstate 55 at East St. Louis, IL.

1.2 Thesis Outline

This thesis presents the objective, methodology, and results of the research about the impact of textured epoxy-coated rebars on the bond-slip behavior of bridge decks conducted at the University of Illinois at Urbana-Champaign, supported by the Illinois Department of Transportation. This research is the continuation of the exploratory study by Kim and Andrawes (2019) to comprehensively investigate the effect of difference types of surface roughness on reinforcing bars.

Chapter 2 is a literature review introducing the causes of transverse bridge deck cracking and several crack mitigating measures. It also discusses the development of the use of epoxy-coated bars in bridge decks through the experimental results from multiple studies and a previous study about the use of textured epoxy-coated rebar.

Chapter 3 discusses the methodology of quantitatively measuring and evaluating the surface roughness of TEC and BLK rebars through several roughness parameters. Then the quantified surface roughness was compared and evaluated. The thickness of the smooth epoxy coating and the textured epoxy coated was also measured and compared to investigate whether

there was a significant difference which may have affected the bond-slip behavior. In addition, a modified knife adhesion test was also conducted on SEC and TEC bars to provide a qualitative insight on the bond strength between the coating and the steel substrate.

Chapter 4 describes the procedures and experimental results of pull-out tests on specimens with BLK, SEC and different types of TEC bars. The objective was to evaluate and compare the initial slip resistance and peak strength of different types of rebars.

Chapter 5 outlines the finite element studies conducted to understand the interaction mechanism between the TEC bar and the surrounding concrete using the data obtained from the pull-out tests. ABAQUS (Dassault Systèmes, 2014) was used to create a 3-D model of a pull-out specimen using two methods: 1) detailed geometry of rebar and cohesive behaviors as the interaction between bar and concrete; 2) simplified geometry of rebar and axial spring connectors as the interaction. The numerical results were compared with the experimental for validation and stress contour plots were obtained to gain an understanding of the interaction mechanism. In addition, the development length for one type of TEC bar was predicted using a finite element four-point bending beam model.

Chapter 6 presents the design phase of a concrete bridge deck shrinkage test. Two identical large-scale laboratory models of bridge decks reinforced with a selected type of TEC bar and SEC bar were designed to investigate the impact of the bar roughness on the long-term shrinkage of the deck.

Chapter 7 summarizes the major findings of this research.

Chapter 2: Literature Review

2.1 Causes and effects of bridge deck cracking

The cause of concrete deck cracking is that the longitudinal tensile stress in the deck exceeds the concrete tensile strength limit when the volumetric change of concrete is prevented by some source of restraint. The volumetric change of concrete is affected by various types of concrete shrinkage, which are dependent on the properties of the concrete mix itself, construction techniques, and the ambient environmental condition such as temperature changes or humidity (Hadidi & Saadeghvaziri, 2005). Unrestrained shrinkage does not necessarily cause deck cracking if the concrete is not restrained against movement. However, bridge decks generally have both internal and external restraints which prevent the free movement of concrete. Internal restraints are imposed by reinforcements and some aggregates inside concrete. The external restraints are usually caused by the boundary conditions of the bridge, or the composite action of concrete deck and the steel girders beneath when the shear connectors on the girder resist concrete's shrinkage (Hadidi & Saadeghvaziri, 2005). Additionally, since concrete and steel have significantly different thermal conductivities, the difference in the volumetric change induced by concrete shrinkage and steel expansion under the ambient temperature cycles can also contribute to deck cracking.

2.1.1 Plastic shrinkage

In fresh concrete, plastic shrinkage tends to occur when the bleeding water evaporates from the concrete surface faster than the replenishing rate from bleeding. These cracks usually have random orientations and rarely affect the structural performance of the bridge, as shown in

Fig 2.1. When water is removed from the system, menisci are formed between particles. As those menisci produce increasing negative capillary pressure over time, the cement particles are pulled together. When the capillary pressure is accumulated to a certain value, plastic shrinkage cracks are formed (Brown et al. 2001).



Figure 2.1: Typical plastic shrinkage cracks (Basham, 2014).

Plastic shrinkage cracking is more likely to occur with higher ambient temperatures, low humidity, and strong gusts of winds, all of which increase the water evaporation rate near the surface. Concrete mixes with low w/c ratios, high silica fume content, air entrainment, and superplasticizers are also more susceptible to plastic shrinkage since there is little bleed water in concrete (DalSoglio, 2017).

2.1.2 Autogenous shrinkage

Autogenous shrinkage is a major concern in the early stage of high-performance concrete (HPC), in which there is a large amount of cementitious materials and a low w/c ratio. It refers to reduction of apparent volume or length of the cement-based materials under seal and isothermal

conditions (Wu et al. 2017; Williams et al, 2016). No uniform mechanism has been developed for autogenous shrinkage yet, but the capillary tension theory is the most advantageous one. During the cement hydration process, when there is insufficient water in the concrete mix, the product of the cement hydration process takes up smaller space than the reactants. This phenomenon creates a large number of pores in hardened cement paste which leads to the tensile stress in the pore water through the menisci formation. As a result, the relative humidity is decreased and self-desiccation occurs in the cement paste, leading to the shrinkage of concrete (Bentz & Jenson, 2004; Wu et al, 2017). Autogenous shrinkage can cause micro-cracking in concrete and lower the durability of the structure (Wu et al. 2017).

Factors influencing the formation of autogenous shrinkage include low w/c ratio, type of cement, supplemental cementitious materials (SCM), aggregate, admixtures, and curing. It can be mitigated through adjusting mixture proportioning or using shrinkage reducing admixture (SRA) to adjust the extents of cement self-desiccation, internal restraints by aggregates, and expansive reactions (Bentz & Jenson, 2004; Wu et al. 2017).

2.1.3 Drying shrinkage

Compared with the two types of early-stage shrinkages above, drying shrinkage is a long-term shrinkage phenomenon which results in random or transverse cracks (Purvis et al. 1995), as shown in Fig 2.2. The free water is lost at first, which hardly contributes to any volumetric shrinkage. Then the absorbed water in concrete is lost which is equal to the volume change in concrete. The loss of water continues until it reaches equilibrium with the surrounding environment. This loss of water can introduce tensile stress which makes concrete shrink (DalSoglio, 2007; Güneyisi et al, 2010; Zhang et al. 2013). There are three mechanisms of

drying shrinkage: capillary stress, disjoining pressure, and surface tension, each of which is dominant in a different range of relative humidity (Folliard et al. 2003).



Fig 2.2: Typical transverse concrete drying shrinkage cracks (The Concrete Society).

One of the major factors inducing drying shrinkage is the relative humidity of the surrounding environment. With higher relative humidity, drying shrinkage is less likely to happen. The more water the mixture has, the more evaporation, which results in more shrinkage, since increasing the water content in concrete leads to an increase in the capillary water amount (Zhang et al, 2013). On the other hand, aggregates significantly affect drying shrinkage, especially the coarse aggregates. According to Purvis et al. (1995), aggregates affect concrete drying shrinkage in primarily two ways. First, certain aggregates need more water content in the concrete mixture to achieve the desired workability. This extra amount of water needed increases the drying shrinkage. The second way is that certain soft aggregates with low stiffness and high compressibility yield to the pressure from shrinkage and generates more shrinkage. From the

results of the field survey in the same research by Purvis et al. (1995), the aggregate hardness proved to have a significant role in the formation of transverse cracking on bridge decks. Other researches also showed that coarse aggregates play a role in the drying shrinkage development of concrete, and using some specific types of aggregates, such as the limestone aggregate, can effectively reduce the drying shrinkage (Zhang et al, 2013). Apart from the coarse aggregate, other measures to control the drying shrinkage include using some alternative mineral admixtures (Güneyisi et al, 2010; Collepardi et al, 2005), adjusting amount of SCMs (Yuan et al, 2015), and adjusting curing conditions.

2.1.4 Carbonation shrinkage

Carbonation shrinkage occurs in hardened concrete when the hardened cement paste reacts with CO_2 in the air and loses water over a long time. At high relative humidity, the water in concrete pores near the surface prevents the chemical reaction, and therefore prevents the shrinkage. Carbonation shrinkage is usually not a major concern for structural performance of bridges.

2.1.5 Thermal shrinkage

Thermal shrinkage indicates the volumetric shrinkage of concrete resulting from the temperature gradient between the inner and outer layers of concrete during the early stage of hardening, especially in thick sections. The cement hydration process introduces the first round of temperature changes before the concrete hardens. In the fresh concrete, chemical reactions in the cement hydration process happen so that concrete can gain strength, during which heat is produced. Concrete can accommodate this thermal condition without developing any thermal

stresses, but stresses develop as the temperature of the outer layers of concrete soon drops to the ambient temperature after the concrete solidifies at the peak temperature due to concrete's poor heat conductivity (Wu et al, 2017; Klemczak, 2014; Klemczak & Jędrzejewska, 2011). During this cooling period, the deck concrete shrinkage is restrained by the steel beams underneath, causing transverse cracks. The magnitude of this thermal shrinkage depends on the difference between peak concrete temperature and the temperature of the steel beams at the time of peak concrete temperature (Purvis et al. 1995). The temperature of the steel beams is usually close to the ambient temperature. The amount of the volumetric change is also affected by the coefficient of thermal expansion, which is primarily determined by the aggregate type in concrete (Purvis et al. 1995). As the concrete and the steel girders below have different thermal expansion coefficient and different heat conductivity, they have different amounts of thermal expansion under temperature cycles. As a result, any difference in their length changes introduces stresses. Those thermal stresses cause concrete deck to crack if it exceeds the tensile limit.

There are various studies on mitigating strategies for the thermal cracking on concrete, including the use of various novel materials. According to Fernandes et al (2014) and Šavija & Schlangen (2016), phase changing materials (PCM) can be added to cementitious materials as a thermal cracking mitigating solution. Although the addition of PCMs does not affect the progress of reactions in cementing materials, it reduces thermal shrinkage by reducing the rate of semi-adiabatic temperature rise and cool-down rate in cementitious materials. Another proposed method is to use an electrically conductive CNT/cement composite block for an accelerate curing of concrete, which can lead to a uniform distribution of temperature in concrete, therefore reducing the temperature gradient (Kim et al, 2016).

2.1.6 Settlement crack

During the curing of concrete, settlement may occur when large, dense aggregates sink to the bottom. In bridge decks which are usually reinforced with steel rebars, the supporting reinforcing steel serve as obstructions and stop the settlement process. As a result, transverse cracks caused by the induced tensile stress may happen right on top of the reinforcing steel and greatly compromise the bridge service life. This type of cracks is more likely to happen in concrete mixes with high slump, poorly graded aggregates, low cover, and large bar diameters (DalSoglio, 2017).

2.2 *Bond-Slip Mechanism between concrete and reinforcement*

In reinforced concrete, the stress is transferred from concrete to steel reinforcement through the bond between them. In reinforced concrete section design, the assumption is always that the strains of reinforcing steel and the surrounding concrete are the same due to the perfect bond. But in reality, this is usually not the case. Bond strength depends on multiple factors including bar geometry, bar size, concrete cover, reinforcing bar spacing, concrete strength, etc. (Treece & Jirsa, 1989; Harajli et al, 2002; Dybel & Furtak, 2017; Lin et al, 2019). In structural design, the bond between concrete and steel reinforcement has to be maintained until the point of steel yielding. For this reason, adequate development length is required.

Many studies have been conducted on the bond strength between reinforcement and concrete. Bond has three components: 1) chemical adhesion, 2) friction, and 3) mechanical interaction between concrete and steel (Luiz & Gergely, 1967; Luccioni et al, 2005; Xing et al, 2015). For plain bars, the bond strength is primarily dominated by adhesion, which is constituted by chemical bonds (Luccioni et al, 2005). For deformed bars, the mechanical interaction between

concrete and steel plays a more significant role in bond behaviors than the first two components. The deformed bar always tends to move relative to the surrounding concrete unless the strain of the steel and concrete are identical and constant over the length, which is not usually the case. Initially, adhesion and mechanical interaction caused by the surface roughness of the deformed bar offer slip resistance against movement relative to concrete. After the initial adhesion is broken and slip occurs, the tensile capacity across the concrete splitting plane is reduced and the slip is primarily resisted by the bearing force on bar ribs and friction. Fig 2.3 displays a diagram of the bond force components of a deformed bar.

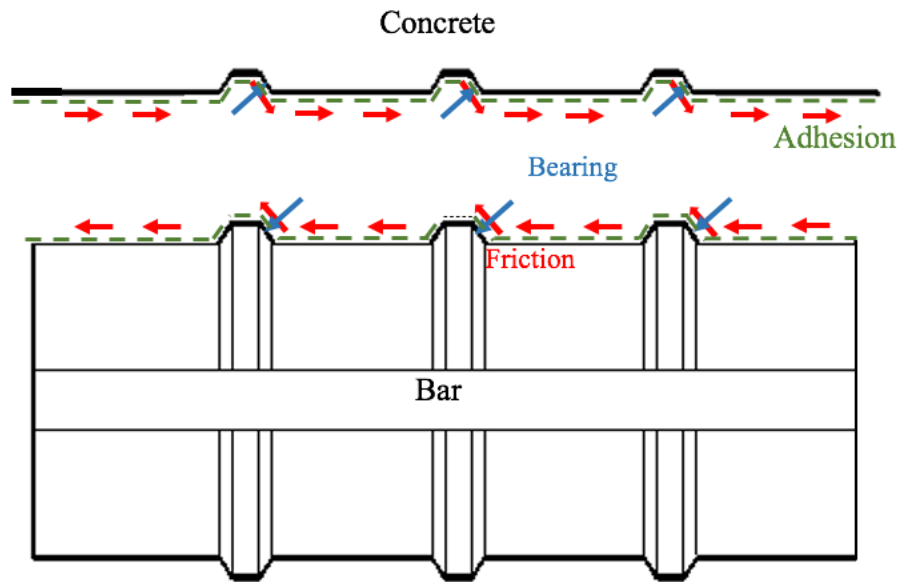


Fig 2.3: Components of the bond force of a deformed bar.

There are two types of bond failures: splitting failure and pullout failure. Wedging action by the rib of the deformed bars resolve the bond force into a normal component and a shear component with regard to the longitudinal bar surface. The resultant of the normal components places the surrounding concrete in tension (Choi et al, 2010). When this component of the

bearing force perpendicular to the bar's longitudinal direction exceeds the concrete tensile capacity due to inadequate concrete cover and reinforcing bar spacing, this radial pressure will result in concrete splitting. In this failure mode, the friction between concrete and steel at interface plays a more important role, since it prevents the concrete key from sliding up against the bar (Treece & Jirsa, 1989; Choi et al, 2010). As illustrated in Fig 2.4, the horizontal component of the resultant force is the effective bond strength. With the frictional component, the friction along the slanting surface of the rib adds to the horizontal bond strength while without the friction, the bond strength is solely due to the bearing force, which becomes smaller (Treece & Jirsa, 1989). Adding confinement or increasing the concrete cover can help in preventing this failure mode. On the other hand, when there is enough concrete cover on the side, pullout failure may occur. For this type of failure, deformed bars bear against the concrete in front of the ribs, increasing the shear stress on the concrete key. Pull-out failure occurs when the concrete key is overcome (Choi et al, 2010). In this failure mode, with adequate splitting capacity, friction is not as critical to prevent the sliding of the concrete key and therefore, it does not play a role as important as in the splitting failure mode.

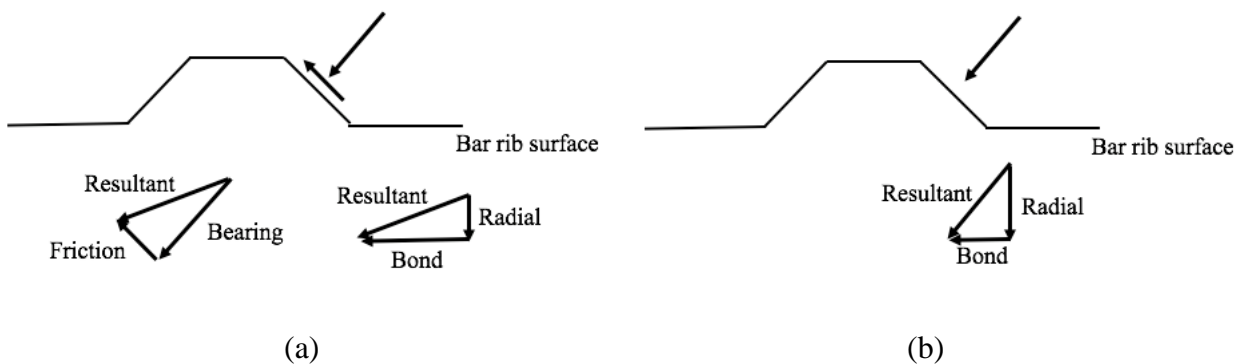


Fig 2.4: Bond strength components (a) with friction; (b) without friction (Treece & Jirsa, 1989).

2.3 Use of smooth epoxy-coated bars in bridge decks

2.3.1 Development of Epoxy-Coated Bars

Numerous methods have been developed to prevent corrosion in bridge superstructures. Of all the proposed solutions, the use of epoxy-coated rebars has been the most cost-effective and widely applied method. The earliest usage of epoxy-coated reinforcing bars is in a bridge in West Conshohocken, Pennsylvania in 1973. In 2013, it was estimated that over 80,000 bridges and numerous buildings, wharfs and other structures were constructed with epoxy-coated bars (Epoxy Interest Group). After several years of the initial use, a more systematic specification was developed by the American Society for Testing and Materials (ASTM) for using epoxy-coated bars in concrete (ASTM A775, 2019). The specification includes information about materials, surface preparation, coating application, and requirements for coated reinforcing bars such as the coating thickness, coating continuity, and coating flexibility.

It is not without reason that epoxy-coated rebars have become the most widely applied mitigating solution against corrosion. Construction with epoxy-coated rebars is not weather or time-dependent, therefore, their use will not delay the construction schedule. Numerous studies also have proved that epoxy coating can protect reinforcing steel in the long run even after the concrete has cracked because of their low permeability. In a study reported by Weyes and Cady (1987), twenty-two bridge decks reinforced with uncoated and epoxy-coated bars were inspected after ten years of service. The inspection showed that none of the decks reinforced with epoxy-coated rebars deteriorated while 40% of the decks with uncoated bars developed early-stage deterioration. This inspection result showed that the epoxy coating on the bar surface effectively prevented steel corrosion. In a more recent study conducted in 2010, which evaluated the

performance of bridge decks in West Virginia, it was found that 33-35 year old bridge decks containing epoxy-coated bars were generally in good or excellent condition, while those decks with uncoated bars were either overlaid or rehabilitated (McDonald, 2010).

Despite the advantages of epoxy-coated bars, studies have shown that smooth epoxy-coated rebars develop less bond strength than uncoated bars. The first study on the bond behavior of epoxy-coated reinforcements was conducted by the National Bureau of Standards (NBS, 1976) on twenty-three epoxy-coated bars of different deformation patterns, coating thicknesses, coating application procedures and five uncoated bars through pull-out tests. The results show that epoxy-coated bars show 94% of the bond of uncoated bars. Most of the tested bars experienced yielding, and only those specimens failing in pull-out mode were considered in strength comparison. As a result, the NBS study suggested a modification factor of 1.15 for the development length of epoxy-coated bars.

In another study by Johnston and Zia (1982) at North Carolina State University, six slab specimens reinforced with epoxy-coated and uncoated bars were tested in both static and fatigue loadings to compare bond strength, crack width, and crack spacing. The study showed that the epoxy-coated bars confined by transverse reinforcement only developed 85% of the bond strength developed by uncoated bars. In their exploratory research on the bond strength of epoxy-coated bars, twenty-one beam specimens reinforced with bars in tension spliced in the center were tested under flexural loads to investigate the effect epoxy-coating coupled with different variables such as bar size, concrete strength, etc. Their conclusion was that the bond strength ratio of epoxy-coated and uncoated bars was 0.66, with a standard deviation of 0.07. This means that for epoxy-coated bars without sufficient cover, the development length has to be increased to gain enough bond strength. In addition to the suggestion by the NBS study, Treece

and Jirsa (1989) made a recommendation that the epoxy coating modification factor should be 1.5 for the calculation of development length when there was insufficient cover.

The failure hypothesis of the smooth epoxy-coated bars, according to Cleary & Ramirez (1989), is that relative to uncoated bars, the smooth surface of epoxy-coated bars cause a loss of adhesion between concrete and steel, which results in a loss of friction at deformations and causes a significant reduction in bond strength. They also found that there were fewer cracks in specimens with epoxy-coated bars but the cracking widths were greater than those of specimens with uncoated bars. In most of the cases, cracking width has a larger impact on structural integrity than the number of cracks. The static flexural test conducted on beam specimens reinforced with epoxy-coated bars by Kobayashi and Takewaka (1984) also confirmed that the maximum crack width increased by about 10% with epoxy coating and the coating also produced a slightly adverse effect on the beam deflection. The increased cracking, together with the increased cost of the larger amount of development length needed, weaken the corrosion control benefit of epoxy coating bars.

2.3.2 Design guidelines regarding smooth epoxy-coated bars

Based the research results above, ACI 318-89 became the first building code to consider the effect of epoxy coating in calculating the development length by introducing a modification factor. The epoxy coating factor specified was 1.5 when the cover is less than $3d_b$ or the bar spacing is less than $6d_b$, where d_b is the rebar diameter; and 1.2 otherwise. This increase in the development length implies an increased amount of steel rebars needed in the structure. The equation itself of the development length of straight bars in tension has changed multiple times over the years, but the modification factors for epoxy coating have remained the same.

2.4 Other mitigation measures to resolve the corrosion issue

Apart from the epoxy coating, which is the most prevalent concrete corrosion-control method, there are other mitigation measures to prevent corrosion in concrete bridge decks, including using Fiber Reinforced Polymer (FRP) composite as an alternative reinforcement material, novel concrete mixtures, surface coating of concrete deck, and staining of reinforcing bars. The following sections introduce those alternative corrosion mitigation measures.

2.4.1 FRP Composites

FRP composites have been considered as a very promising substitute for steel reinforcement in concrete structures to prevent corrosion, especially under severe environmental conditions. FRP reinforcements were first used in reinforced-concrete structures as early as in 1950s (Rubinsky and Rubinsky, 1954). Compared with steel, FRP reinforcement is corrosion-free, light-weighted, and easy to install. It also has high strength and durability. In terms of material properties, FRP composites rupture at a relatively large displacement after a linear stress-strain behavior and are usually designed to fail in concrete-crushing mode, which is more preferable than the reinforcement failure mode as this type of failure is more gradual and less catastrophic (Kassem et al, 2011). Table 2.1 summarizes the material properties of different types of FRP reinforcements and steel (ACI 440.1R-15, 2015). In civil structural applications, there are four types of dominant FRPs: carbon-FRP (CFRP), glass-FRP (GFRP), aramid-FRP (AFRP) and basalt-FRP (BFRP). Of the four types, CFRP has the highest stiffness and the GFRP is the least stiff. GFRP bars are the most predominant type of FRP bars used in bridge decks in North America due to their relatively lower initial cost compared to other types of FRP bars

(Wan, 2014). Different types of FRP bars also have different surface textures, as shown in Fig 2.5.

Table 2.1: Material properties of FRP and steel reinforcing bars (ACI 440.1R-15, 2015).

	Steel	GFRP	CFRP	AFRP
Nominal Yielding Stress, ksi (MPa)	40 to 75 (276 to 517)	NA	NA	NA
Tensile Strength, ksi (MPa)	70 to 100 (483 to 1600)	70 to 230 (483 to 690)	87 to 535 (600 to 3690)	250 to 368 (1720 to 2540)
Elastic Modulus, $\times 10^3$ ksi (MPa)	29.0 (200.0)	5.1 to 7.4 (35.0 to 51.0)	15.9 to 84.0 (120.0 to 580.0)	6.0 to 18.2 (41.0 to 125.0)
Yield strain, percent	0.14 to 0.25	NA	NA	NA
Rupture strain, percent	6.0 to 12.0	1.2 to 3.1	0.5 to 1.7	1.9 to 4.4

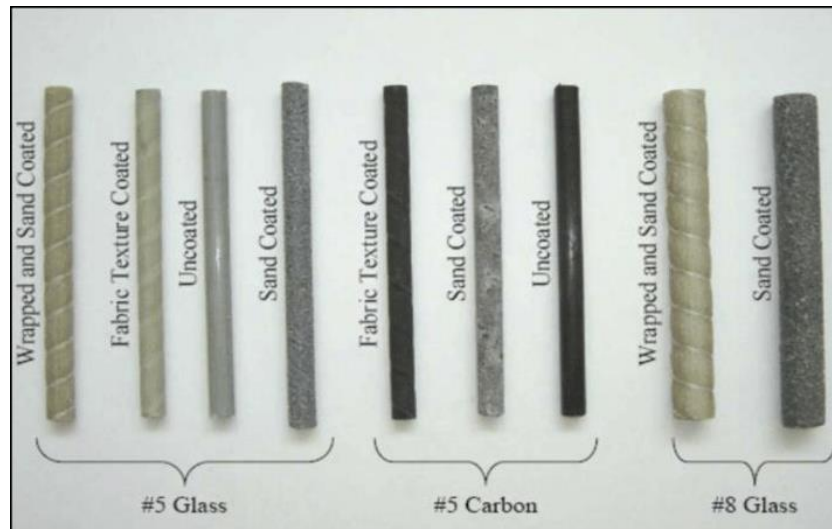


Fig 2.5: Different types of FRP reinforcements (Khalefa & Kaska, 2017).

Although FRP composites show a great potential to be a good reinforcement material, there are some concerns regarding their structural performance, serviceability and cost-effectiveness. Compared with steel-reinforced structures, FRP-reinforced structures generally have greater crack widths, which compromises the structural performance. At the same

reinforcement ratio, the FRP-reinforced structures also have lower stiffness and larger deflections due to the low elastic modulus. Because of the low shear modulus of the composite, there is considerable shear deformation as well. In addition, FRP composites also have high initial costs, higher susceptibility to mechanical damage and fire, and are impossible to bend on field (Sonnenschein et al. 2016). The initial materials cost for FRP-reinforced concrete bridge deck was evaluated to be 60% higher than that of its steel-reinforced counterpart (Berg et al. 2006). But in the long-term, FRP reinforcements may still be cost-effective for some cases considering the savings in labor and maintenance costs.

2.4.2 Alternative Concrete Mixtures

Various mix design factors and material properties of concrete can have significant impact on transverse cracking of bridges. The factors affecting bridge deck cracking related to concrete mixture can be divided into two categories: 1) materials used in concrete mixture, such as aggregates, type of cement, admixtures, water content, w/c ratio, etc.; 2) concrete properties, such as compressive strength, air content, and slump.

The type and size of aggregates can affect deck cracking significantly. It has been recommended to use large size of aggregates, maximize the volume of aggregates and low-shrinkage aggregates to reduce cracking (Krauss and Rogalla, 1996). Schmidt and Darwin (1999) conducted field surveys of 40 continuous steel girder bridges representative of the construction throughout Kansas to evaluate the correlation between various concrete materials properties and the amount of cracks. The amount of cracks was quantified with the crack density in terms of length per unit area. It was found that an increased amount of water content, cement content and w/c ratio can lead to higher crack densities. Crack also increases with increasing slump and

concrete compressive strength. However, there are other studies which obtained a contradictory conclusion about the correlation between slump and cracking. In the state-of-art report about transverse cracking of concrete bridge decks by Hadidi and Saadeghvaziri (2005), it was found that some studies, such as the ones by Stewart and Gunderson (1969) and Krauss and Rogalla (1996), stated that there was no relation between slump and cracking in concrete. In a study by Cheng and Johnson (1985), transverse cracking even decreased with an increase in slump. Therefore, the correlation between slump and cracking tendency is still uncertain. Schmidt and Darwin (1999) also noticed a decrease in cracking tendency with an increase in air content, especially that there was a significant decrease in cracking when the air content exceeded 6%. Various types of admixtures, such as retarders or water reducing admixtures, also affect concrete deck cracking to different extents.

Due to the pronounced impact of the concrete mixture on the bridge deck cracking tendency, alternative mixture designs and materials have been proposed to mitigate cracking. A common practice already applied in many structures is to use Type II cement, which helps to reduce cracking through decreasing early thermal gradient. A study conducted by Brown et al. (2007) investigated various alternative materials in concrete mixtures to reduce concrete cracking through restrained and free ring tests and large-scale bridge deck (LSBD) tests. As the concrete shrinks, the restraint by the inner steel ring represents the worst-case scenario for concrete when dealing with shrinkage cracking. The LSBD tests resemble a typical Texas bridge deck. The mixtures tested included a control mixture, high performance concrete (HPC), silica fume mixture (SF), two types of fiber reinforced concrete (FRC) mixtures, shrinkage-reducing admixture (SRA) mixture, Type K cement mixture, high-volume fly ash (HVFA) mixture and shrinkage-compensating mixture. Of all types of mixtures, it turned out that the Type K concrete

and SRA concrete exhibited the least cracking while the control mixture and HPC mixture exhibited a high propensity of shrinkage cracking. Another study supported by IDOT (Rahman et al. 2018) also evaluated the use of Type-K cement as a partial replacement of Portland cement to reduce cracking in bridge decks through monitoring shrinkage of a large-scale bridge deck specimen over six months. The results showed that Type-K cement decreases cracking in both longitudinal and transverse directions through an early expansion during early-age hydration. This early expansion introduced compressive stress in concrete and compensated the onset of cracking due to the tensile stress.

Although alternative mixture proportioning and novel materials can help reduce cracking in bridge decks, this corrosion-control method cannot be used in many cases. Some novel cement and admixtures have high initial costs. Additionally, using those shrinkage-compensating concrete mixtures usually compromises other important concrete properties such as compressive strength and workability.

2.4.3 Deck Surface Coating

The goal of the deck surface coating is to create a barrier between concrete and the environment around it to prevent aggressive substance and moisture from penetrating into concrete and cause reinforcement corrosion. Therefore, this type of coating is also called a surface sealer. The effectiveness of concrete surface coating is affected by many factors, such as surface preparation, application rate, adhesion with concrete surface, and the chemical properties of the coating itself (Kepler et al, 2000). When using certain types of coatings such as silanes or siloxanes, improper surface preparation may also adversely affect the coating effectiveness. The deck must be free of any oil, curing compounds, and road grim to ensure that the coating

material can make full contact with the concrete surface (Sherman et al, 1993). One of the most important properties of a concrete surface coating is its vapor transmission characteristics, which indicates the ability of the moisture inside the concrete to pass through the sealer and escape, which prevents the high vapor pressure from building up in concrete during dry periods to cause the coating to blister and peel (Sherman et al. 1993).

Concrete surface coating can be divided into three main categories: organic coatings, hydrophobic impregnation, and cementitious coatings (Bertolini, et al. 2004). Organic coating forms a polymeric film on the concrete surface to block carbon dioxide and chloride ions. It can be dense coating or vapor permeable coating (Goyal, et al. 2018). Dense coatings, which are based on epoxy, polyurethane, and chlorinated rubber polymer, do not let moisture in the concrete escape at the time of application, which may result in loss of adhesion and coating failure. Vapor permeable coating are acrylates and allow the moisture to escape, therefore there is less risk of coating degradation (Bertolini et al. 2004). Hydrophobic impregnation coatings, such as silanes and siloxanes, can penetrate into concrete and form a water-repellent linings on the pore walls to prevent the penetration of aggressive substances (Goyal, et al. 2018). Cementitious coating is cement-based coating applied by brushing or in overlays which have good carbonation and chloride penetration resistance.

Within the three main categories, there are many different types of concrete surface coatings used in industry with different properties and costs. The first sealer used in concrete decks in the US is linseed oil. It is one of the last expensive corrosion protection strategies in the market but need to be reapplied every 2 to 5 years (Sherman et al. 1993). Other types of surface coating include epoxy, silane, and methacrylate. Fig 2.6 shows a typical bridge coating application process.



Fig 2.6: Typical concrete deck coating application (Master Builders Solutions).

Concrete surface coatings are easy to apply and does not complicate structural design as using epoxy-coated reinforcement does. But the effectiveness of the surface coating is questionable. A study by Al-Zahrani et al. (2002) conducted a comparative study on uncoated concrete specimens and specimens coated with four different common types of surface coatings, including cement-based polymer-modified coating, cement-based coating, polyurethane-based coating, and epoxy-based coating, on their physical properties. They found that although all types of coatings tested provided better performance compared with uncoated specimens, they still allowed certain amounts of chloride ions to penetrate into the concrete, especially with wetting/drying cycles and heating/cooling cycles. Overall, polyurethane-based coating, and epoxy-based coating demonstrated far more superior performance in durability than the other coating systems. Another study on the effectiveness of surface coatings against sulfate, chloride and carbonation attacks conducted by Ibrahim et al. (1999) proved that all the coatings investigated were not effective in reducing concrete deterioration from sulfate attack and none of the coatings were totally effective in preventing carbonation of concrete.

2.4.4 Stainless steel

Stainless steel has been used as an alternative reinforcement material in reinforced concrete structures to prevent corrosion, as shown in Fig 2.7. Stainless steels are chromium containing steel alloys, with the minimum chromium content to be 10.5%. There are three major types of stainless steels applied as reinforcements in concrete: 1) Ferritic; 2) Austenitic; 3) Austenitic-Ferritic (Duplex). Of the ferritic stainless steels, 12% chromium-containing steels are mostly used in structural applications. Austenitic stainless steel is the most widely used stainless steel, making the steel structure fully austenitic and durable. The duplex stainless steel has combined characteristics of ferritic and austenitic features, giving structures both strength and ductility. This type of stainless steels is rated to be in the high range of corrosion resistance (Markeset, et al. 2006). There have been various methods of classification for the stainless steel. The European standard EN 10088-1 (1995) provides a uniform method of classification of stainless steels. Table 2.2 provides a comparison of methods of classification for common stainless steels by Markeset et al. (2006). Most of the stainless steels used as reinforcement are within types 1.4301 and 1.4436.



Fig 2.7: Stainless steel reinforcing bars (Concrete Construction, 2017).

Table 2.2: Comparison of methods of classification for common stainless steels (Markeset et al, 2006).

Steel Type	Steel Grade		USA	Great Britain	Sweden	PREN-value
	EN1008 8-1	Designation	AISI	BS	SS	
Austenitic	1.4301	X5CrNi 18-10	304	314S11/314S15	2332	19
	1.4401	X5CrNiMo 17-12-2	316	316S33	2347	25
	1.4429	X2CrNiMoN 17-13-3	316LN	316S63	2375	26
	1.4436	X5CrNiMo 17-12-2	316	-	2343	26
	1.4571	X6CrNiMoTi 17-12-2	316Ti	-	2350	25
Ferritic- Austenitic (lean duplex types)	1.41xx (LDX 2101)	X3CrNiMo 22-2-0	-	-	-	26
	1.4362	X2CrNiMo 23-4	-	-	-	24
Ferritic- Austenitic (Duplex)	1.4462	X2CrNiMoN 22-5-3	-	318	2377	36

Stainless steel is usually used in chloride-bearing environments (Bertolini et al. 2013).

The stainless steel reinforcements are highly effective in resisting corrosion because a thin layer of chromium oxide film forms on the surface of the reinforcement and creates a passive condition to improve the corrosion resistance (Markeset et al. 2006). The corrosion resistance of stainless steel is significantly greater than that of mild or carbon steel because of the high stability of the chromium oxide film. Pitting is the only type of expected corrosion with stainless steel, since the other types of corrosion, such as stress corrosion, can only take place at extreme environments of high temperature, carbonated concrete, and heavy chloride contamination (Bertolini et al. 2013).

Due to economic reasons, stainless steel reinforcements are usually used as skin reinforcements or inside critical elements. In structural rehabilitations, stainless steel reinforcement is often coupled with the original carbon steel. In this case, there is a risk of galvanic corrosion. But experimental studies have shown that the consequences of coupling stainless steel with carbon steel are negligible compared with those of coupling corroding carbon steel with passive carbon steel. Therefore, it has been suggested that stainless reinforcement can serve as a better reinforcement material than the common carbon steel when part of the corroding reinforcement need to be replaced (Bertolini et al. 2013).

Despite the benefits of stainless steel, a major setback which prevents wide application of stainless steel reinforcements in structures is the high initial cost. Compared with the cost of carbon steel, the cost of stainless steel is 6-10 times higher. Other related costs, such as bending, transportation and cutting, remain the same (Markeset et al. 2006).

2.4.5 Galvanized Reinforcement

Galvanized reinforcements are produced by a hot-dipping galvanizing process using zinc metal. It is more resistant to corrosion compared with conventional steel reinforcement especially when the structure is exposed to carbonation or mild contamination of chlorides (Goyal et al. 2018). The galvanizing process gives the reinforcement a metallic coating of multiple layers of iron-zinc alloys, with a layer of pure zinc formed on top (Bertolini et al. 2013), as shown in Fig 2.8. The thickness of the zinc layer significantly affects the corrosion resisting capacity of the reinforcements. Without sufficient thickness of the zinc layer, it is more difficult for the protective passive film on the surface of the bar to form (Bertolini et al. 2013).



Fig 2.8: Galvanized rebars (International Zinc Association)

The problem with galvanized reinforcements is that a significant portion of the zinc layer can be lost even before the steel substrate is attacked by corrosives. At early age after casting, there is a loss of bond strength at the interface of concrete and reinforcement due to the formation of hydrogen gas. A solution to this problem is to add soluble inhibitors such as chromates. But their use is limited by the European Union because of their toxic nature. The risk of stress corrosion cracking in galvanized bars under high stress is also higher compared with conventional steel reinforcements (Goyal et al. 2018). In addition, the initial cost of galvanized reinforcement is 2-2.5 times of that of conventional steel reinforcements (Bertolini, et al. 2013).

2.5 Textured epoxy-coated (TEC) bars

2.5.1 Background

Although epoxy-coated reinforcement remains to be one of the most popular methods of mitigating corrosion in bridge construction, it introduces more cracking in bridge decks and require a greater amount of development length of reinforcement due to loss of bond between concrete and reinforcement. In order to keep the benefits of the epoxy coating and overcome the

disadvantages without requiring significant technology advances, the Illinois Department of Transportation (IDOT) developed a new type of textured epoxy-coated (TEC) reinforcement with applied surface roughness. The specific coating materials and coating application process are proprietary. The additional roughness was expected to increase the bond between concrete and reinforcement through increasing adhesion and friction. Fig 2.9 shows a comparison of uncoated, smooth epoxy-coated and TEC reinforcing bars.

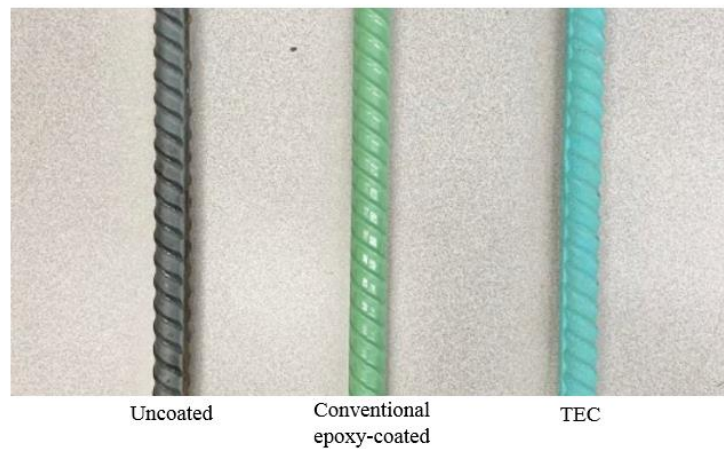


Figure 2.9: Comparison of uncoated, smooth epoxy-coated and TEC reinforcements.

2.5.2 Exploratory Study of TEC Bars

Kim and Andrawes (2019) at the University of Illinois at Urbana-Champaign did an exploratory study on the bond-slip behavior of TEC bars. Direct pull-out tests and flexural tests were conducted with No.5 and No.8 uncoated, smooth epoxy-coated, and TEC bars in both confined and unconfined conditions.

The basic principle of direct pull-out test is to exert an axial tensile load on the steel bar with the concrete bearing against the testing frame. The bond-slip behavior of the bar was

quantified through the force-slip curve. The slip was measured with a Linear Variable Differential Transformer (LVDT) at the free end of the bar against the movement of the concrete. The dimensions of the direct pull-out specimens and testing procedures were based on International Union of Laboratories and Experts in Construction Materials, Systems and Structures (RILEM) specifications (1994). PVC sleeves were introduced to eliminate the bond of bars and concrete in the unbonded region. Fig 2.10 displays a schematic diagram of the pull-out specimen and the pull-out test setup.

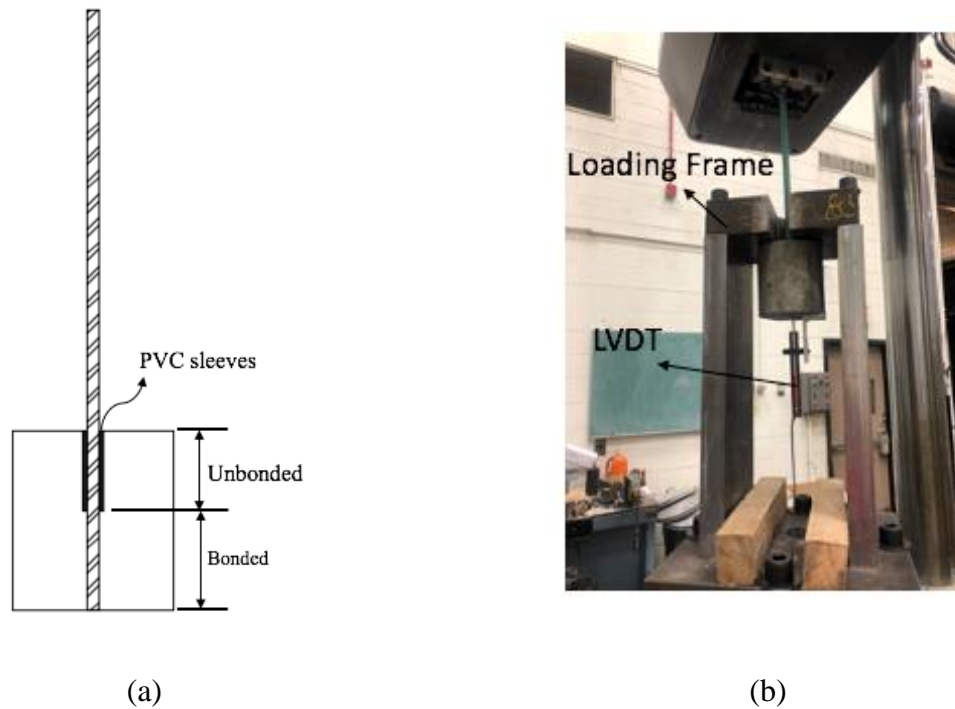


Fig 2.10: (a) Schematic diagram of pull-out test specimen; (b) pull-out test setup (Kim & Andrawes, 2019).

For No.5 bars, six specimens with an embedded length (l_e) of 2 in. (50 mm) and fifteen specimens with an l_e of 3 in. (75 mm) were tested. The test results showed that the epoxy-coated bars exhibit notably reduced slip resistance compared to the uncoated bars, but they achieved high peak strengths comparable to those of uncoated bars. Contrary to the expectations, the

average peak pull-out force of the TEC bars was 19% lower than that of uncoated bars for $l_e = 2$ in. (50 mm) and 14% lower for $l_e = 3$ in. (75 mm). Although the TEC bars showed high initial slip resistance, the bond degraded sharply which indicated rapid loss of bond. None of the TEC bars showed any improved behaviors in the post-peak region compared with the uncoated and smooth epoxy coated bars. After the TEC bars were manually pulled out, the surfaces of the bars were examined and it was found that there was an adhered layer of uncrushed cement paste at the bonded interface, which reduced the height and angle of the bar ribs and therefore reduced the bearing effect.

For unconfined specimens with No.8 bars, all three specimens failed in splitting mode at almost identical force levels. It can be concluded that the splitting failure occurred simply due to insufficient concrete cover. Since splitting failure mode was not of interest in this study, steel and NiTiNb shape memory alloy (SMA) wires were used to confine the specimens. The results for the confined specimens were similar to those of No.5 bars, i.e. high initial slip resistance followed by rapid slip was observed for TEC bars. The confined No.8 TEC specimens however, attained 95% of the peak force of the uncoated bars, which was higher than the No.5 test results.

Apart from the direct pull-out tests, flexural tests were conducted on uncoated, epoxy-coated and TEC bars to supplement the findings from the direct pull-out tests. One beam specimen reinforced with a single No.5 bar was casted for each type of bar. The depth and cover were designed based on typical bridge deck thickness and cover used by IDOT. The development length, l_e , of the reinforcement was designed as per the American Association of State Highway and Transportation Officials (AASHTO) and Load and Resistance Factor Design (LRFD) Bridge Design Specifications (2017) to be 10.63 in. (270 mm) for epoxy-coated bars. To

induce failure, all specimens were tested as cantilevers with $l_e = 9.84$ in (250 mm). The deflection and slip were measured with LVDTs.

The force-deflection and force-slip results of the flexural tests showed that there was almost no slip resistance in epoxy-coated bars while the uncoated and TEC specimens exhibited ductility without significant slip. The slip occurring at cracking of the uncoated specimen was greater than that of TEC specimen, indicating a higher resistance for the TEC specimen.

The results of the direct pull-out tests and flexural tests by Kim and Andrawes (2019) demonstrated the great potential of the TEC bars in improving the bond-slip behavior by showing the high initial slip resistance. However, there are also concerns regarding the fast degradation of slip resistance of TEC bars possibly due to the adhering layer of uncrushed cement paste on the bar.

2.6 Coating Adhesion Tests

Although many studies have been conducted on the bond-slip mechanism between concrete and reinforcing bars, most studies only considered the interface between the bar and concrete. This consideration is reasonable for uncoated bars. However, for coated reinforcing bars, apart from the bar-concrete interface, the interface between the coating and the steel substrate also needs to be considered since the coating can be peeled off from the bar after slip occurs. Therefore, it is necessary to understand and evaluate the adhesion between the coating and the steel substrate. The following subsections present a summary of the most commonly used methods for evaluating the adhesions between the coating and steel substrate.

2.6.1 Tape Test (ASTM D3359-17)

This test method qualitatively assesses the adhesion of relatively ductile coating films to metallic substrates through applying and removing pressure-sensitive tape from the penetrative cut made on the coating. It can be further divided into two categories based on the test subjects:

1) Test Method A: more suitable for use in the field; 2) Test Method B: more suitable for use in laboratory or shop environments but cannot be used for coating thicker than 4.9×10^{-3} in. (125 μm) unless wider spaced cuts are allowed.

For Method A, an “X” cut with a smaller intersection angle of 30° - 45° is made through the coating. Each of the two cuts of the “X” needs to be about 1.57 in (40 mm). A piece of 3-inch-long (75-mm-long) pressure-sensitive tape is placed with its center at the intersection of the cut on the coating. The tape needs to be rubbed firmly over the surface of the coating to ensure good, uniform contact between the tape’s adhesive and the coating. Within 90 ± 30 s of tape application, the tape is removed through pulling the free end of the tape rapidly off at an angle as close to 180° as possible along the same direction as the smaller angles of the “X” cut. This test provides a qualitative result. Depending on the condition of the coating after the tape is torn off, the adhesion is rated in the following scale shown in Table 2.3. The test shall be repeated in a total of three locations on the test surface.

Table 2.3. Coating adhesion rating scale.

Rating	Coating Condition
5A	No peeling or removal.
4A	Trace peeling or removal along incisions or at their intersection.
3A	Jagged removal along incisions up to 1/16 in. (1.6 mm) on either side.
2A	Jagged removal along most of incisions up to 1/8 in. (3.2 mm) on either side.
1A	Removal from most of the area of the X under the tape.
0A	Removal beyond the area of the X.

For Method B, instead of an “X” cut, a series of cuts making up a grid system shall be made on the test surface. For coatings with a thickness up to 1.97×10^{-3} in. (50 μm), 11 parallel cuts spaced at 0.04 in. (1 mm) apart should be made; for coatings with a thickness between 1.97×10^{-3} in. (50 μm) and 4.92×10^{-3} in. (125 μm), six parallel cuts spaced at 0.08 in. (2 mm) apart should be made; unless wider spaced cuts are allowed, Method B should not be used for coatings with a thickness greater than 4.92×10^{-3} in (125 μm). All cuts should be about 0.79 in. (20 mm) long and penetrate the coating all the way to the substrate. The same number of parallel cuts should be made perpendicular to the original cuts. The same procedure of tape application and removal as used in Method A shall be implemented for Method B as well. After the tape is removed, the grid area should be examined and the adhesion should be rated based on the scale shown in Fig 2.11.

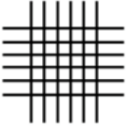
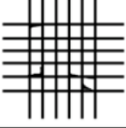
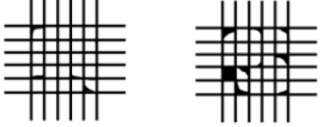

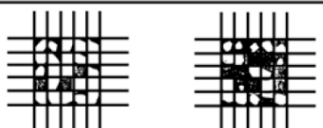

CLASSIFICATION OF ADHESION TEST RESULTS		
CLASSIFICATION	PERCENT AREA REMOVED	SURFACE OF CROSS-CUT AREA FROM WHICH FLAKING HAS OCCURRED FOR SIX PARALLEL CUTS AND ADHESION RANGE BY PERCENT
5B	0% None	
4B	Less than 5%	
3B	5 – 15%	
2B	15 – 35%	
1B	35 – 65%	
0B	Greater than 65%	

Fig 2.11: Classification of adhesion test results in Method B (ASTM D3359-17, 2017).

The advantages of this test are the easy implementation and qualitative rating. However, this tape test may not necessarily generate reliable and consistent results since there is variation in the type of tape selected, the force exerted in applying and removing the tape based on the individual performing the test, and the intersection angle of the “X” cut. In addition, this test does not provide any quantitative evaluation of the adhesion.

2.6.2 Knife Test (ASTM D6677-18)

This test method qualitatively assesses the adhesion of the coating to substrate by using a knife. This method can be used in both laboratory and the field. Two penetrating cuts making up an “X” with an intersection angle between 30° and 45° shall be made using a utility knife. The cuts have to be made in one stroke and completely penetrate the coating. Each leg of the “X” has to be at least 1.5 in. (38.1 mm) in length. After the cuts are made, the point of the knife needs to be employed at the vertex of the angle to lift up the coating from the substrate. Sufficient tests have to be made to improve the consistency of the experimental data. The rating of the adhesion is based on the difficulty in lifting the coating.

Similar to the tape test, the knife test is easy to implement and can provide a general qualitative adhesion evaluation. However, this test is highly subjective. The individual who conducts this test may lift the coating at the vertex with different forces at different angles, which may significantly affect the test results. The rating system is also heavily dependent on personal bias. A way to minimize personal bias is to have the same individual conduct all the tests in a consistent manner and evaluate the adhesion rating.

2.6.3 Pull-off test (ASTM 4541-17)

This test provides a quantitative evaluation of the adhesion (also pull-off strength) between coating and metal substrate. The basic principle of this test is to measure the force needed to detach the coating from the metal substrate along the direction perpendicular to the surface. There can be different ways to conduct the measurements, such as using a fixed alignment adhesion tester or a self-alignment adhesion tester. Fig 2.12 displays multiple types of loading test fixtures from ASTM 4541-17 (2017).

After the test surface area is selected, a loading fixture, which can be a dolly or a stud, is glued to the test surface. After the glue cures, the testing apparatus is attached to the loading fixture and aligned along the direction normal to the test surface. The force is gradually and uniformly applied on the loading fixture till the coating is completely detached from the metal substrate. It is specified in the ASTM standards that the rate of pull shall be 1MPa/s or less. The two common uses of this test are: 1) test to fracture, which records the maximum load achieved when the coating is fully detached; 2) pass/fail test.

The test results can be affected by many factors, including the selected loading fixture, type of glue, pulling rate, and glue curing time. Compared with the other tests, the pull-off test not only provides quantitative results but also is more accurate and less subjective.

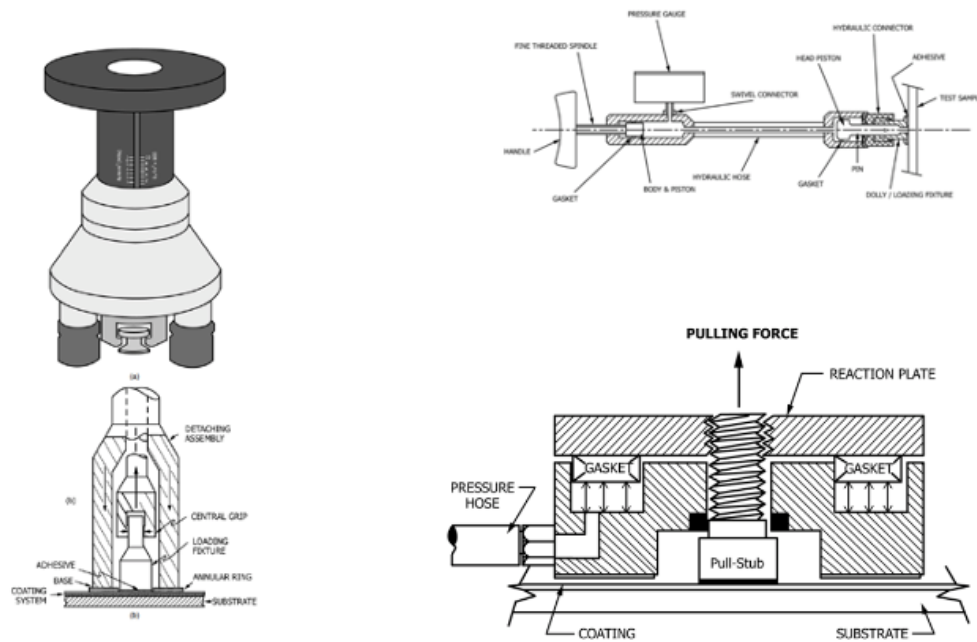


Fig 2.12: Schematic diagram of different types of pull-off testers. (ASTM 4541-17, 2017).

2.6.4 Modified Knife Test (Vaca-Cortes et al. 1998)

A study sponsored by the Texas Department of Transportation conducted at the University of Texas at Austin investigated the available coating adhesion tests and developed a new knife adhesion test to eliminate subjectivity and quantify adhesion through the use of a calibrated knife (Vaca-Cortes et al, 1998). This proposed knife test is based on the knife test specified in ASTM 6677-18 (2018). It can be performed after immersion in hot water if simulation of a harsh environment is desired.

The original knife test specified in ASTM standards is highly subjective due to the variation in the force exerted on the knife. In this study, various types of utility knives and knife blades were tested in an effort to develop a self-calibrating knife which can produce a force of a designated magnitude. For this purpose, an internal spring is placed inside the knife case to control the force. Since the stiffness of the spring is known, the magnitude of the force is determined by measuring the spring compression. A slot is designed and placed on the knife case in which an indicator is sliding back and forth to control the force. A scale is placed below the slot to show the magnitude of the desired force values.

Chapter 3: Characterization of the Surface Roughness of TEC Rebars

3.1 Introduction

In the previously discussed exploratory study by Kim and Andrawes (2019), although the textured epoxy-coated (TEC) bars showed potential at the initial stage of the direct pull-out test and the flexural test, their slip resistance degraded rapidly at a later stage. There was also not a significant increase in the peak strength of the TEC bars compared with that of the uncoated black (BLK) and smooth epoxy-coated (SEC) bars. Despite the conclusions of the study by Kim and Andrawes (2019), it was still unclear how the surface profile of the TEC bars impacted their interfacial bond-slip behavior with concrete. To address this issue, it was necessary to carry out 2-D and 3-D surface profile analyses on TEC bars of various surface roughness. The analyses were divided into two phases. Phase I study was a continuation of the previous research by Kim and Andrawes. Surface roughness of the same No.5 and No.8 TEC bars used in the previous study was quantified to be compared with that of the BLK bar to obtain a deeper insight on the difference of their surface characteristics. In addition, the quantified surface roughness of No.5 and No.8 TEC bars were also compared to verify whether the surface roughness was consistent between the two sizes. Since the coating thickness was also a factor which may potentially affect the bond-slip behavior and it was unknown whether the applied surface roughness changed the surface coating thickness, the coating thickness of the TEC and SEC bars were compared to determine whether coating thickness played a role during the interaction between the bar and the surrounding concrete.

In Phase II, apart from the previously investigated bars, surface roughness analyses were carried out on five additional types of TEC bars with different levels of surface roughness

provided by different manufacturers. To differentiate those types of bars, the total six types of bars were labeled as TEC1-6, TEC1 being the bars used in the previous study of Kim and Andrawes (2019). TEC1-3 bars were manufactured by the same manufacturer and TEC4-6 bars were provided by another manufacturer. The coating application procedure of the two manufacturers were both proprietary. Microscopic images and Gaussian-filtered 3-D topology of the bar surfaces were also obtained to supplement the roughness analyses. In addition, the adhesion between the coating and the steel substrate was quantified and compared for both TEC and SEC bars to see whether there was a distinct difference in the coating adhesion between both bars. The numerical values of all the measurements and average roughness parameters in this chapter are shown in Appendix A.

3.2 Phase I Study

3.2.1 Surface Roughness Quantification Methodology

The surface profile of reinforcing bars in this study was measured using a KLA Tencor P6 profilometer located at Beckman Institute Imaging Technology Group at the University of Illinois at Urbana-Champaign (see Figure 3.1a). The KLA Tencor P6 was a stylus-based profilometer that was able to measure the surface height up to 0.04 ± 0.02 in. (1048 ± 524 μm) with a resolution of 2.46×10^{-6} in. (0.0625 μm). The stylus had a 7.87×10^{-5} in. (2 μm) radius tip and scanned the surface with contact force between $1.10 \times 10^{-6} \sim 1.10 \times 10^{-4}$ lb ($0.5 \sim 50$ mg). The scan size (width and length) and spacing of data points in each direction can be controlled, allowing high resolution 2-D and 3-D surface topography measurements. As shown in Fig 3.1b, 3-inch-long rebar segments were randomly selected along the length of the rebar and placed on a 3D-printed supporting base for the

measurement of the raw surface profile. For this comparative study, only the areas between ribs were measured for roughness quantification.

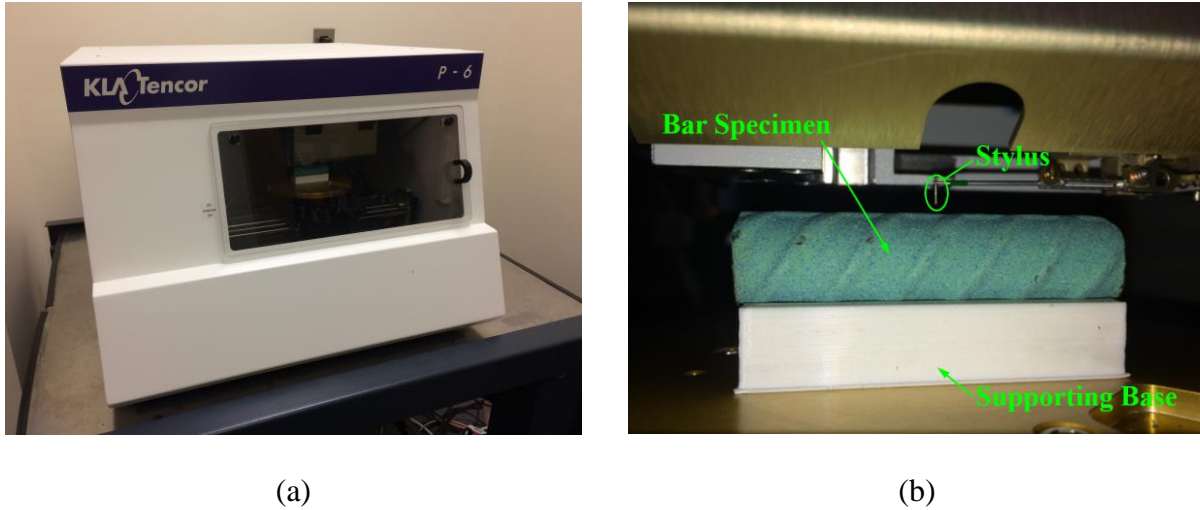


Fig 3.1: Profilometer system used in the study: (a) KLA Tencor P6 and (b) stylus of the profilometer.

After the raw surface profiles were obtained, they were post-processed by filtering out the effect of noise and long waviness. This process is schematically described in Fig. 3.2.

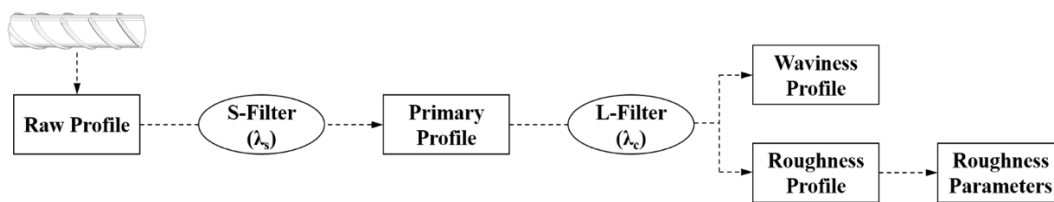


Fig 3.2: Post-processing of the raw profile data.

The Gaussian filter based on ISO 16610-21 (2011), which had been widely used for surface analysis, was selected in this study to filter the measured data. The digitalized raw profile of the bar specimens was first filtered using S-filter with a short cutoff wavelength (λ_s) of

3.15×10^{-4} in. (8 μm) as per the recommendations of ISO 3274 (1996) to suppress the high-frequency noise that was included during the measurement. The primary profile was again filtered using L-filtering to separate the roughness profile and the waviness profile. A long cutoff wavelength (λ_c) was used first to obtain a waviness (low frequency) profile, and the roughness profile was extracted by subtracting the waviness profile from the primary profile. As per ISO 4288 (1996), different λ_c values ranging from 0.0032 in. (0.08 mm) to 0.32 in. (8 mm) were recommended depending on the roughness of the filtered profile. Due to the short available scan length of 0.20 in. (5 mm) between the scanned rebar ribs, λ_c was taken as 0.10 in. (2.5 mm) in this study. The selected long cutoff wavelength was also used as a sampling length which acted as a unit length to estimate the roughness parameters. The 2-D Gaussian filtering for linear profiles described above was conducted using a MATLAB script code. Fig. 3.3 presents typical linear surface profiles of a TEC1 bar and a BLK bar before and after the post-processing of the Gaussian filter. From the filtered profiles in Fig 3.3a and Fig 3.3b, the BLK bar had a much more flat surface profile compared with the TEC1 bar, which indicated that the TEC1 bar had a much greater surface roughness.

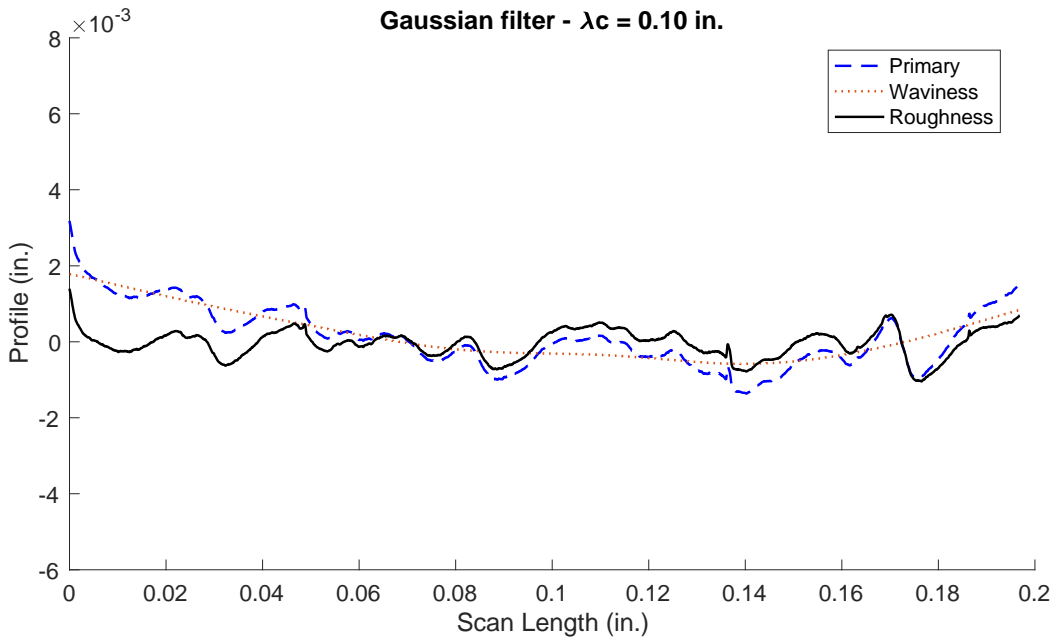
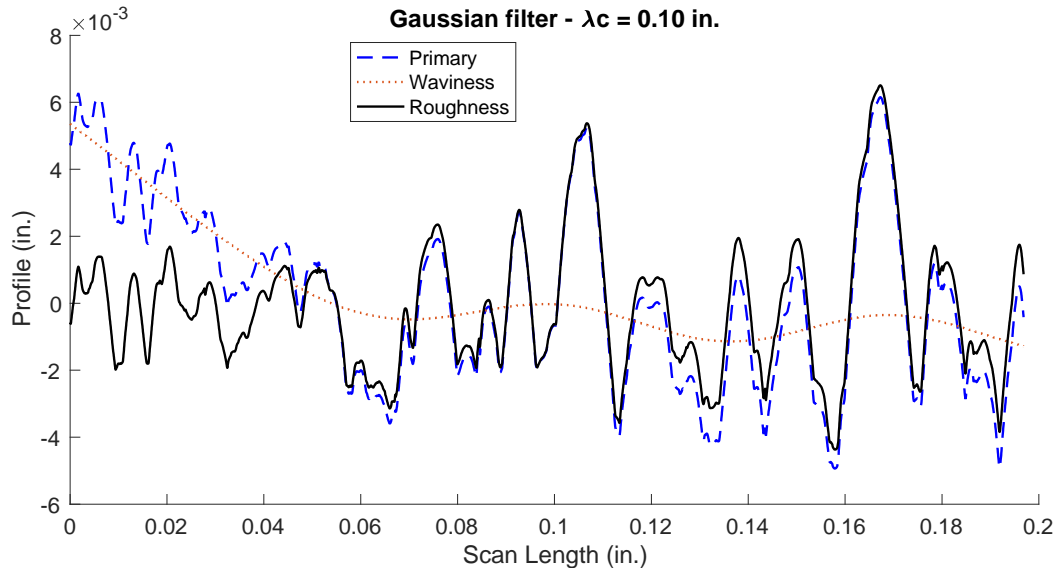


Figure 3.3. Typical linear filtered surface profiles for: (a) TEC1 bar and (b) BLK bar.

For the comparison of surface profile characteristics, it was necessary to quantify the surface roughness with relevant roughness parameters. In this study, the variables of interest were

the amplitude of the profile, the spacing between peaks and valleys, as well as the symmetry of the surface profile with respect to the mean line. Based on recommendations from the literature (Gadelmawla et al, 2002; I.S.O, 1997; Bhusan, 2000; ASME, 2010), 5 linear parameters: R_a , R_z , R_{ku} , HSC and R_{sm} were evaluated by taking the average of all measured specimens. On each specimen, three areas between ribs were scanned. On each area between ribs, three 0.20-inch-long lines with a spacing of 0.002 in. (50 μm) were scanned. A schematic diagram of the measured areas is presented in Fig 3.4.

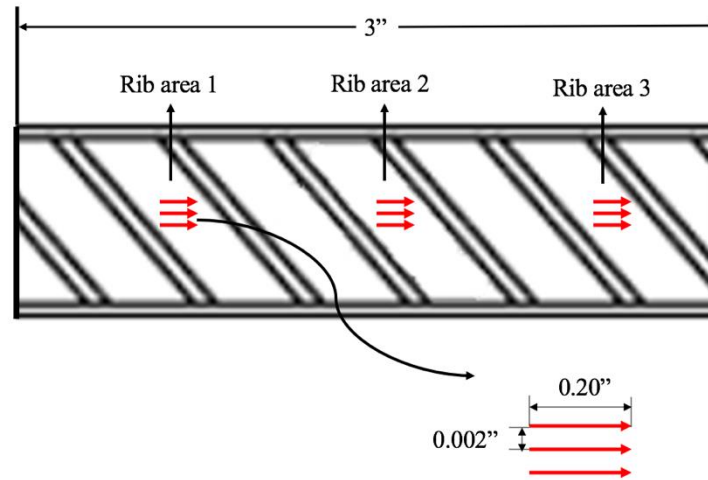


Fig 3.4: Schematic diagram of areas for measurement on each specimen.

The concept and calculation method of each parameter is introduced in detail as follows:

Amplitude Parameters:

- *Arithmetic average height (R_a)*

The arithmetic average height, R_a , is defined as the average deviation of the roughness irregularities from the mean line over one sampling length, l . Fig 3.5 below is a graphical definition of R_a . In the broader civil engineering literature, R_a is one of the most widely recommended and used parameters to evaluate surface roughness profiles for various materials, such as aesthetic

bracket materials, ceramics, textured epoxy coated reinforcement bars, etc. (Zinelis et al, 2005).

The value of R_a for each sampling length l is calculated as

$$R_a = \frac{1}{n} \sum_{i=1}^n |y_i| \quad (3.1)$$

where, n is the number of data points, y_i is the deviation from the mean line after filtering.

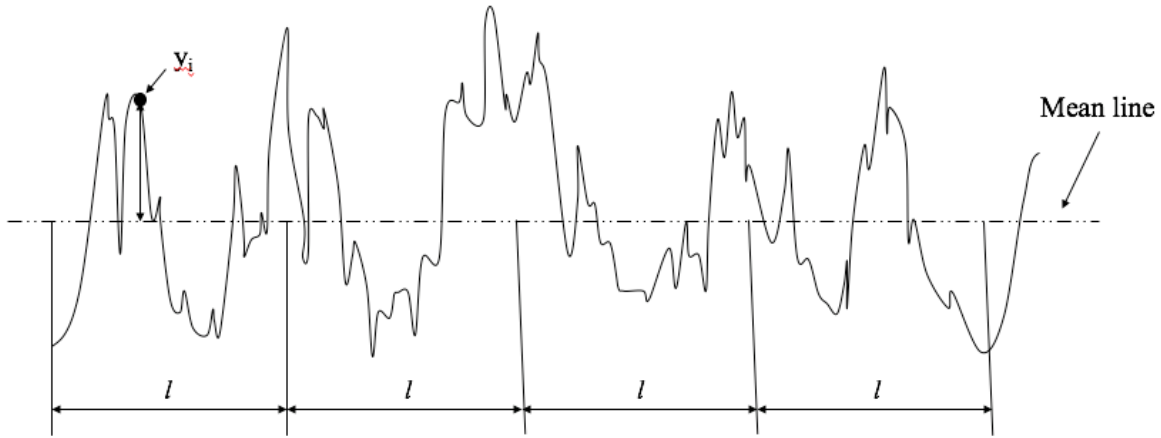


Fig 3.5: Graphical definition of R_a .

- *Maximum height of the profile (R_z)*

R_z is defined as the difference in height between the highest peak and the lowest valley along every sampling length. In this investigation, the formula used to calculate the R_z value is:

$$R_z = \frac{1}{n} \left(\sum_{i=1}^n p_i - \sum_{i=1}^n v_i \right) \quad (3.2)$$

where n is the number of data points, p_i is the height of the highest peak within one sampling length, and v_i is the height of the lowest valley. Fig 3.6 shows the graphical definition of R_z .

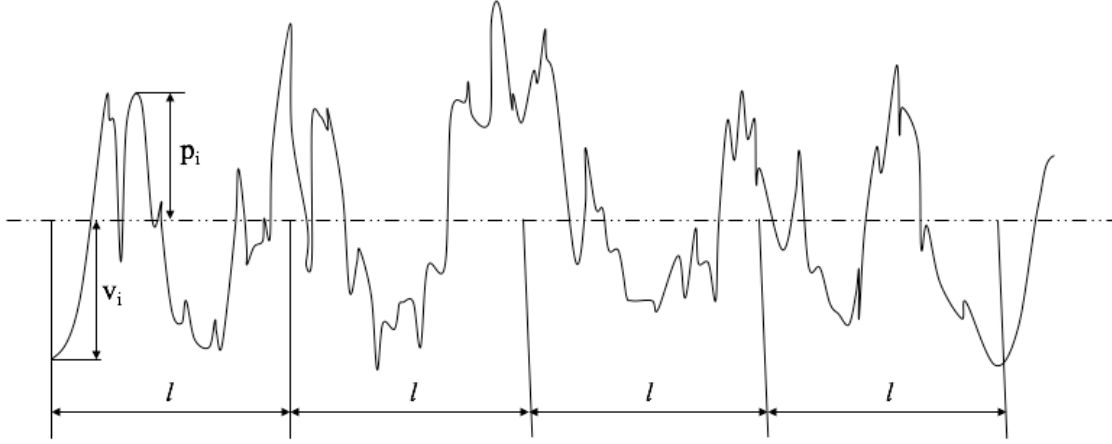


Fig 3.6: Graphical definition of R_z .

Compared with R_a , R_z is more sensitive to outliers in surface profile heights. For example, two surface profiles may have the same R_a values but completely different extreme values of R_z .

- *Kurtosis* (R_{ku})

R_{ku} measures a different aspect from that of R_a and R_z regarding the surface roughness. Instead of measuring the magnitude of the heights, R_{ku} is a measure of symmetry of the surface profile with respect to the mean line. It provides the shape characteristics of the surface profile in both vertical and horizontal directions other than height magnitudes. If the R_{ku} value is smaller than 3, there are few peaks and valleys, while if the value is greater than 3, there are relatively many high peaks and low valleys (Gadelmawla et al., 2002).

In this research, R_{ku} is taken with respect to the mean line of the filtered profile, which has a value of zero. The formula used to compute R_{ku} is shown below:

$$R_{ku} = \frac{1}{NR_q^4} \left(\sum_{i=1}^N Y_i^4 \right) \quad (3.3)$$

where, R_q is the root mean square roughness calculated as

$$R_q = \sqrt{\frac{1}{n} \sum_{i=1}^n Y_i^2} \quad (3.4)$$

where n is the number of data points, Y_i is the deviation from the mean line after filtering.

Fig 3.7 below demonstrates the characteristics of R_{ku} . Fig 3.7 (a) represents the case when $R_{ku} > 3$ and Fig 3.7 (b) represents the case when $R_{ku} < 3$. The two surface profiles have almost the same values of R_a and R_z but look completely different. Compared with Fig 3.7 (b), Fig 3.7 (a) has more peaks and valleys. This surface profile characteristic cannot be reflected by R_a and R_z .



(a)



(b)

Fig 3.7: Geographic definition of R_{ku} when: (a) $R_{ku} > 3$; (b) $R_{ku} < 3$.

Spacing Parameters

- *Mean width of profile elements (R_{sm})*

R_{sm} is a measure of the density of profile elements in the horizontal direction. It is defined as the mean value of the profile element width X_s within one sampling length (EN ISO 4287, 1997). The formula for computing R_{sm} is

$$R_{sm} = \frac{1}{m} \sum_{i=1}^m X_{si} \quad (3.5)$$

where, m is the number of measured surface heights and X_{si} is the element width within each sampling length.

It is specified in EN ISO 4287 (1997) that a height discrimination of 10% of R_z and a spacing discrimination of 1% of the sampling length need to be applied. The geographic definition of R_{sm} is given in Fig 3.8 below.

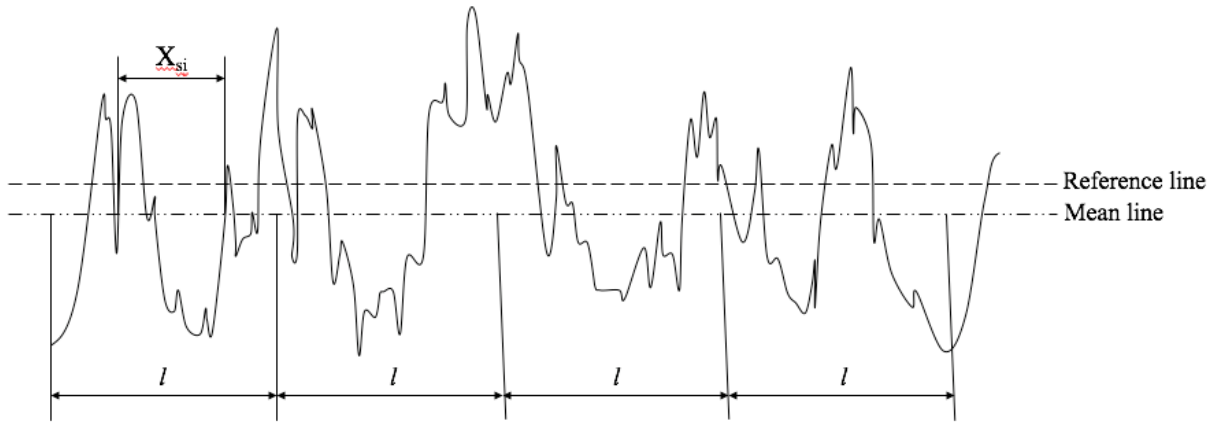


Fig 3.8: Geographic definition of R_{sm} .

- *High Spot Count (HSC)*

HSC is defined as the number of high regions of the surface profile above the mean line or another line which is parallel to the mean line per unit length (Gadelmawla et al, 2002).

It is a good indicator of the density of the high peaks of the surface profile, as for the textured bar, a higher density of peaks may indicate a higher bonding strength to retain concrete. The reference line for HSC is selected as the 10% R_z to keep it consistent with the reference line of R_{sm} . The geographic definition of HSC is given in Fig 3.9.

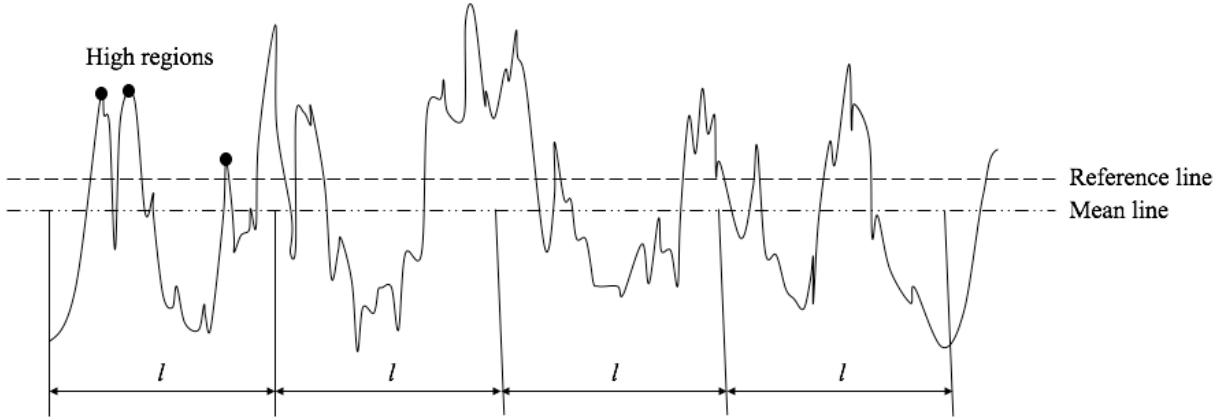


Fig 3.9: Geographic definition of HSC.

For all of the linear parameters discussed above, the roughness profile of three lines were measured for each rib area. However, due to the fact that those parameters were only for linear measurements, it was unknown whether they are accurate enough to describe the characteristics of the 3-D surface of reinforcement bars. To provide some insights on the accuracy of the linear parameters, two 3-D roughness parameters, S_a and S_z , were calculated and compared with R_a and R_z . The formulas used for S_a and S_z are as follows:

$$S_a = \frac{1}{MN} \sum_{k=1}^M \sum_{j=1}^N |Z_{jk}| \quad (3.6)$$

where, M and N are the measured element points along the two horizontal directions, and Z_{jk} is the height of each element point.

$$S_z = S_p + S_v \quad (3.7)$$

where, S_p is the maximum height in the evaluated area with respect to the mean surface, and S_v is the absolute value of the minimum height in the evaluated area with respect to the mean surface (ASME B46.1, 2009).

3.2.2 Phase I Surface Roughness Quantification Results Discussion

Fig 3.10 below presents comparison of 1-D roughness parameters R_a , R_z and R_{ku} between No.5 and No.8 TEC and BLK bars. From Fig 3.10a and 3.10b, the plots of R_a and R_z appeared to have very similar trends. The values of both parameters of TEC bars were more than four times those of BLK bars, indicating that the TEC bars are significantly rougher than BLK bars. From the aspect of symmetry, as shown in Fig 3.10c, the TEC bar and BLK bar had very close R_{ku} values, except for the No.5 BLK bar. Since the R_{ku} value was close to 3 for TEC bars of both sizes and No.8 BLK bars, their surfaces had as many peaks as valleys, indicating a symmetry about the mean line. However, Fig 3.10c did not show any distinct difference of R_{ku} between the TEC and BLK bars.

From Figure 3.10 it could be seen that there was consistency between No.5 and No.8 bars results. For TEC bars, the percent differences between No.5 and No.8 bars for all three parameters, R_a , R_z , and R_{ku} , were 4.38%, 1.27%, and 0.46%, respectively. However, for the BLK bar, the three parameters for the No.8 bar were 2.1, 2.2, and 1.7 times of those for the No.5 bar. Hence, it could be concluded that there was no significant difference between No.5 and No.8 for TEC bars while the surface roughness of the No.8 BLK bar was about twice that of the No.5 BLK bar. Furthermore, the higher R_{ku} value of No.8 BLK bar indicated that there was relatively more high peaks and low valleys for No.8 BLK bars than for No.5 BLK bars.

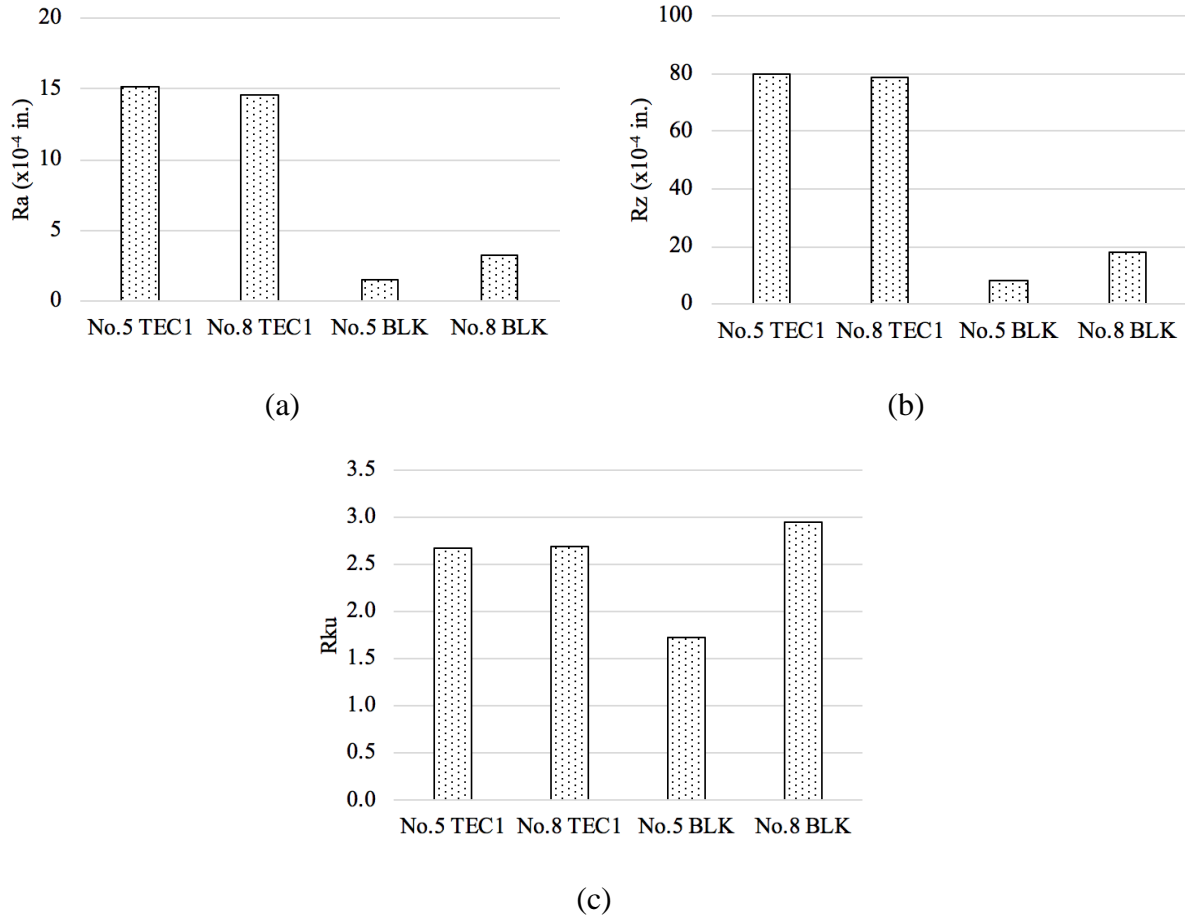


Fig 3.10: Comparison of (a) R_a , (b) R_z , and (c) R_{ku} for No.5 & No.8 TEC1 and BLK bars.

As for the spacing parameters, Fig 3.11 below displays the comparison of HSC and R_{sm} between No.5 and No.8 TEC1 bars. The differences between No.5 and No.8 TEC bars were negligible, with a percent difference of 2.49% in HSC and 2.05% in R_{sm} . There were about six high peak regions per sampling length for the TEC bars and the mean spacing between adjacent peaks and valleys was about 0.45.

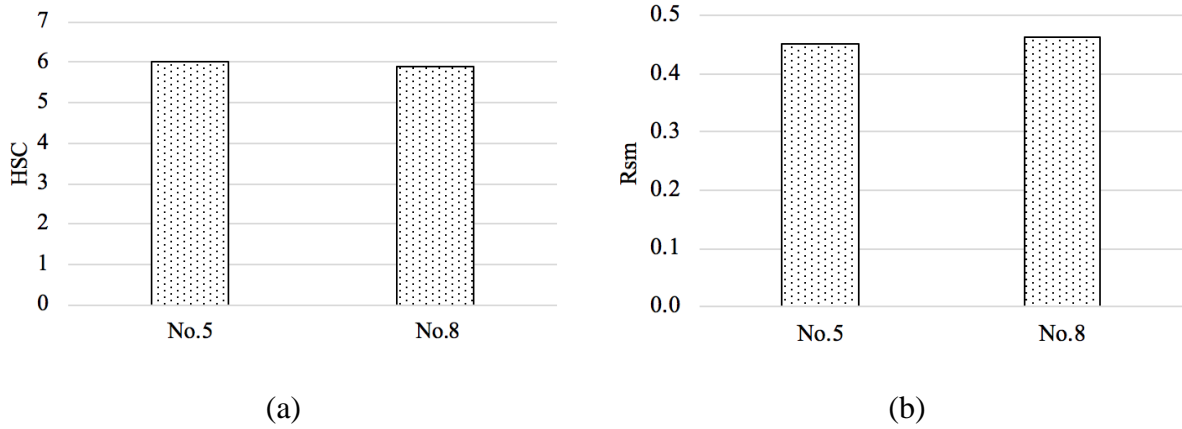
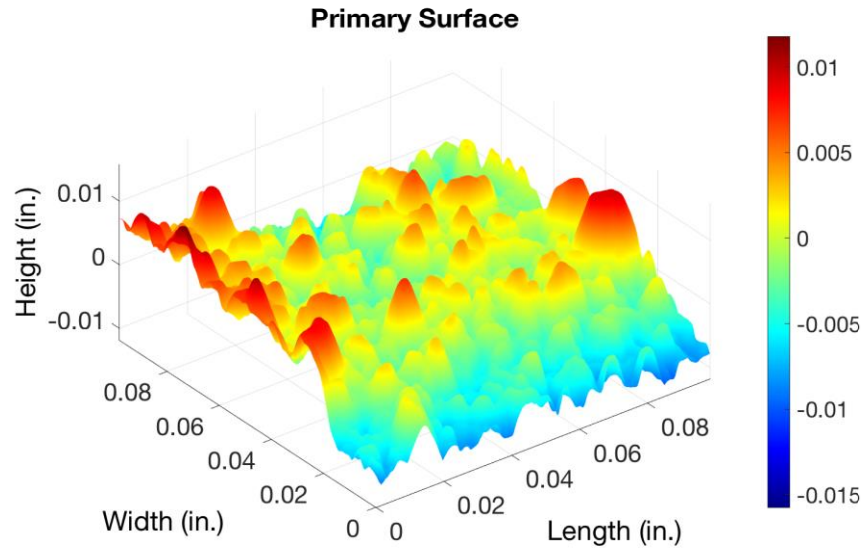
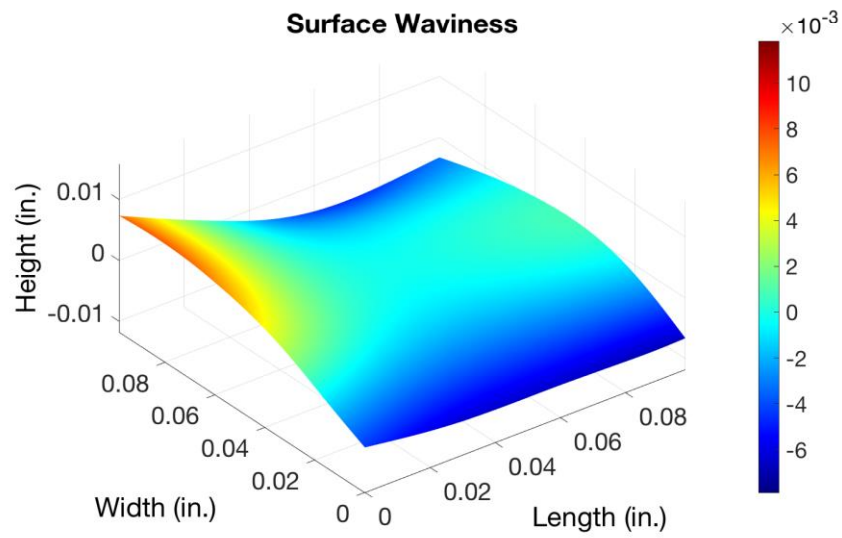


Fig 3.11: Comparison of spacing parameters (a) HSC and (b) R_{sm} between No.5 and No.8 TEC1 bars.

Apart from 1-D roughness parameters, 3-D roughness parameters were also calculated for TEC bars to check the consistency between No.5 and No.8 TEC bars as well as the consistency between the R_a and S_a , and the R_z and S_z values. It was important to investigate whether the 2-D and 3-D parameters yielded consistent patterns. Due to the limited space between the ribs of the rebar, an area of 0.10 in. x 0.10 in. (2.5mm x 2.5mm) was used for the investigation for each of the No.5 and No.8 TEC bars. Fig 3.12 displays a typical 3-D raw primary surface, surface waviness, and filtered surface profiles for a No.5 TEC bar.



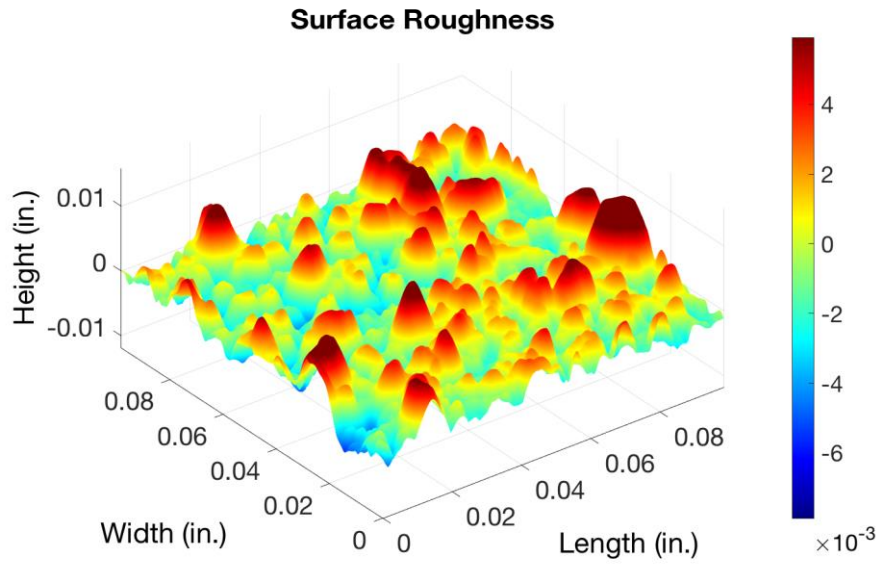
(a)



(b)

Fig 3.12: (a) Raw primary surface; (b) surface waviness; (c) filtered surface roughness of a typical No.5 TEC1 bar.

Fig 3.12 (cont.)



(c)

The comparison of the 2-D and 3-D parameters for No.5 and No.8 TEC1 bars is shown in Fig 3.13. In Fig 3.13a, although the values of R_a and S_a for no.5 TEC1 bars were different by 21.2%, the difference for No.8 TEC bars was negligible. However, in Fig 3.13b, the S_z values for both No.5 and No.8 bars were almost twice the R_z values. This greater difference between the R_z and S_z values was likely to be attributed to the much larger amount of roughness measurement points in the 3-D measurement. Since deeper peaks and valleys were more likely to be included in the measurement, there were more extreme values involved.

On the other hand, the comparison between the No.5 and No.8 TEC bars showed that the R_a and R_z values for both sizes were consistent. However, there was a 23.55% difference in the S_a value and a 17.46% difference in the S_z value between No.5 and No.8 bars. Therefore, from the 3-D measurement, No.5 TEC bars showed a higher roughness than No.8 TEC bars although the 2-D parameters showed a consistency in the roughness of the two bar sizes.

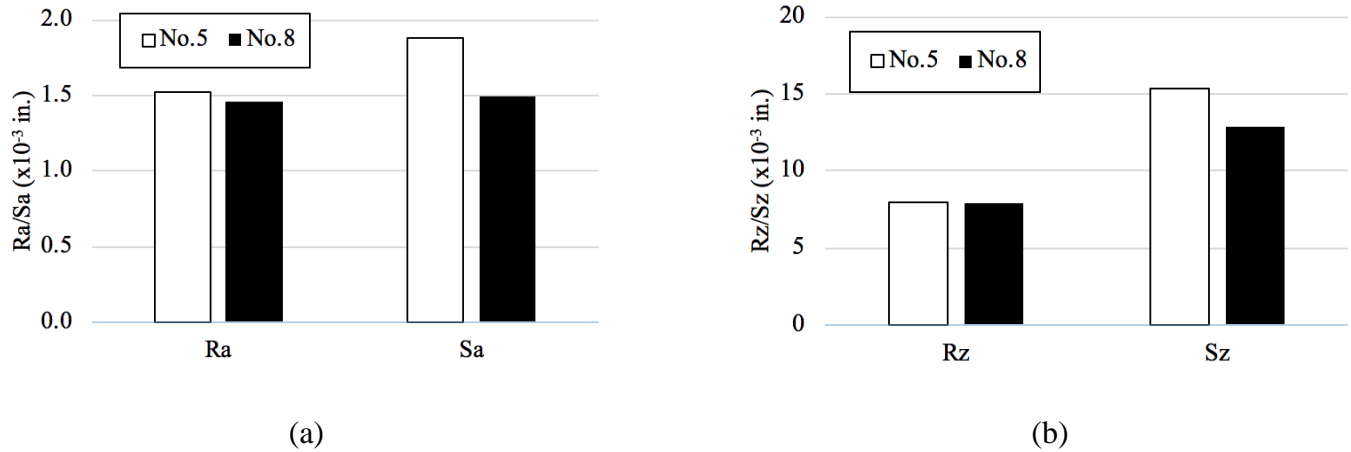


Fig 3.13: Comparison of (a) R_a and S_a ; (b) R_z and S_z between No.5 and No.8 TEC1 bars.

3.2.3 Coating Thickness Measurement

In the exploratory study by Kim and Andrawes (2019), it was observed that some part of the coating at the bonded region of the TEC1 bar was peeled off. One possible cause of this phenomenon was that the coating thickness of the epoxy “green” base layer of the coating might have reduced due to the roughness application procedures. To investigate whether there was a distinct difference in the coating thickness of SEC and TEC1 bars, the thickness of the rebar coating was measured with the Zeiss AxioScope A1 inspection light microscope, as shown in Fig 3.14. Images could be obtained from a Zeiss AxioCam MRc Color CCD camera and postprocessed using the Zeiss AxioVision LE software. After the microscopic images of the

specimen cross section were taken, the measuring tool in the software was used to determine the thickness of the rebar coating.



Fig 3.14: Zeiss AxioScope A1 inspection light microscope (the Imaging Technology Group, 2020).

The coating thickness measurements were performed on 1-inch long specimens obtained from random locations on the same batches of rebars used in the study by Kim and Andrawes (2019). To explore whether applying the roughening particles on the top of the base smooth epoxy coating of the TEC1 bars impacted the thickness of the base coating, two specimens of SEC and TEC1 bars of No.5 and No.8 sizes were measured. Twelve measurements were conducted along the perimeter of each No.8 specimen and seven measurements were conducted along the No.5 specimens, as shown in Fig 3.15. The average of all the measurements were taken for each type of rebars. Fig 3.16 presents the typical microscopic images of SEC and TEC1 cross sections with the measured coating thickness values.

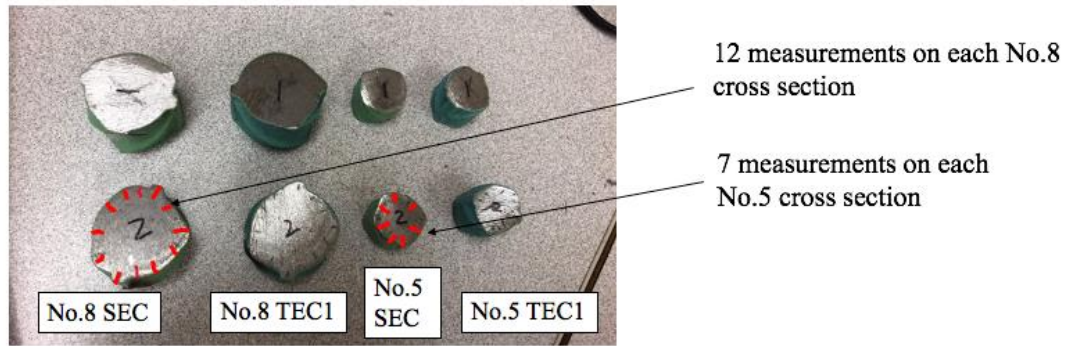


Fig 3.15: Specimens used for coating thickness measurement.

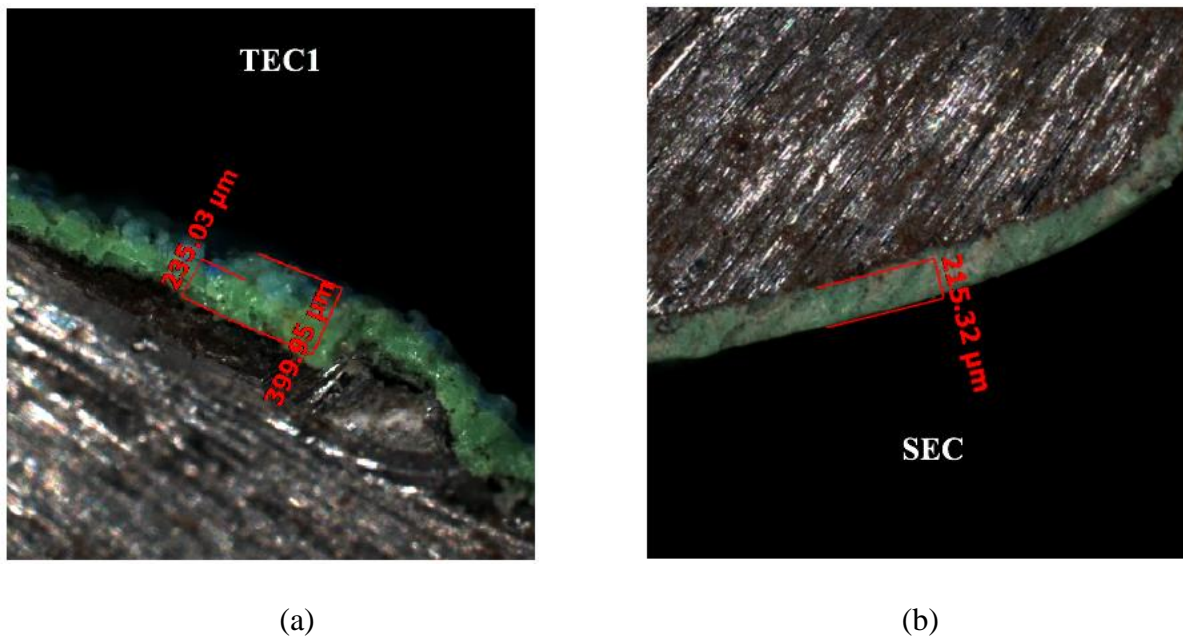


Fig 3.16: Microscopic images of rebar cross section and the measured coating thickness for (a) TEC1 and (b) SEC bars.

As shown in Fig 3.16, the coating of the TEC1 bar was much rougher than that of the SEC bar, which was quite even. On the surface of the TEC1 bar base epoxy coating (green layer), it could be observed that there were some coarse blue particles which contributed to the surface roughness of the TEC1 bars. Fig 3.17 displays the average measured coating thickness of the two specimen sets. “TEC total” denotes the total thickness of the TEC1 coating including the

blue coarse particles, while “TEC Green” represents the thickness of the TEC1 base epoxy coating without the blue coarse particles on top.

From Fig 3.17, it can be seen that No.5 and No.8 bars had very similar coating thickness. The differences of the coating thickness between No.5 and No.8 bars for SEC, TEC Green, and TEC Total, respectively, were 9.92%, 3.87%, and 1.62%, respectively. These measurements indicated that the difference in bar size did not significantly affect the coating thickness.

In addition, the coating thickness of the SEC and TEC1 bars were compared to explore whether adding the polymeric particles had an impact on the thickness of the base epoxy layer in TEC1 bars. The difference of the No.5 bar between SEC and TEC Green was 6.40% while that of the No.8 bar was 7.40%, both of which were relatively small. Therefore, it can be concluded that there was no significant difference in the epoxy coating thickness between SEC and TEC1 bars.

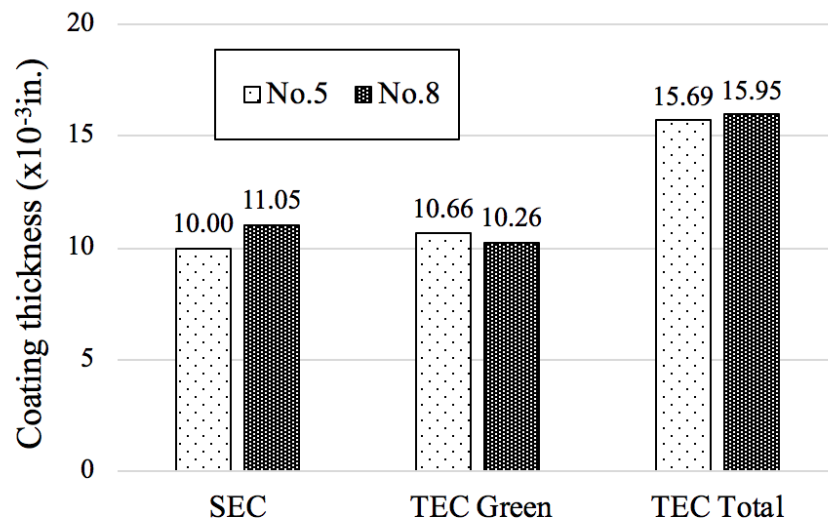


Fig 3.17: Coating thickness comparison of No.5 and No.8 SEC and TEC bars.

3.3 Phase II Study

In Phase II study, a comprehensive comparative study was conducted on a total of six types of TEC bars (TEC1-TEC6) coated with different texture patterns. TEC1-TEC3 were coated by one particular manufacturer, while TEC4-TEC6 were coated by a different manufacturer. The same polymeric powder, however, was used to create the texture of all six TEC bars. The size and density of the powder applied were varied to create bars with different texture and roughness. However, since the coating application procedure is proprietary, it will not be discussed in this study.

3.3.1 Microscopic Images of TEC1-6 bars

Although 2-D and 3-D quantitative analysis methods had been developed, they did not provide insights on all aspects of the rebar surface characteristics, such as color, voids, coating pattern, etc., any of which may have a significant impact on the bond-slip behavior of the bar. As a result, it was necessary to examine the texture of the bars visually. As had been done in the coating thickness study, TEC bar segments were placed under the Zeiss AxioScope A1 inspection light microscope, which has been shown in Fig 3.14, to be observed with a 2.5x objective lens. Images were snapped from a Zeiss AxioCam MRc Color CCD camera and postprocessed using the Zeiss AxioVision LE software. The microscopic images of all six types of bars are shown in Fig 3.18.

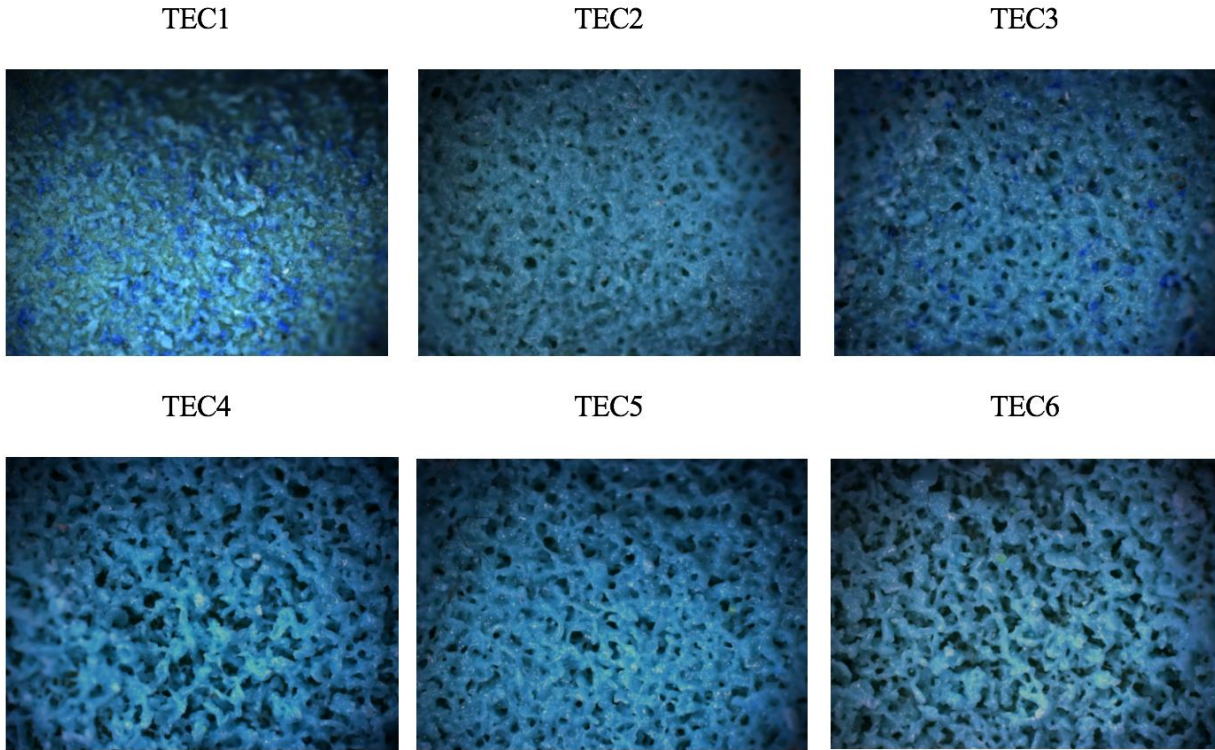


Fig 3.18: Microscopic images of TEC1-6 bars.

As TEC1-3 bars came from the same manufacturer, there were different amounts of blue particles on their surfaces, which might have affected the surface roughness to some extent. TEC1 had the largest amount of the blue particles while TEC2 had almost negligible amount of the blue particles. The surface profiles of all TEC bars, except that of TEC1, showed voids with various densities and sizes. TEC4-6 appeared to have larger voids than TEC2 and TEC3, with the voids of TEC5 being slightly smaller than those of TEC4 and TEC6. To evaluate the impact of variation of the TEC bars' surface texture on their roughness, the surface profiles of the bars were measured in 2-D and 3-D, and quantified by roughness parameters.

3.3.2 Coating Adhesion Measurement

There had been many studies conducted on the bond-slip behaviors of reinforcing bars with concrete, as has been described in Chapter 3 of this thesis. However, most of them only studied the bond-slip mechanism between the rebar itself and the surrounding concrete. For epoxy-coated bars, there are two interfaces: 1) the interface between the coating and the steel substrate, and 2) the interface between the coating and the surrounding concrete. Therefore, it was necessary to explore the adhesion between coating and steel substrate. Although there are multiple test standards and various research studies about the testing of the adhesion between coating and metal substrate (ASTM D3359, 2017; ASTM D 6677, 2018; ASTM D6943, 2015; Cortes et al, 1992; Tex-739-I, 2012), most of the available testing standards only evaluate adhesion qualitatively, instead of quantitatively. The objective of this study is to compare the adhesion strength of the SEC and TEC bars, therefore, a combination of the test methods specified in ASTM D6677 (2018) and the proposed method by Cortes et al. (1992) was adopted in this study to obtain a quantitative evaluation of the coating adhesion. Since the SEC bars and TEC1-3 bars were provided by the same manufacturer, the comparison was made only among these bars to eliminate the effect of possibly different coating application procedures and materials.

Three 3-inch-long specimens were cut on randomly selected locations along each bar. For each type of bars, two bars were randomly selected from each batch. On each specimen, two “X” cuts were made with an intersection angle of approximately 45° on each side. The cuts needed to penetrate the coating completely. A utility knife was held at an approximately the same angle of 45° to shear the coating off from the intersection point of the “X” cut. A diagram of such X cuts is shown in Fig 3.19. For each “X” cut, the coating of both flaps was sheared off . Then the

opening width of the sheared-off coating was measured using the Zeiss AxioVision LE software by taking a microscopic image of the cut opening with the Zeiss inspection A1 light microscope. A typical microscopic image of the cut is shown in Fig 3.20. A large opening width indicated a small coating adhesion strength. To make larger opening widths easier to observe, the utility knife was hammered twice from the same distance at the same angle to apply a larger impact force to shear off the coating while keeping the applied force as uniform as possible.

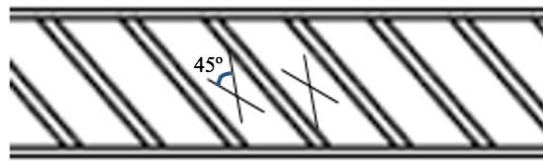


Fig 3.19: A diagram of the two “X” cuts on each side of the specimen.

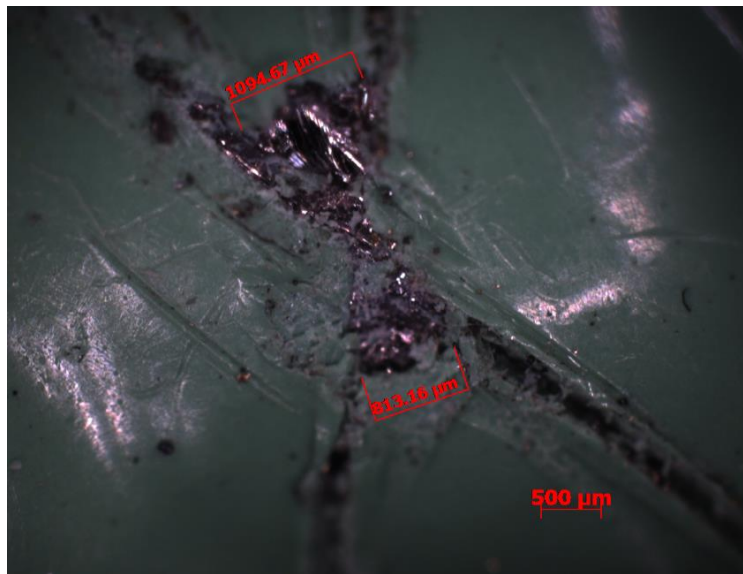


Fig 3.20: Typical microscopic image of the cut.

The average measured opening width for each type of bar is displayed in Fig 3.21. The larger the opening width, the smaller the adhesion between the coating and the steel substrate.

From Fig 3.21, the opening width of the SEC bar was 67.92% greater than the average opening width of TEC1-3 bars, indicating that the SEC bar had a much lower coating adhesion than the TEC bars. Among the TEC bars, TEC2 had the highest average opening width while TEC1 bar had the lowest opening width. This observation demonstrated that of the three types of TEC bars, TEC1 had the highest coating adhesion strength while TEC2 bar had the lowest adhesion strength. The high coating adhesion strength of the TEC1 bar indicated that the coating of TEC1 bar was the hardest to be peeled off.

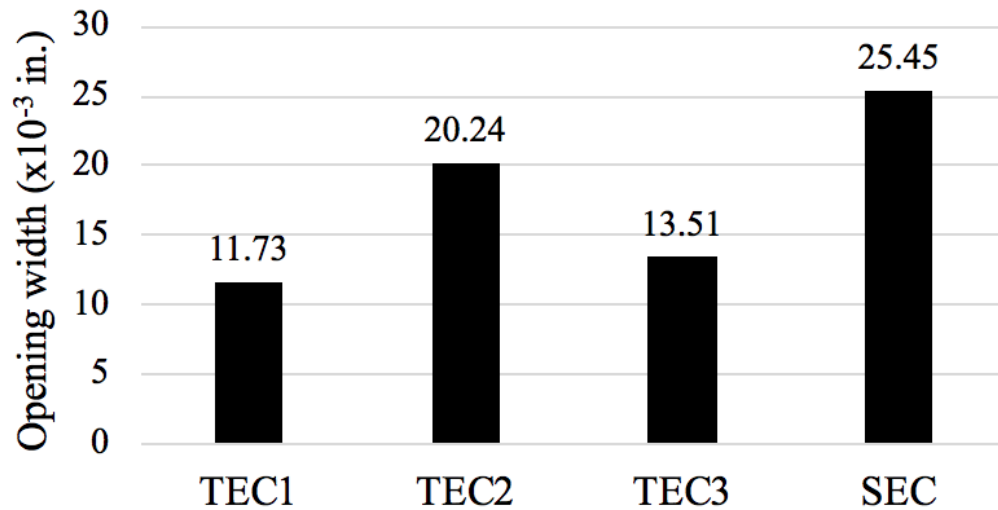


Fig 3.21: Measured average opening width of TEC1, TEC2, TEC3, and SEC bars.

3.3.3 Roughness Quantification & Comparison of TEC1-6 Bars and BLK bars

From the results of Phase I analyses, there were no significant differences in the values of R_{ku} , R_{sm} between TEC1 and BLK bars. Therefore, only R_a , R_z , S_a , and S_z were evaluated for TEC1-6 bars and BLK bars. Since there was only a small difference in the roughness parameter values of No.5 and No.8 bars, Phase II surface roughness analysis was only conducted on No.5

bars. Using the quantification methods described earlier in Section 3.2.1, the values of R_a and R_z for all No.5 TEC bars and BLK bars were calculated and are compared in Fig. 3.22. Both R_a and R_z values of all TEC bars were, on average, at least 3-4 times greater than those of the BLK bars, which matched the findings in the Phase I study. Among TEC1-6 bars, TEC6 had a higher R_a value than the other TEC bars, which indicated the highest roughness, with TEC2 having the second-highest roughness, TEC3 and TEC4 being the next highest, and finally, TEC1 and TEC5 yielding the lowest R_a values. Although the R_z plot exhibited a similar trend with the R_a plot, with TEC5 having the lowest values of R_z , TEC2 had the highest value of R_z instead of TEC6. The R_z value of TEC3 was only slightly lower than that of TEC2, with TEC6 having the next highest R_z value. This observation demonstrated that TEC2 and TEC3 had the largest difference between peaks and valleys, while that of TEC5 was not as distinct.

Based on the microscopic images presented earlier in Fig 3.18, although voids were expected to result in higher R_a and R_z values, TEC4-6 did not necessarily have the highest values of R_a and R_z . TEC6 had the highest value of R_a , but both R_a and R_z values of TEC5 were the lowest among all TEC1-6 bars. Therefore, based on the comparison of the results of TEC1 and TEC5, it was not readily apparent whether the presence of voids had any impact on the surface roughness.

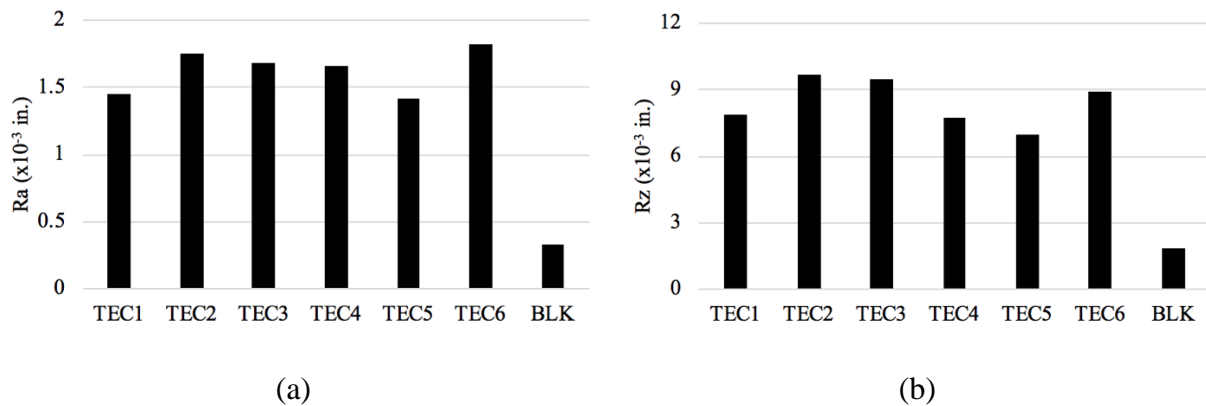
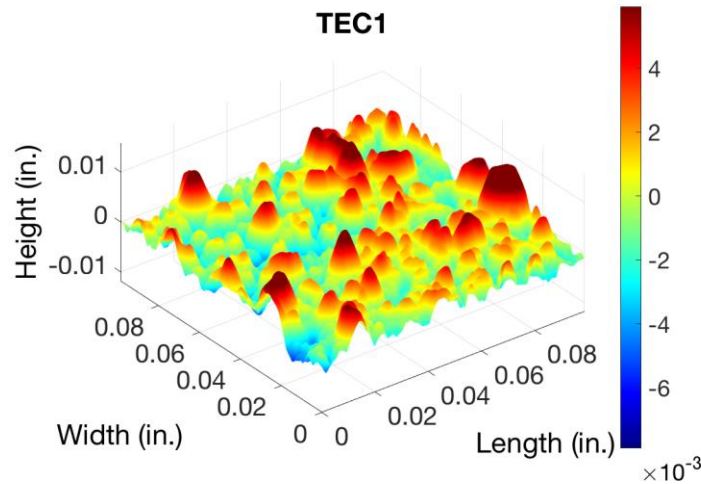


Figure 3.22: Comparison of (a) R_a ; (b) R_z values for all TEC bars & BLK bars.

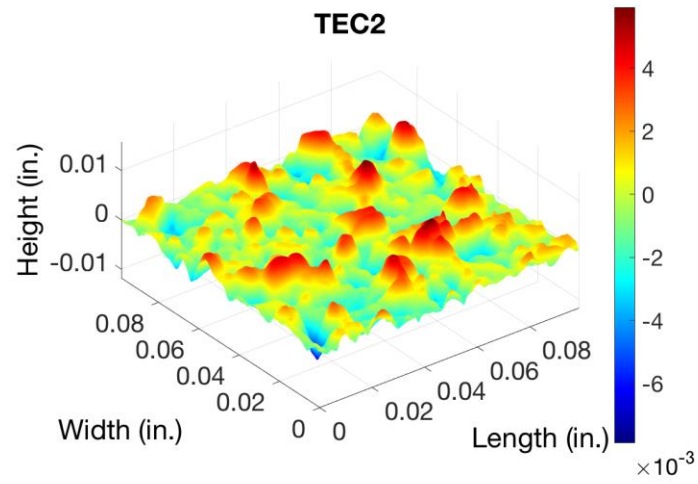
Although the 2-D amplitude parameters R_a and R_z provided certain insights on the bar surface roughness, they did not reflect the spacing between the peaks and their skewness. Two different surface topologies may have the same values of R_a or R_z . To obtain the full picture of the surface roughness, a 3-D analysis was also conducted using the measurement data from the surface profilometer. For each type of TEC bar, an area of 0.10 in. x 0.10 in. (2.5 mm x 2.5 mm) between ribs was measured. A set of longitudinal measurement data 3.94×10^{-4} in. (10 μm) apart in the transverse direction was obtained. Fig 3.23 shows the 3-D surface topology of the six types of TEC bars after the Gaussian filter using MATLAB. Furthermore, to quantify the 3-D comparison of roughness, the 3-D roughness parameters, S_a and S_z , which corresponded to the linear parameters R_a and R_z , were calculated and presented in Fig 3.24.



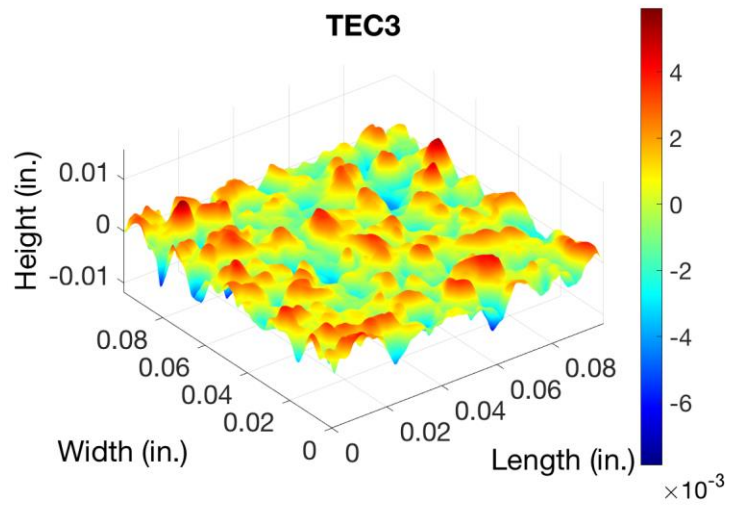
(a)

Fig 3.23: 3-D filtered surface topologies of (a) TEC1; (b) TEC2; (c) TEC3; (d) TEC4; (e) TEC5; (f) TEC6 bars.

Fig 3.23 (cont.)

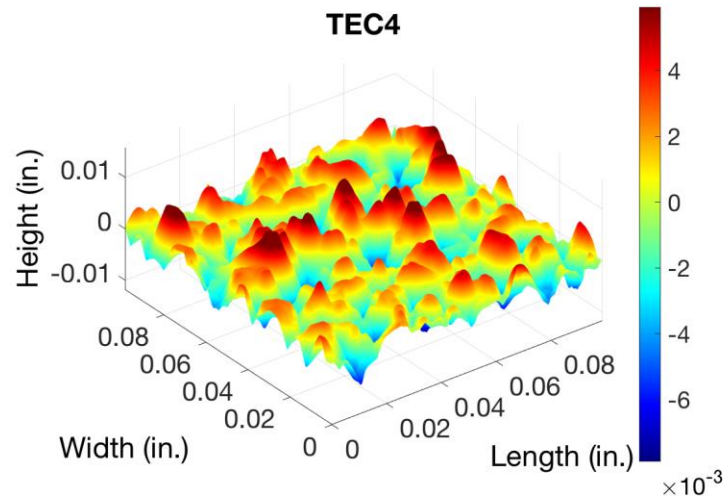


(b)

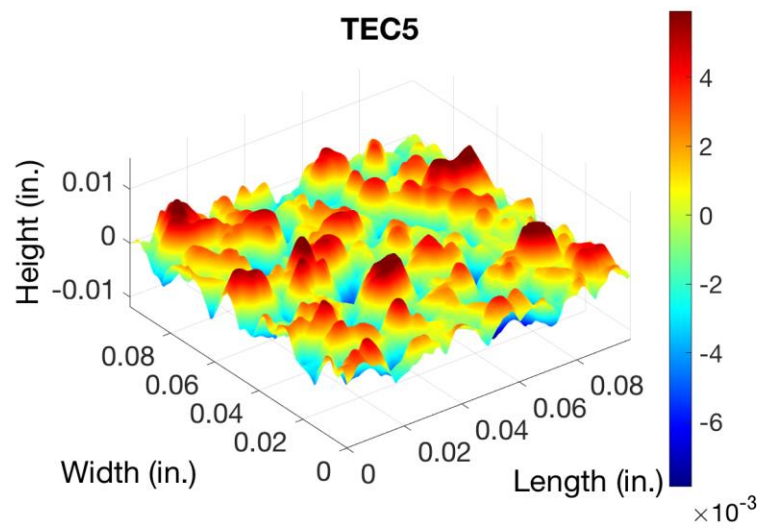


(c)

Fig 3.23 (cont.)



(d)



(e)

Fig 3.23 (cont.)

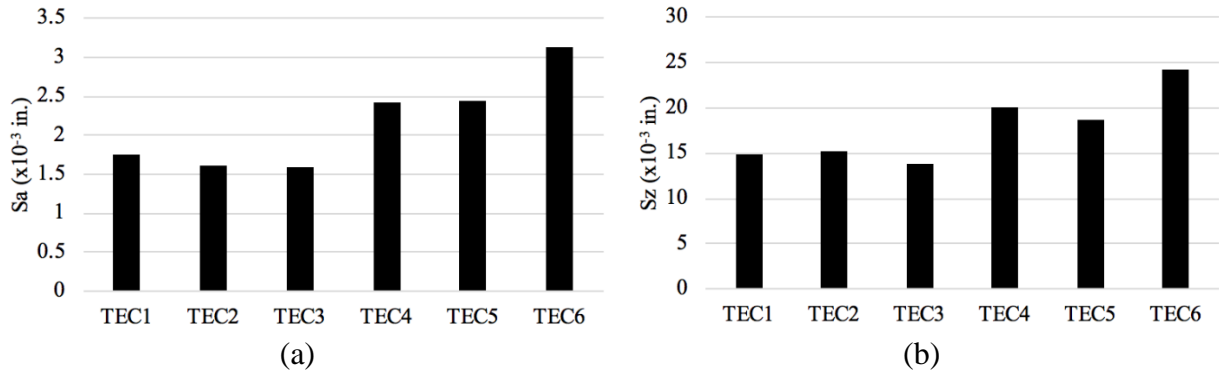
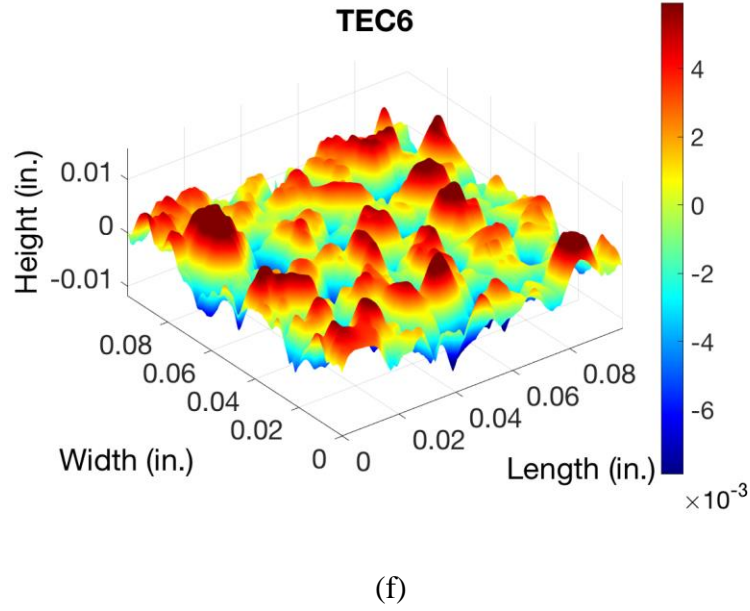


Fig 3.24: Comparison of (a) S_a and (b) S_z values of all TEC bars.

From the 3-D surface topologies of all TEC bars, TEC4-6 bars had higher and denser peaks than TEC1-3 bars, indicating that TEC4-6 bars generally had rougher surfaces. More low valleys (voids) were also visible on the 3-D surface images of TEC4-6 bars (see Fig 3.23). This observation was further confirmed by a distinct difference between TEC1-3 bars and TEC4-6

bars in the values of S_a and S_z displayed in Fig 3.24 where the average S_a and S_z values of TEC4-6 bars were 60.7% and 43% higher than those of TEC1-3 bars, respectively. Among TEC1-3 bars, TEC3 had a slightly higher S_a value than the other two bars, and TEC6 had the highest S_a and S_z values overall. The greater value of S_a indicated an overall higher roughness of TEC4-6 bars, and the greater value of S_z implied that, on average, there was a higher difference between the peaks and valleys on TEC4-6 bars. Of TEC1-3 bars, although they had similar values of S_a and S_z , TEC3 bars had the fewest and lowest peaks while TEC1 bar had relatively more and higher peaks from the 3-D topology images. This observation, which was not reflected in the values of S_a and S_z , indicated the limitation of the roughness parameters in describing surface characteristics. All except TEC1 bars had deep valleys (voids), but the depths of valleys of TEC4-6 bars were noticeably larger than those of TEC2 and TEC3 bars, indicating that TEC4-6 bars had deeper voids. Overall, the 3-D surface topology images reflected that TEC6 bars had the highest level of surface roughness than the rest of TEC bars. This high roughness could result from a combination of high surface peaks and deep voids.

Chapter 4: Pull-Out Tests of Coated and Uncoated Bars

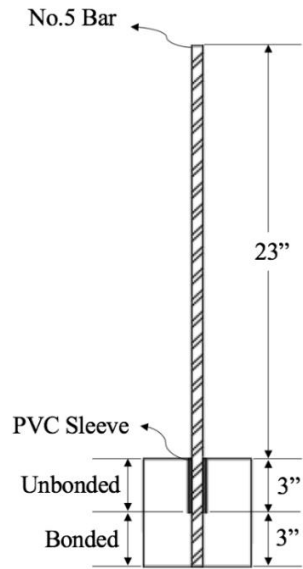
After examining the surface profiles of various TEC bars, it was essential to correlate these profiles with the bond-slip behavior of these TEC bars with concrete. To achieve this objective, a pull-out test program was conducted to compare the bond strength of No. 5 TEC bars with that of SEC bars and BLK bars, all of which were made from Grade 60 steel ($F_y = 60$ ksi, $E = 29000$ ksi). The pull-out tests were conducted in two phases: the first phase tested specimens of TEC1-3 bars, which were from the same manufacturer, to verify the pull-out test results of TEC1 bars by Kim and Andrawes (2019). The second phase was a comprehensive comparison study of all TEC1-6 bars, SEC bars, and BLK bars.

4.1 Phase I Pull-out Tests

4.1.1 Pull-out Specimen Preparation & Test Setup

As per the recommendations of RILEM (1994), the concrete pull-out specimens for No. 5 bars had a diameter of 6 in. with a bonded length of 3 in. The specimens were cast using 6"x12" plastic concrete cylinder molds with half of the height removed. They were casted upside down so that the surface being pulled against the loading frame can be kept flat. Moreover, the unbonded region of the bar was incorporated using PVC sleeves. A standard IDOT concrete mix was used. A schematic diagram of the specimen dimensions, specimen casting, and the testing set-up are shown in Fig. 4.1. A custom-designed frame was used to hold the concrete specimen in place against the bottom of the hydraulic frame when the bar was being pulled. A Linear Variable Differential Transformer (LVDT) was installed at the free end of the concrete specimen to record the slip between the bar end and the concrete bottom surface. The loading rate used was

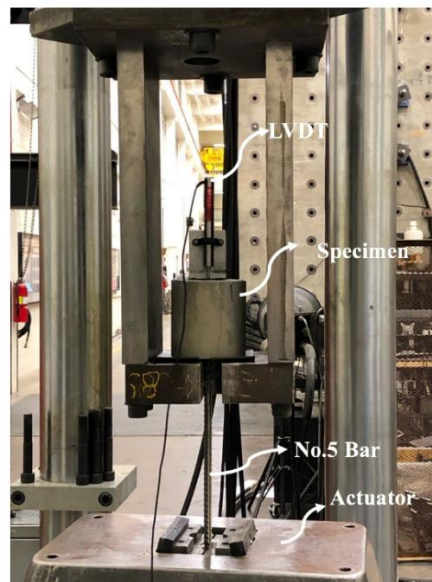
0.0375 in./min. All data points were collected at a rate of 8 Hz. After a significant slip was detected, the bar was manually pulled out from the concrete specimen. A total of six specimens were casted, with two specimens casted for each type of TEC bar.



(a)



(b)

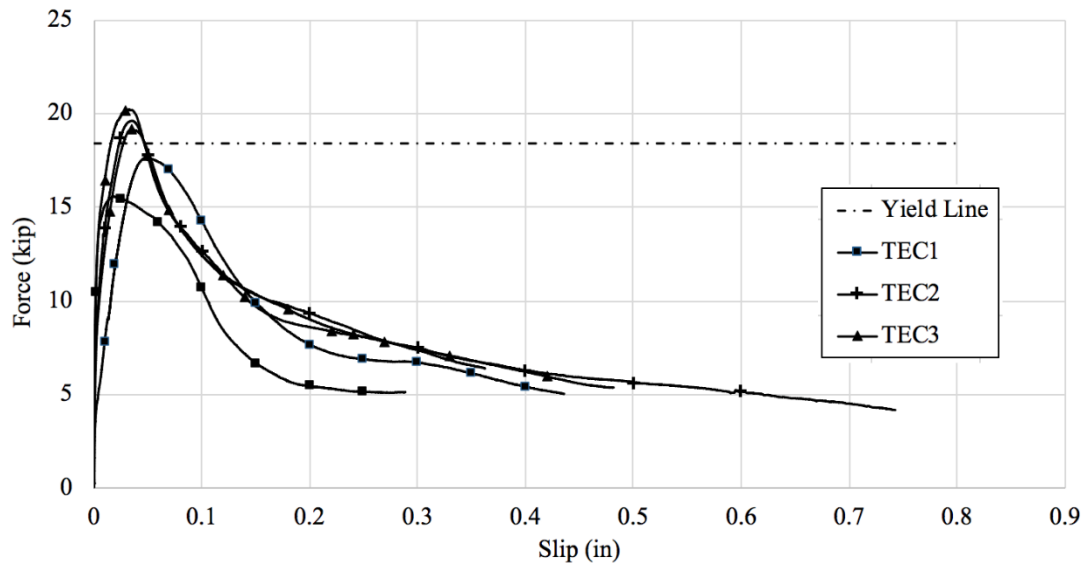


(c)

Fig 4.1: Pull-out test preparation: (a) schematic diagram of the pull-out specimen; (b) specimen casting molds; (c) testing setup.

4.1.2 Phase I Test Results

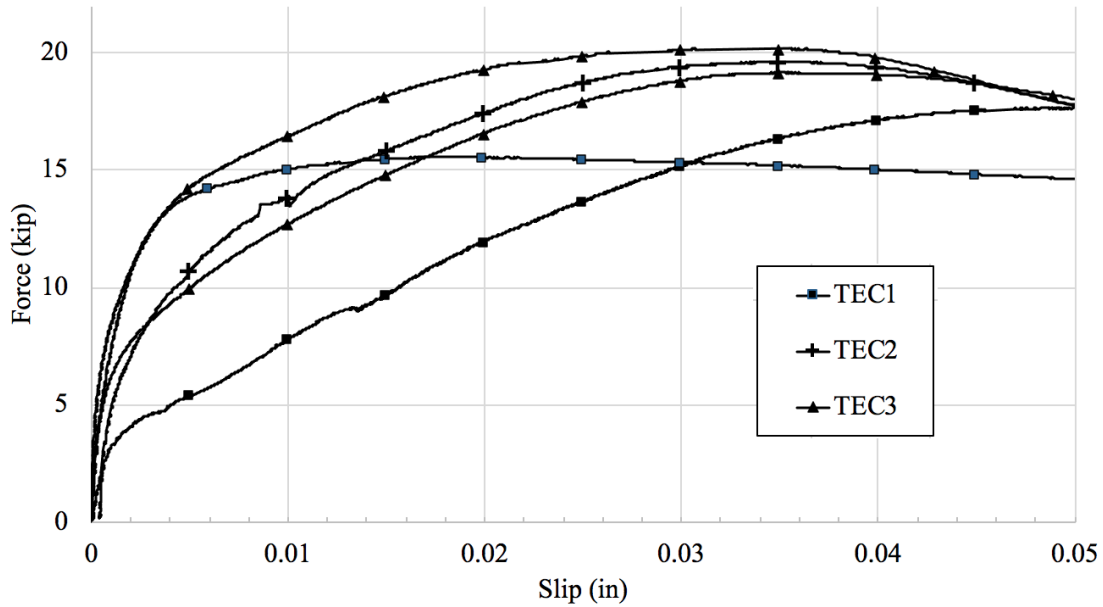
From testing the standard 4"x8" concrete cylinders poured with the same mix at the 14th and 28th days after the pull-out specimens were casted, the compressive strength of concrete at 14 days reached 6.2 ksi, which exceeded the specified minimum 14-day strength of 4.1 ksi. The 28-day concrete compressive strength reached 7.6 ksi. Due to the limitation on the pull-out machine schedule and time, only five bars were tested, including two TEC1 specimens, two TEC3 specimens, and one TEC2 specimen. The end of one of the TEC1 bars, slipped from the top actuator grip during the test and the specimen had to be tested again. However, after the first test, it was uncertain how much damage was sustained by the specimen due to the tensile force, so the data for that specimen was not deemed reliable. The overall pull-out test results and the initial bond-slip curves can be seen in Fig 4.2.



(a)

Fig 4.2: The force-slip curves of the tested specimens: (a) Overall curves; (b) Initial stage.

Fig 4.2 (cont.)



(b)

Based on the initial bond-slip behaviors shown in Fig. 4.2 (b), it can be seen that TEC2 and TEC3 bars exhibited significantly higher bond-slip behavior compared to TEC1 bar in terms of both initial slip resistance and peak strength. Considering the differences in the surface characteristics, it is likely that the improved behaviors are due to the voids on the bars surface and the decreased amount of the blue polymeric particles, as shown in Fig 3.18. A possible explanation is that the decreased blue particles and the voids provide adequate surface friction between the bar surface and the surrounding concrete without causing significant adherence of concrete paste to the bar surface, which could lead to reduced bond strength.

After significant slip was detected, all the bars were manually pulled out. Fig 4.3 presents the bar surfaces for all five specimens after they were pulled out and the microscopic images of the surface at the bonded region for each type of bar. From Fig 4.3a, on all specimens, the coating at the bonded the region was torn off to different extents. For TEC2 and the left TEC3

specimen, the coating on almost every visible rib was completely torn off, indicating strong surface friction between the bar and concrete after initial slip occurred. To examine the bar surface more closely, the surface of the bonded regions was examined under the inspection microscope. Based on observations shown in Fig 4.3b, there was no obvious visual difference in the bonded regions of difference types of TEC bars. For all specimens, some parts of the coating were torn off, especially on the ribs. There were comparable amounts of porous concrete paste remaining on all of the bar surfaces as well, which resulted from concrete crushing between ribs.

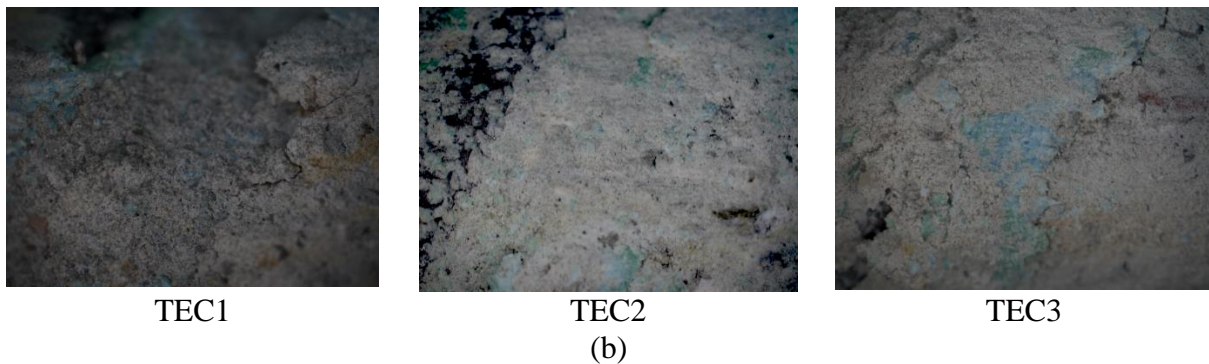
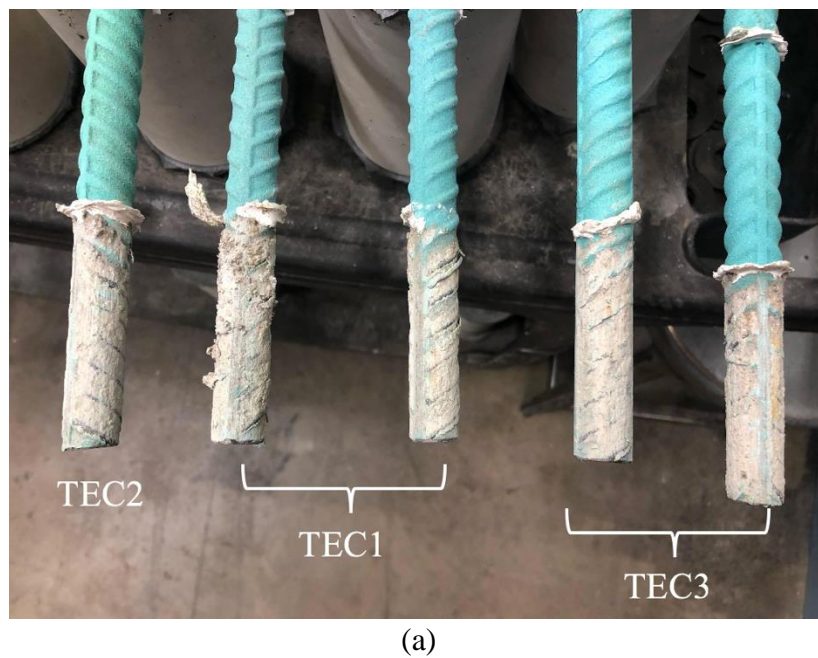


Fig 4.3: Images of the typical bar surfaces at the bonded region after being pulled out: (a) macroscopic image and (b) microscopic image.

Fig 4.4 summarizes the average peak strength for each type of TEC bars. On average, TEC2 and TEC3 bars yielded much higher peak forces than TEC1 bars. Despite their different surface characteristics, TEC2 and TEC3 bars reached yielding and their peak forces were almost identical with a minor difference of only 0.39%. On the other hand, there was a distinct difference of 15.49% on average between TEC1 bar and the other TEC bars in terms of the peak force. Since there was a possible error in the test result of one of the two TEC1 specimens, its result was not considered.

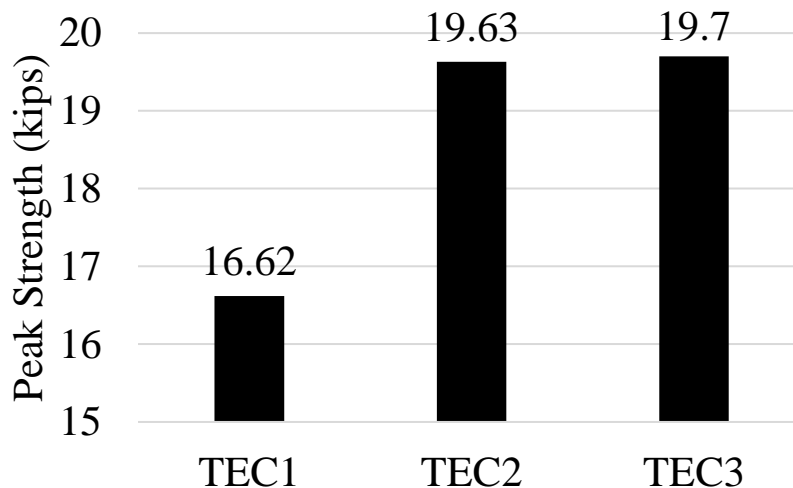


Fig 4.4: Average peak strengths for TEC1-3 bars.

Compared with the previous direct pull-out tests conducted by Kim and Andrawes (2019), the peak forces achieved in this study are higher. Research has shown that a specimen with higher concrete compressive strength typically results in higher bond strength (Kabir and Islam, 2014). The 28-day concrete strength for this study was 7.6 ksi while in the study by Kim and Andrawes, the concrete compressive strength was 5.1 ksi. Therefore, although the direct pull-out tests on the specimens with the TEC1 bars did not yield identical bond-slip curves, the bond-slip behaviors are still comparable. Since on real bridges, cracks usually occur at an early




stage and the rebars may never reach their peak strength in their lifetime, the peak strength was not of primary concern in this study. Instead, the initial slip resistance was more important and was analyzed more thoroughly.

4.2 Phase II Pull-Out Test

Phase II study was a comprehensive set of tests of BLK, SEC and all TEC bars, using the same specimen dimensions and testing set-ups as in Phase I. Three batches of specimens were tested, each comprising eight specimens, including one BLK bar, one SEC bar, and six TEC bars (TEC1-TEC6) with varying concrete compressive strength. Batches 1, 2, and 3 had a compressive strength of 5.8 ksi, 9.2 ksi, and 8.3 ksi, respectively. A summary of all three batches of specimens is presented in Table 4.1.

For the direct pull-out test, there are two possible failure modes: splitting failure and pull-out failure. For higher-strength concrete or concrete with small cover, splitting failure is more likely to happen (Lundgren, 2005). After running tests for Batches 1 and 2, it was found that the majority of failures were occurring due to splitting of the specimens. To ensure that both failure modes were well represented in the test data, Batch 3 specimens were confined prior to testing using carbon fiber reinforced polymer (CFRP) sheets. The CFRP sheet had a ply thickness of 0.049 inches and an ultimate elongation of 0.98%. The tensile modulus and tensile strength of the CFRP sheets were 13000 ksi and 135 ksi, respectively. The specimens were confined with 2 layers of CFRP sheets for a height of 4 inches starting at the bonded region as depicted in Table 4.1. The CFRP was applied using the wet-layup method.

Table 4.1: Summary of the three test batches.

	Batch 1	Batch 2	Batch 3
Confinement	Unconfined	Unconfined	Confined with 2 layers of CFRP
28-day f'_c (ksi)	5.8	9.2	8.3
Specimen			

4.2.1 Pullout Test Results: Peak Strength

Fig 4.5 provides a comparison of the peak strength of the bars for the three batches. In Batch 1, the SEC, TEC1, TEC2, and TEC6 specimens failed due to concrete splitting while the BLK, TEC3, TEC4, and TEC5 specimens failed in the pull-out mode. Images of the two failure modes are presented in Fig 4.6. The nominal yield strength of No.5 rebar was 18.4 kips. In the specimens which failed in the pull-out mode, only TEC3 specimen experienced steel yielding, with a peak strength of 4.4% greater than the yielding force while the BLK, TEC4 and TEC5 specimens reached peak strengths of 1.8%, 2.0% and 16.4%, respectively lower than the yield strength of the rebars. TEC5 developed a significantly lower peak strength compared to the other specimens which failed in the pull-out mode. Of the specimens with splitting failures, only the force of TEC2 specimen reached the yielding force.

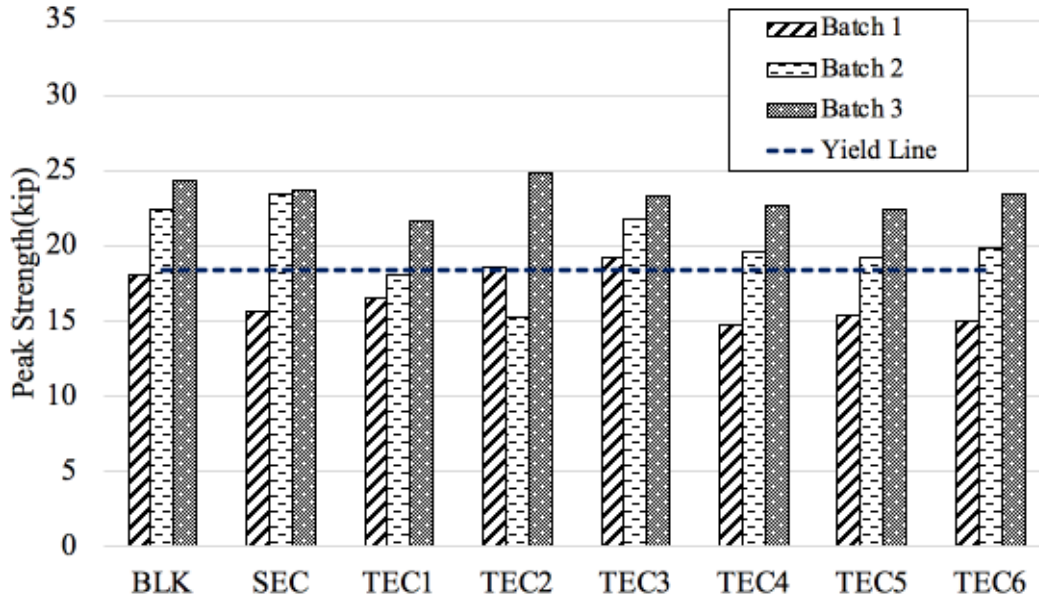


Fig 4.5: Comparison of the peak strength of all bar types in the three batches.



Fig 4.6: Two failure modes of the specimens: (a) pull-out failure, and (b) splitting failure.

In contrast, Batch 2 had the highest concrete compressive strength of all batches. While all six TEC specimens experienced splitting, only BLK and SEC specimens experienced pull-out failure. This was probably attributed to the fact that high-strength concrete was more susceptible to splitting failure (Lundgren, 2005). The combination of the high roughness of the TEC bars and

the high strength of concrete might have contributed to the splitting of all TEC specimens. Additionally, all specimens except TEC1 and TEC2 experienced yielding before failing. This high yielding rate could be due to the high strength of Batch 2 concrete mix. Among all specimens that experienced yielding, TEC5 exhibited the lowest peak strength, only 4.7% higher than the yielding stress. This observation confirmed the results obtained in Phase I that TEC5 developed a lower peak strength than the other specimens. Another observation worth noting was that in Batch 2, although the adhesion and friction between the coating and the concrete decreased due to the smooth surface of the SEC bar, the SEC bar still developed a peak strength higher than that of the rest of the bars. Since the bond between coating and concrete comprises three components: 1) adhesion, 2) friction, and 3) mechanical interaction, or bearing force (Lutz and Gergely, 1967), this observation demonstrated that the bearing force played a more important role in developing the bond strength than the other two components in this test.

In Batch 3, where the specimens were confined, all specimens failed in the pull-out mode. Although micro-splitting was observed in some of the specimens, the CFRP wraps still effectively prevented the splitting failures. In this batch, all of the specimens experienced yielding. TEC2 reached the highest peak strength of 34.9% higher than the yielding strength, while TEC1 had the lowest peak strength of 17.8% higher than the yielding strength.

Based on these results, it could not be concluded whether the SEC bars resulted in a higher or lower peak strength than the BLK bars. Similarly, TEC bars did not necessarily seem to improve the peak strength compared with the BLK and SEC bars, with TEC5 bars even producing lower peak strengths in Batch 1 and Batch 2 than the BLK and SEC bars. Moreover, it could also be seen that the force level was different for each batch, with Batch 3 reaching the highest force level and Batch 1 having the lowest peak strengths. This observation illustrated the

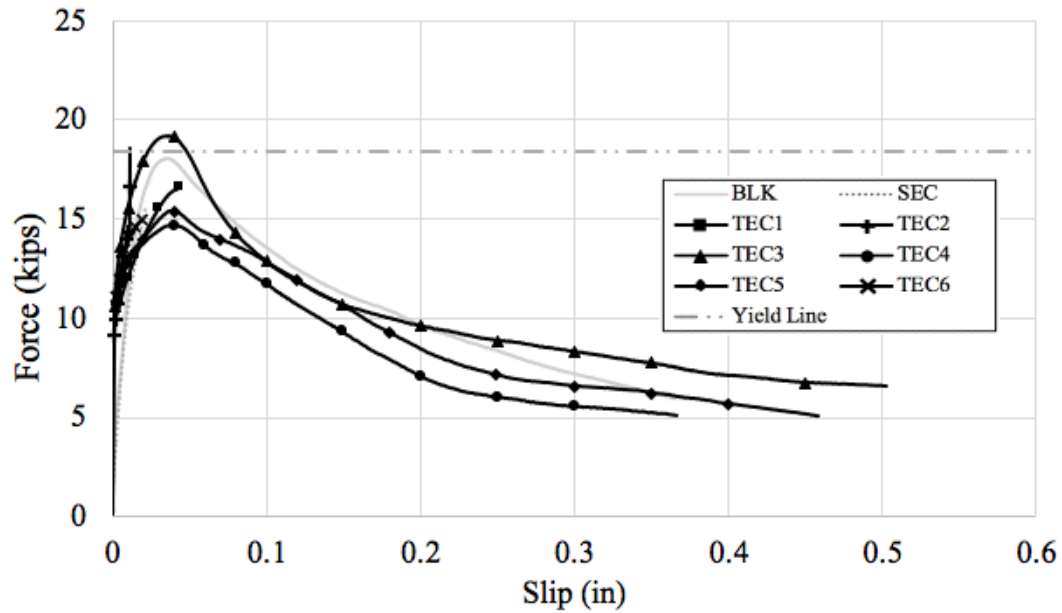
impact of the concrete compressive strength and confinement on the bond-slip behavior. Among all types of bars, TEC3 was the only bar type, which experienced steel yielding in all three batches, indicating a strong bond between the bar and the surrounding concrete.

4.2.2 Pullout Test Results: Initial slip resistance

Since the transverse cracks observed in bridge decks typically occur early at much lower stress values than the peak stress values recorded during the pull-out test, it is likely that what dominates the early development of these cracks is the initial slip resistance of the rebars, not their peak bond strength. Therefore, the initial slip resistance was of more importance in this study than the peak strength in evaluating the rebar bond-slip performance.

The overall bond-slip curves for the three batches are displayed in Fig 4.7 and the initial slip resistance curves for all three batches are displayed in Fig 4.8. A common feature observed in all three plots in Fig 4.8 was that the BLK and SEC bars manifested notably lower initial slip resistance than the TEC bars, which demonstrated that the applied roughness on the surface had a positive impact on increasing the initial slip resistance. Between the BLK and SEC specimens, the SEC specimen exhibited lower slip resistance as expected because of its smooth surface. From Fig 4.8 (c), it was clear that although the curve of TEC1 bar had a higher initial slope, its slip resistance degraded sharply and at a later stage, it showed even lower slip resistance than the BLK bars. The performance of the other TEC bars did not display any difference as significant among each other. However, they all showed much higher slip resistance than the TEC1, BLK, and SEC bars and their degradation of slip resistance occurred much later than that of the TEC1 bars. The surface voids on the TEC2-TEC6 bars (Fig 3.18) might have served as a “micro” anchorage system that helped with increasing the initial bond until the cementitious material

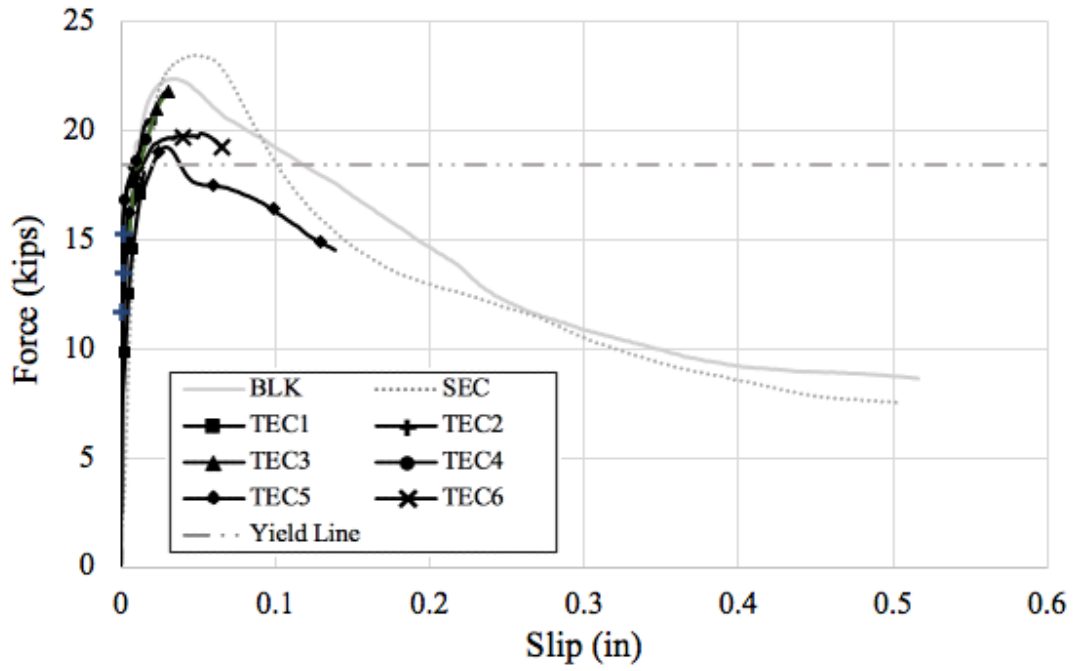
filling the voids was sheared off. To better quantify the performance of various bar types, the slip resistance was evaluated by calculating the initial tangent and secant slopes of the force-slip curves to obtain a more direct comparison.



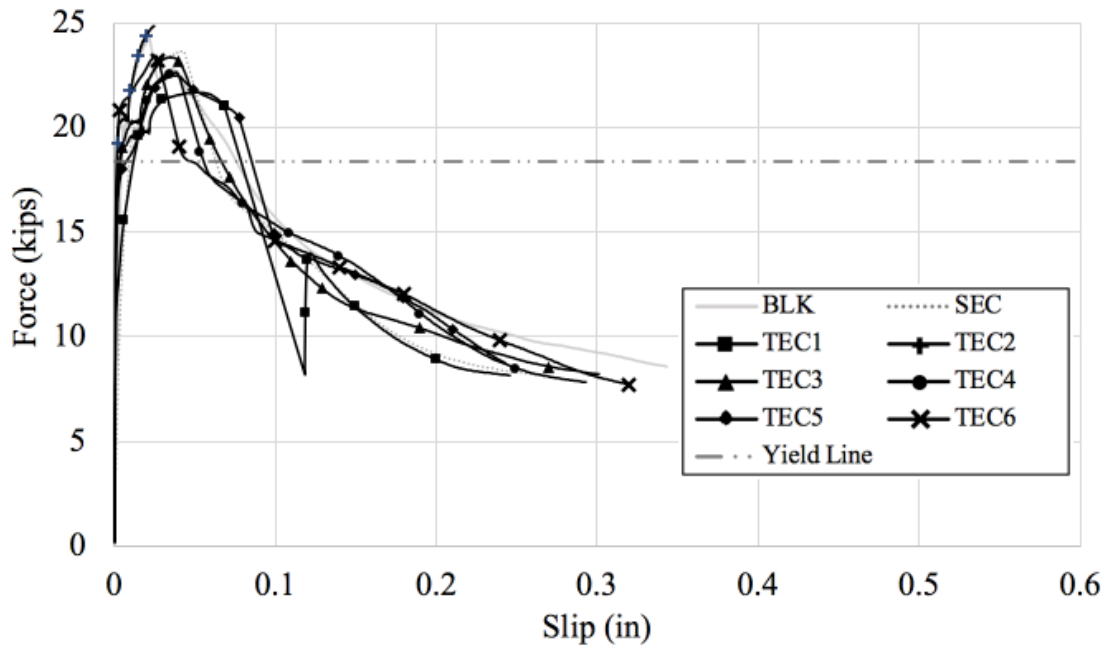
(a)

Fig 4.7: Overall force-slip curves for (a) Batch 1; (b) Batch 2; (c) Batch 3.

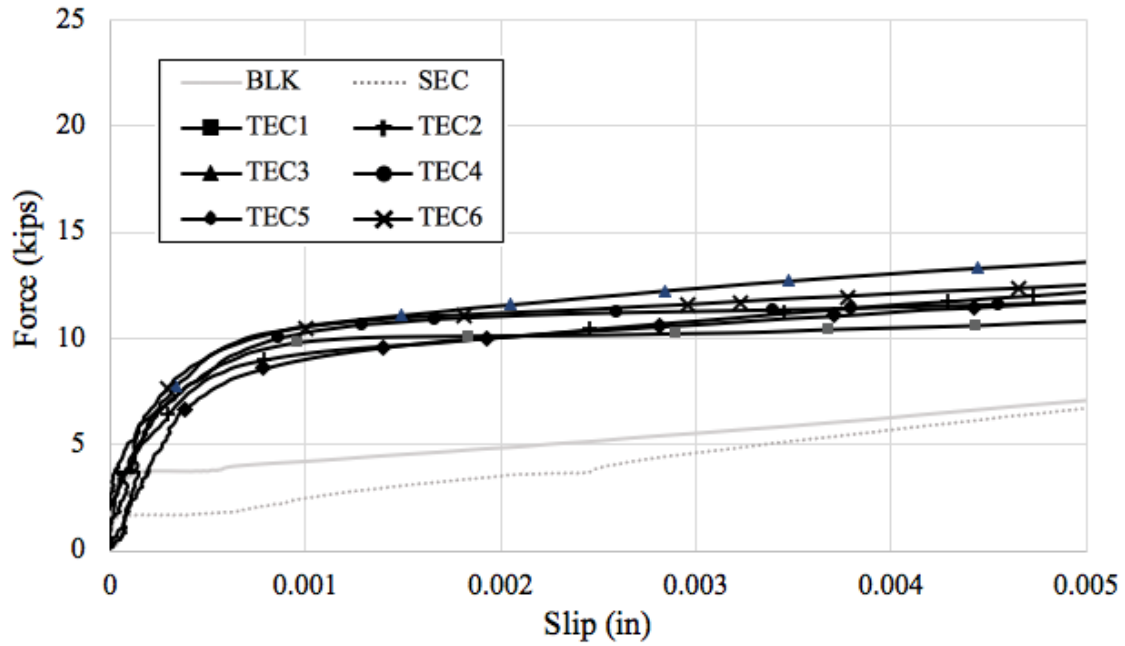
Fig 4.7 (cont.)



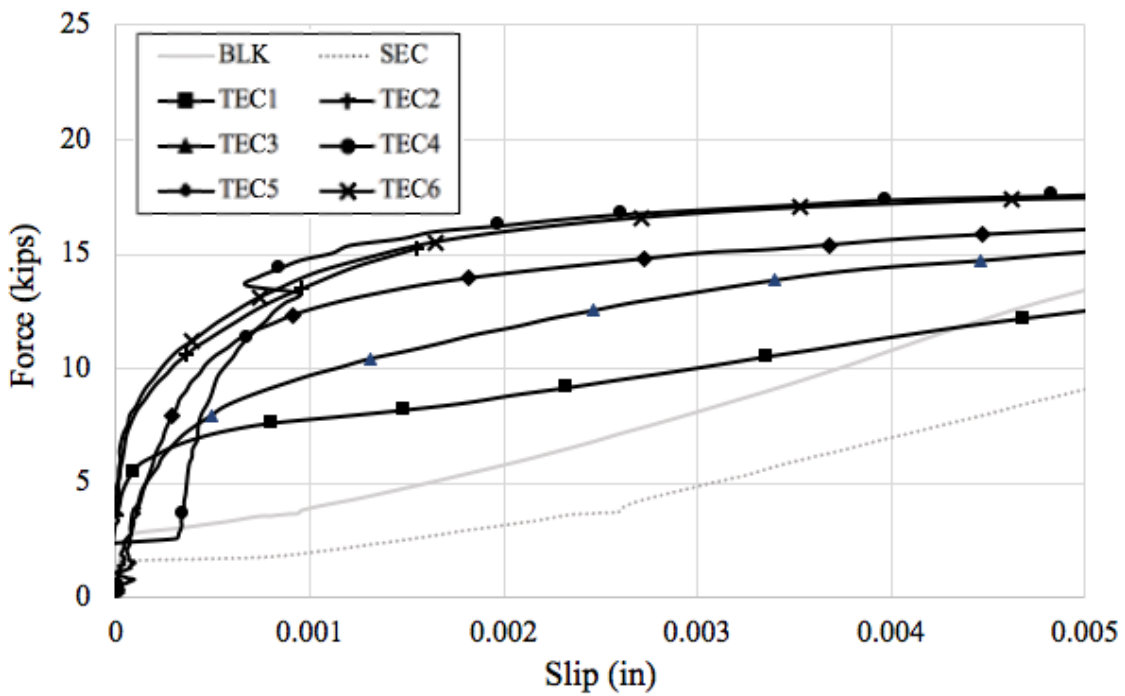
(b)



(c)



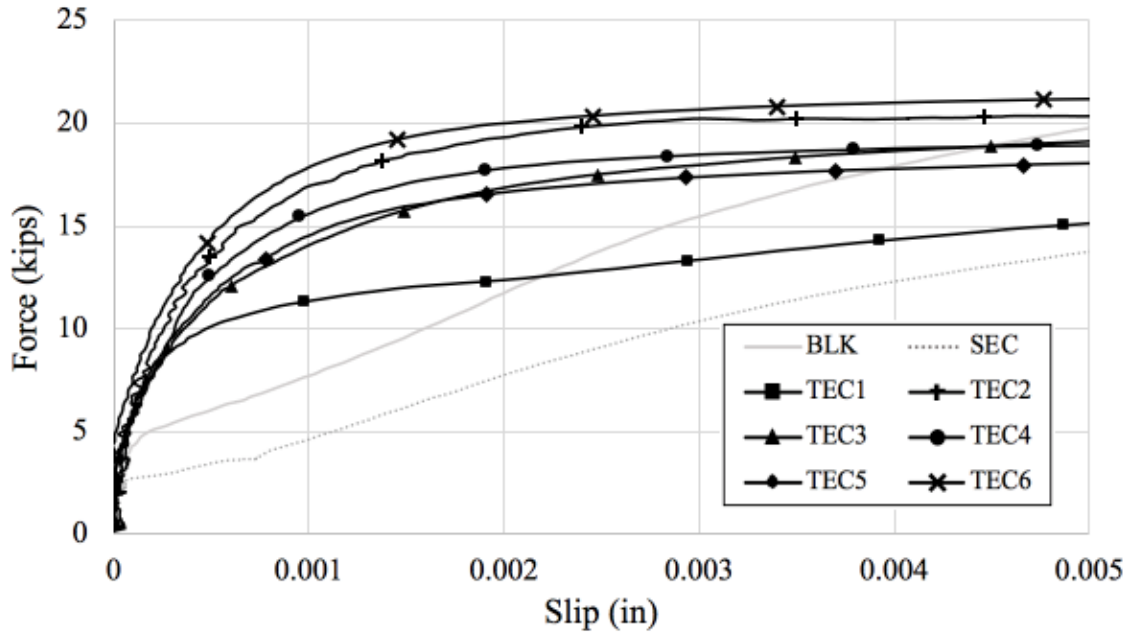
(a)



(b)

Figure 4.8: Initial slip resistance curves for (a) Batch 1; (b) Batch 2; (c) Batch 3.

Fig 4.8 (cont.)



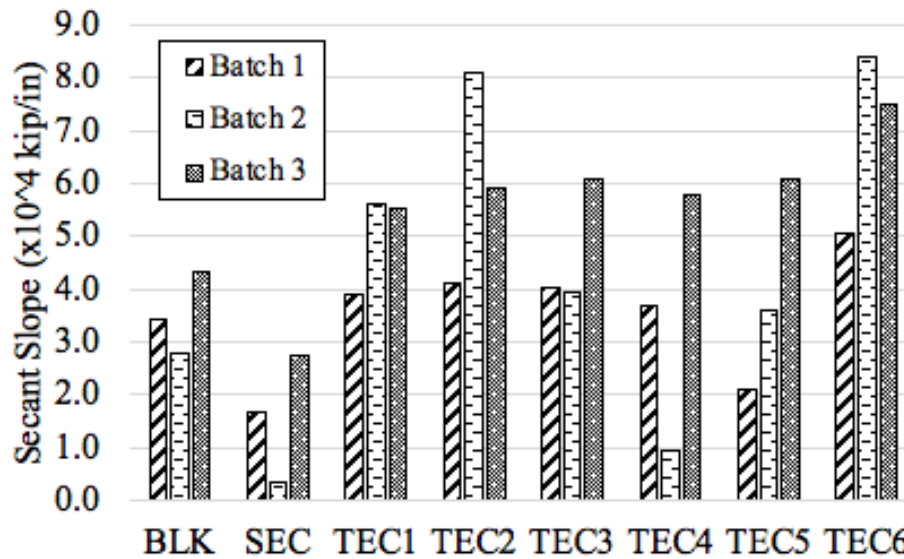
(c)

The initial tangent slope represented the slip resistance at a very low level of slip before any significant decrease in the slip resistance occurred. From a visual observation of the plots in Fig 4.8, for all batches, the slope sharply decreased at a slip less than 0.001 in. Therefore, the initial tangent slope was taken at a range of 0-0.0005 in. for all batches. The secant slope, on the other hand, represented an overall slip resistance better than the initial tangent slope. The range of data used to determine the secant slope was based on an investigation of bridge decks (DalSoglio, 2017), in which the crack spacing and crack width of multiple bridges were measured. For several bridges, the total crack width was measured in terms of microstrain. An average value of 473 microstrain based on all the measured crack widths was selected as the threshold of the secant slope calculation. Since the length of the bonded region in the pullout specimens was 3 inches, the upper bound of the range for the secant slope was determined to be 0.0014 in., i.e., the bonded region length multiplied by the strain value. The slip resistance

evaluated at this range was considered to be the closest to the actual bridge condition at cracking.

To look at the slip resistance farther from the range of the initial tangent slope, especially after the sharp decrease in the slope, the secant slopes at the range of 0.0028 in., were also evaluated.

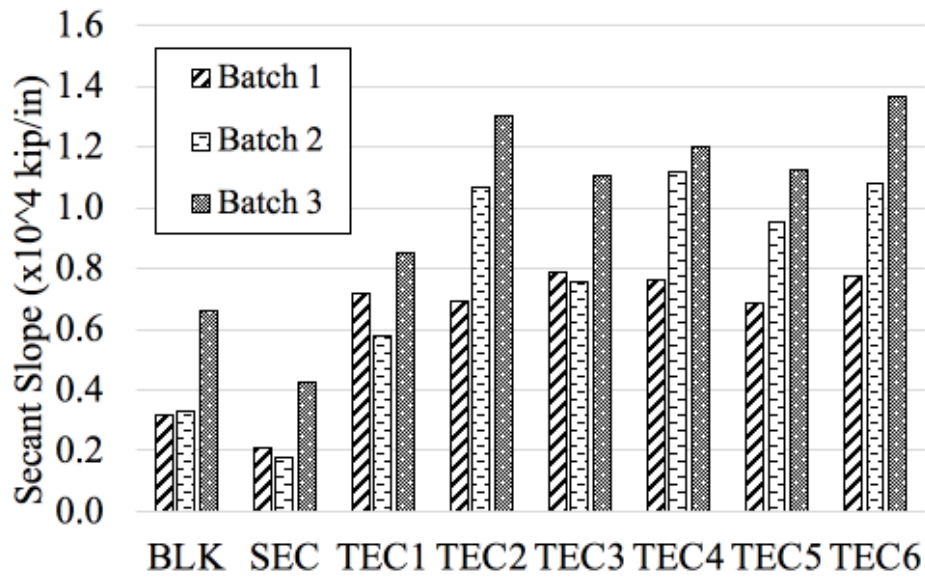
Fig 4.9 presents the initial tangent slopes and secant slopes for the three batches.



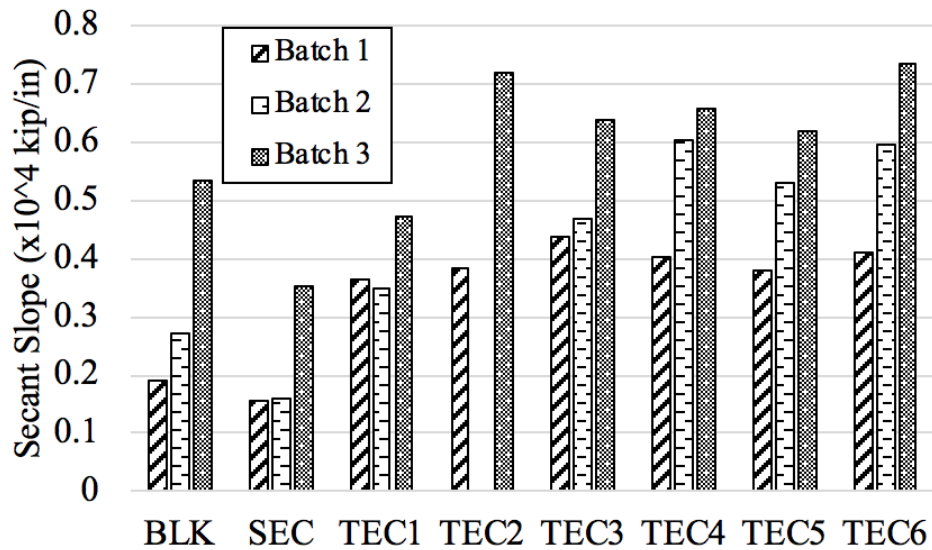
(a)

Fig 4.9: Comparison of: (a) Initial tangent slope; (b) Secant slope at 0.0014 in. slip; (c) Secant slope at 0.0028 in. slip for all three batches.

Fig 4.9 (cont.)



(b)



(c)

In Fig 4.9, the numerical values of the initial tangent slope and secant slope were different for each batch, with Batch 3 having the highest slip resistance due to the application of

CFRP confinement. Although the three batches had different concrete compressive strengths, the slip resistance of each bar relative to each other displayed a similar trend. In Fig 4.9c, the slip resistance of TEC2 was not included in the bar chart since TEC2 specimen split before reaching a slip of 0.0028 in. Furthermore, it could be observed that the slip resistance of the TEC bars was on average much higher than those of the BLK and SEC bars with the only exception of Batch 3 for the secant slope at 0.0028 in. In addition, the rapid degradation of the initial slip resistance of TEC1 observed from the force-slip curves in Batch 3 (Fig 4.8c) could further be corroborated by Fig 4.9. The average initial slip resistance of the TEC bars for the three batches was three times that of SEC bars and 50.3% more than that of BLK bars. At a low level of slip, the initial tangent slope and secant slope bar charts showed a similar distribution of slip resistance, with TEC2 and TEC6 having a higher slip resistance compared to the other TEC bars. The rest of the bars showed similar slip resistance distribution as the secant slopes taken at a lower level of slip. The overall observations based on the pull-out behaviors (peak strength and initial slip) and the roughness quantification suggested that TEC2, TEC3, and TEC6 exhibited superior bond-slip behaviors than the other types of bars. The numerical values of peak strength and initial slip resistance of all types of bars in Phase II study are shown in Appendix B.

Chapter 5: Finite Element Analysis of Interfacial Bond between TEC Bars and Concrete

The previously discussed results of roughness measurements and pull-out tests showed that the TEC bars exhibit great potential in improving the bond-slip behavior compared to SEC bars. Still, the bond mechanism at the interfaces of the reinforcement, epoxy coating, and surrounding concrete of TEC bars cannot be fully understood based solely on pull-out tests. To obtain a more in-depth insight into the bond mechanism, first, a numerical finite element (FE) simulation of the pull-out test was carried out using ABAQUS (Dassault Systèmes, 2014). The model captured the complex rebar geometry and the interfaces between concrete, epoxy, and steel using cohesive behaviors. Then the model was calibrated using the experimental test results of TEC6 bar in Batch 1, which was the one TEC bar type with the overall best bond-slip behavior. Next, a spring-based simpler approach was utilized to model the interfacial bond-slip behavior of TEC6 and SEC. Finally, using the parameters of cohesive behaviors developed in the first model for TEC6, a four-point-bending FE model of a TEC6- reinforced beam was created to evaluate the development length of TEC6 bars.

5.1 Cohesiveness-Based Model

5.1.1 Model Description

Most of the studies reported in the literature on the FE modelling of pull-out tests, focused on modeling only one interfacial plane, namely, the interface between the rebar and the surrounding concrete (Tang, 2015; Murcia-Delso et al, 2011; Issa & Masri, 2015; Pereira et al, 2015). However, for epoxy-coated bars, there are two interfaces to consider: 1) the interface

between concrete and epoxy coating, and 2) the interface between the coating and the steel rebar. Therefore, it was necessary to consider the effect of both interfaces in this study. In addition, the ribs on the rebar surface also play a significant role in the bond-slip mechanism by providing bearing force and mechanical interlocking. To capture different factors affecting the bond-slip interface, the complex geometry of bar ribs, epoxy coating, and the surrounding concrete next to the bonded region with the bar was all captured in the model, as can be seen in Fig 5.1. To reduce the meshing complexity and increase modelling efficiency, the ribs on the unbonded region were not modeled, and the ribs on the bar were modeled with sharp edges, instead of the more realistic smooth rounded edges. All the dimensions of the surrounding concrete and the rebar were the same as those of the pull-out test specimen. Both, the rebar and concrete were modeled with solid, homogenous C3D8R elements while the coating was modeled using C4R shell elements.

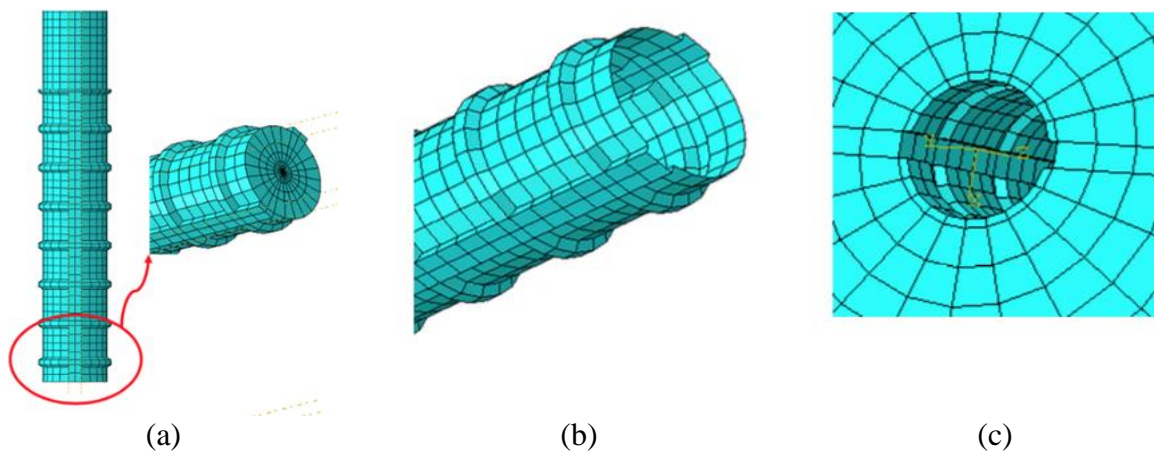
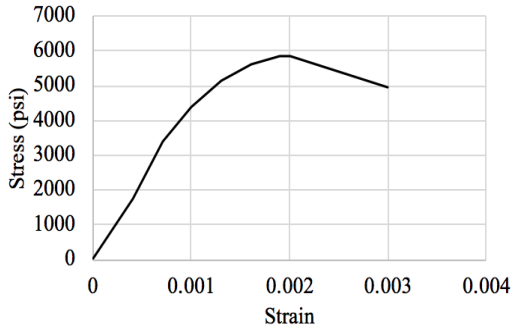
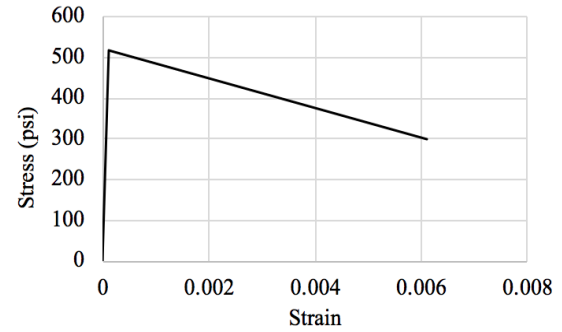


Fig 5.1: Geometry and meshing for (a) rebar; (b) coating; (c) surrounding concrete next to the bonded region.

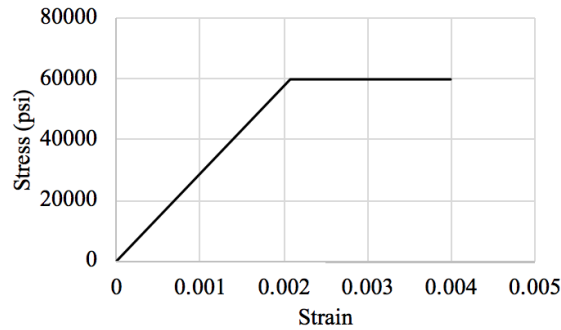
The ABAQUS concrete damaged plasticity model was adopted to simulate the nonlinear behavior of concrete due to its crushing in the region between the ribs (Dassault Systèmes 2014). The modified Hognestad model (Hognestad et al, 1955) was used to describe the compressive stress-strain behavior of concrete, and the splitting tensile strength defined by ACI 318 (2019) was used to define the concrete tensile behavior. An elastic-plastic model was used to model the steel rebar. The material constitutive curves used in the study are all shown in Fig 5.2. The slope of the post-peak descending branch for the concrete constitutive curve was decreased to achieve easier convergence of the model. The concrete plasticity parameters, including the dilation angle, eccentricity, f_{b0}/f_{c0} , K , and viscosity parameter were assigned as the default values of 31, 0.1, 1.16, 0.67, and 0, respectively (Dassault Systèmes 2014). The mechanical properties of the epoxy coating were selected based on typical values from the literature (Xiong et al, 2016), including an elastic modulus of 602 ksi, yielding stress of 1.74 ksi and Poisson's ratio of 0.31.



(a)



(b)



(c)

Fig 5.2: Constitutive behavior used for (a) Concrete in compression; (b) Concrete in tension; (c) Steel rebar.

To simulate the pull-out force, boundary conditions were placed on the top surface of the concrete to prevent any displacement in all directions without any rotational constraints. A displacement control of 0.0375 in. per minute, the same as the loading rate of the actual pull-out test, was imposed on the top surface of the bar.

5.1.2 Interfacial Properties

Two interfaces were incorporated in this model: 1) interface between the steel substrate and epoxy coating, and 2) interface between the epoxy coating and the surrounding concrete. The bond-slip behaviors at the two interfaces were different. From the experimental pull-out tests, it was observed that some coating residues were adhered to the concrete exposing several regions of the bar surface, which illustrated that the bond between the coating and concrete was stronger. Based on this observation, a stronger bonding strength between the concrete and the epoxy coating was assumed for the finite element model. Fig 5.3 shows the meshing interfaces between bar ribs, coating, and the surrounding concrete. Since coating was modelled with shell elements, it was not visible in the figure.

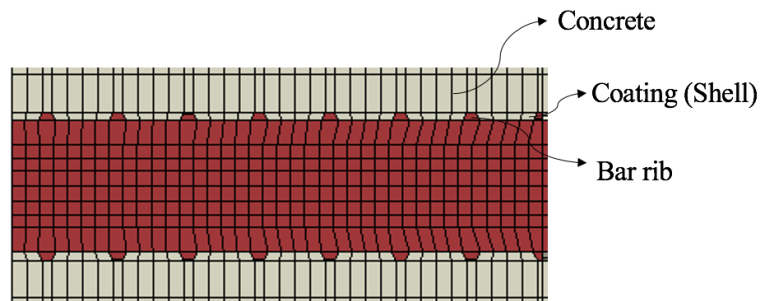


Fig 5.3: Meshing interfaces between bar ribs, coating, and the surrounding concrete.

Cohesive behavior was specified at the coating-concrete and coating-steel interfaces to simulate the bond between interfaces. The traction-separation response in ABAQUS (Dassault Systèmes 2014) was used to define the bond strength and debonding failure at pull-out, as shown in Fig 5.4. The cohesive behavior could be defined in normal, shear, and tangential directions, with the stiffness along each direction being K_{nn} , K_{ss} and K_{tt} , respectively. Damage initiation

marked the beginning of the degradation of the cohesive response and damage evolution described the rate at which the material stiffness degraded after the point of damage initiation was reached. Since for the pull-out test, the bond-slip behavior in the shear direction was of the primary concern, the cohesive and damage parameters for all three directions were defined to be identical.

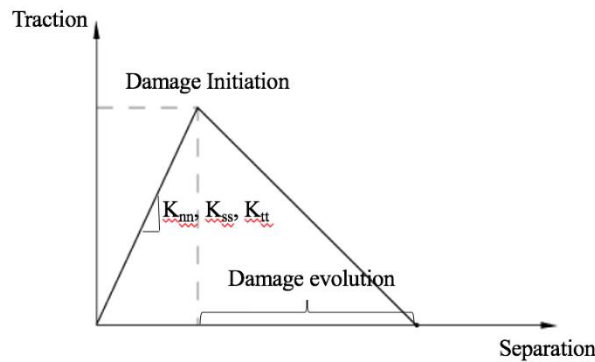


Fig 5.4: Traction-separation response in ABAQUS (Dassault Systèmes 2014).

Given the traction-separation response discussed above, since it was assumed that the bond strength at the coating-concrete interface was stronger than that at the coating-steel interface, K_{nn} , K_{ss} and K_{tt} at the coating-concrete interface were defined to be three times that of the coating-steel interface. The maximum stresses and damage evolution of the coating-concrete interface were set to be larger than those of the coating-steel interface to indicate slower cohesion degradation. Once the stress at any node reached the peak point, i.e., maximum stress, degradation started and the damage evolution determined the degradation rate. These parameters were calibrated using previously discussed experimental results. Table 5.1 displays the parameters for the cohesive behavior and the damage of the two interfaces.

Table 5.1: Cohesive behavior and damage parameters for the two interfaces.

Interface	Cohesive Behavior			Damage			
	K_{nn} (psi/in.)	K_{ss} (psi/in.)	K_{tt} (psi/in.)	Normal (psi)	Shear 1 (psi)	Shear 2 (psi)	Evolution (in.)
Coating-Concrete	3×10^8	3×10^8	3×10^8	5000	5000	5000	0.006
Coating-Steel	1×10^8	1×10^8	1×10^8	1250	1250	1250	0.005

5.1.3 Comparison between Experimental and Numerical Results

Since bridge decks transverse cracks often happen at an early stage, the initial ascending slip resistance was of the greatest concern. Fig 5.5 displays a comparison between the experimental and numerically simulated bond-slip behavior of TEC6 bar in Batch 1. At a low level of slip when the slip was less than 4.72×10^{-3} in., the simulated force-slip curve closely matched the experimental result, although at a higher slip stage, the simulated result started to deviate and diverge.

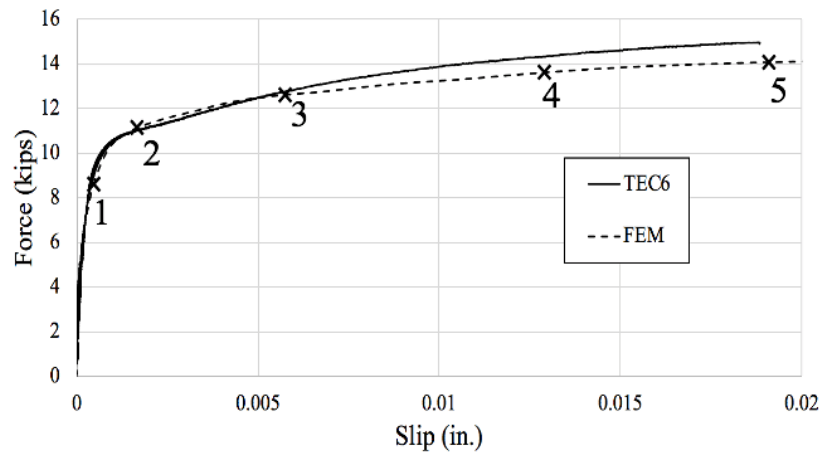


Fig 5.5: Experimental and simulated bond-slip curves of TEC6 bar in Batch 1.

The contour plots in Fig 5.6 show the stresses at the bonded region of concrete and steel at a slip of 0.019 in., which was close to the slip right before the splitting failure in the

experimental data. The shear stress was concentrated at the ribs of the rebar and the lower part of the concrete key between ribs. This distribution seemed reasonable because as the bar was being pulled out from the concrete, it was moving upwards against the surrounding concrete. This slip was primarily resisted by the bearing force on the ribs. Likewise, the axial stress in the rebar decreased towards the bottom end. On the surrounding concrete, the axial stress was concentrated at the upper part of the bonded region close to the interface of bar and concrete and started to decrease downwards. However, it was still concentrated primarily around the bar ribs.

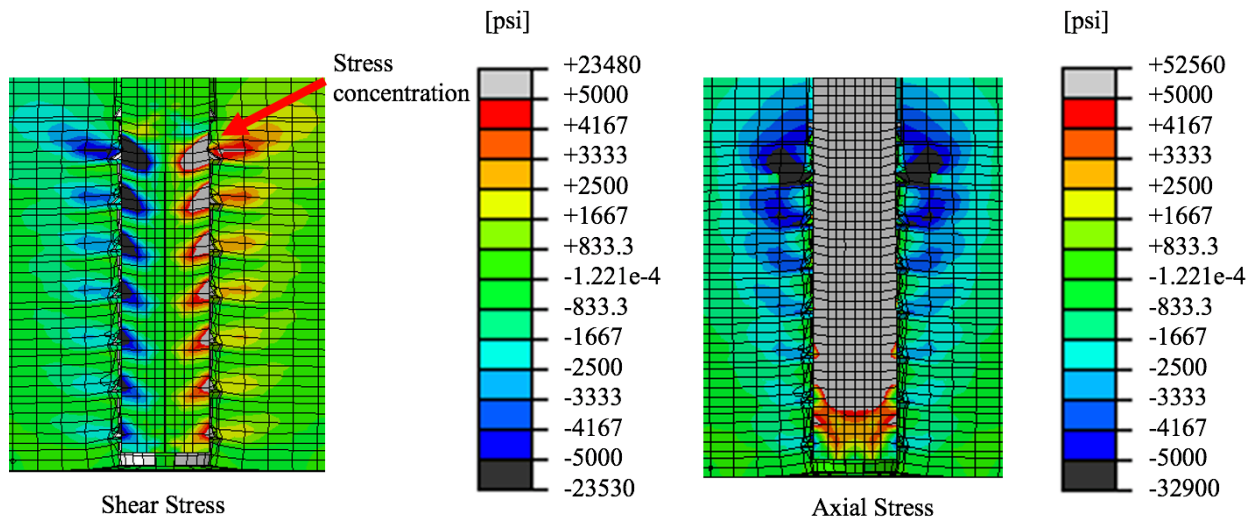


Fig 5.6: Deformed contour plots for shear stress and axial stress on steel and concrete at the bonded region.

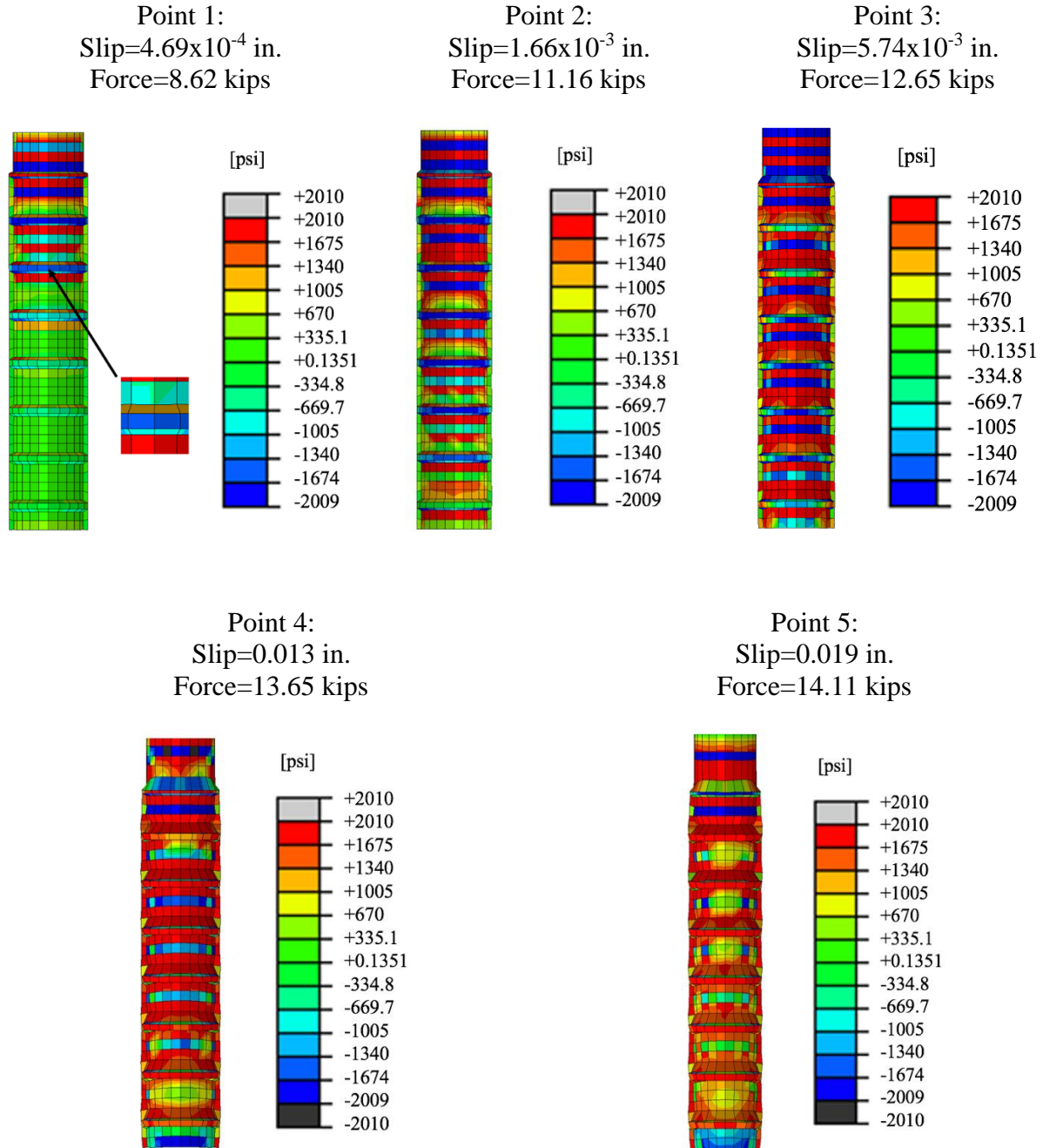


Fig 5.7: Deformed contour plots for longitudinal stress on coating at the bonded region at different slip levels.

Apart from the stress on rebar and concrete, it was also necessary to observe how the longitudinal stress in coating propagated at different slip levels. Due to the applied surface

roughness, unlike SEC bars, whose coating did not experience a high level of stress, the coating of TEC bars was subjected to high friction with concrete, resulting in a higher level of stress in coating. In Fig 5.7, the contour plots show the longitudinal stress at the bonded region of the coating at five different slip levels, labeled on the force-slip plot in Fig 5.5. At Point 1, the upper portion of the bonded region was subjected to significantly higher stress than the lower portion at this early stage when some coating elements already reached yielding. As the slip increased, the longitudinal stress on the coating started to propagate downwards and an increasing amount of the coating reached yielding, indicating damage on the coating. The stress was primarily concentrated on and around the ribs. The top face of the ribs was first subjected to compressive stress at the early stage, but as the bar was gradually pulled out, the stress on the ribs became tensile. This change could be illustrated by the longitudinal stress on the element marked out by the arrow in Fig 5.7 as -1.62 ksi, -0.67 ksi, and 1.89 ksi at Points 1, 3, and 5, respectively. Moreover, the horizontal splitting stress in the concrete initiated at the region close to the bonded region and propagated outwards. At Point 5, which was close to the point right before the specimen split in the experimental data, it could be clearly seen from the figure that there was stress concentrated on the ribs and significantly less stress on the region between ribs. At this same point, the splitting stress at the edge of the concrete specimen reached concrete tensile capacity, indicating splitting of the specimen, which matched the observation. Based on the observations above, it could be concluded that the finite element model was able to capture the bond-slip behavior of steel, epoxy coating, and the surrounding concrete, hence could be used for future numerical simulations of TEC bars embedded in concrete.

5.2 FE modelling using Spring Connectors for TEC6 and SEC Pull-Out Specimens

Although the finite element model with cohesive behavior captured the bond-slip mechanism accurately and matched the experimental result of TEC6 specimen well, it was expensive computationally due to the complicated geometry. To shorten the computation time, the model geometry was simplified, and spring connectors were used to simulate the interface properties instead of cohesive behavior. Both TEC6 and SEC specimens in Batch 1 were modelled using this method. The interaction properties were calibrated using the experimental results.

5.2.1 Model Description

Instead of the 3-D solid C3D8R elements in the previous model, the rebar was modelled with 3-D truss T3D2 elements. In this case, the complicated rebar geometry and the two interfaces due to the epoxy coating were not represented in this simplified model. The concrete however was still modelled with homogenous, solid C3D8R elements. In the bonded region with the bar, the nodes of concrete coincided with the nodes on the bar. To make the model accurate enough without taking too much computation time, 15 nodes were assigned on the bonded region. The material constitutive curves of concrete and steel were the same as described in Fig 5.2. The same boundary conditions and loading rate were applied.

5.2.2 Interfacial Properties

In this model, the bond-slip behaviors were incorporated using spring elements in ABAQUS (Dassault Systèmes, 2014) to allow the reinforcing bar to move relative to the concrete. In reality, there are force and displacements in the normal and tangent directions.

However, the force and relative displacement along the longitudinal direction parallel to the bar were of primary concern. It is also the direction of the force and displacements recorded in the pull-out test. Hence, axial spring connectors were defined between nodes of concrete and bar at the bonded region. The axial connection provided connection between the two nodes where the relative displacement only took place along the line separating the two nodes. Since the top surface of the concrete was laterally constrained, and only a longitudinal, axial tensile force was applied on the bar, the force and displacement only occurred along the longitudinal direction. A schematic diagram of axial spring connectors at the bonded region and the relative motion at one typical node are shown in Fig 5.8. Initially, before any force was applied, the nodes of concrete and rebar coincided with each other. At coincident nodes, the defined local orientations of the first node in connectivity was used. As the tensile force was being applied, the bar started to move along the direction of the force and relative displacements between the rebar and concrete nodes started to occur. When the nodes started to separate, the defined local orientations were ignored and the direction of the line between the two nodes was used. In ABAQUS (Dassault Systèmes, 2014), the force-displacement relationship for an axial spring connection is defined as shown in Equations 5.1 and 5.2. For this model, the rebar nodes were defined as node a and the concrete nodes were defined as node b, therefore, the direction of the relative motion is opposite to the direction of the force.

$$f_{axial} = f_1 q \quad (5.1)$$

$$q = \frac{x_b - x_a}{||x_b - x_a||} \quad (5.2)$$

where f_{axial} is the axial spring force, f_1 is the stiffness, and x_b, x_a are the locations of nodes a and b.

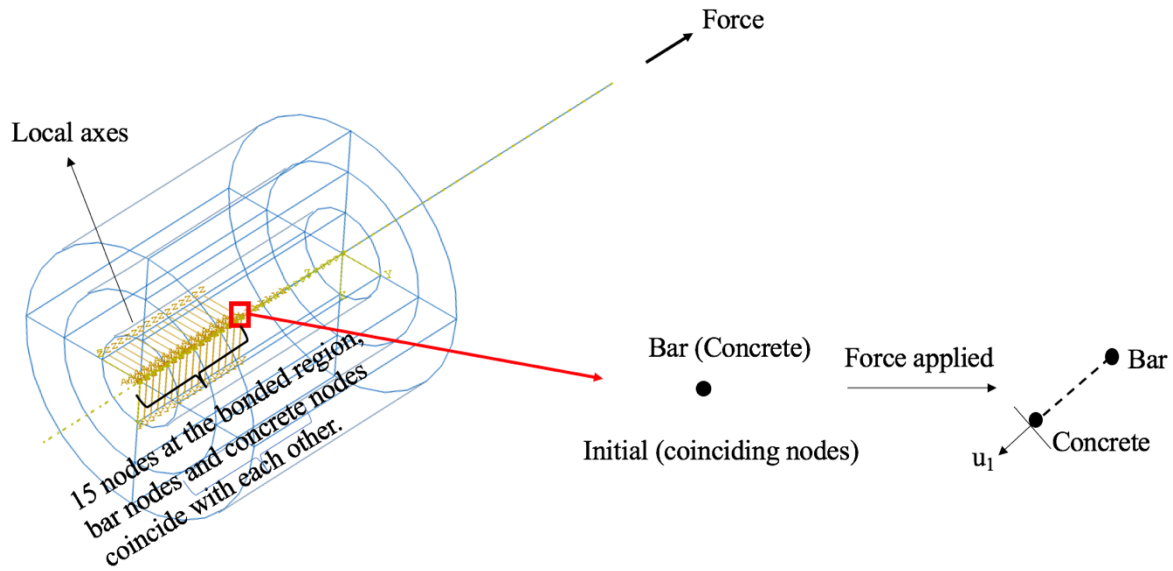


Fig 5.8: Schematic diagram of the axial spring connectors at the bonded region and the relative motion defined at one of the nodes.

To capture the bond-slip behavior accurately, tabular data was used to define the axial spring connector's nonlinear behaviors in the elastic region. The spring connectors lost their stiffness when outside the specified range of the tabular data, which indicated that the force was extrapolated as constant with the change of relative motion. Fig 5.9 shows the definition of the nonlinear connector behaviors defined in ABAQUS User's Guide (2014). Typical points in the nonlinear elastic region of the force-displacement curve shall be specified, such as the initial force when there is no displacement, the ascending or descending branch, and the force in the plastic region, etc. In the example shown in Fig 5.9, the curve was defined with five points: (u_1, F_1) , $(0, F(0))$, (u_2, F_2) , (u_3, F_3) , (u_4, F_4) , with F_1 and F_4 defining the force at the plastic region in the compressive and tensile directions, respectively.

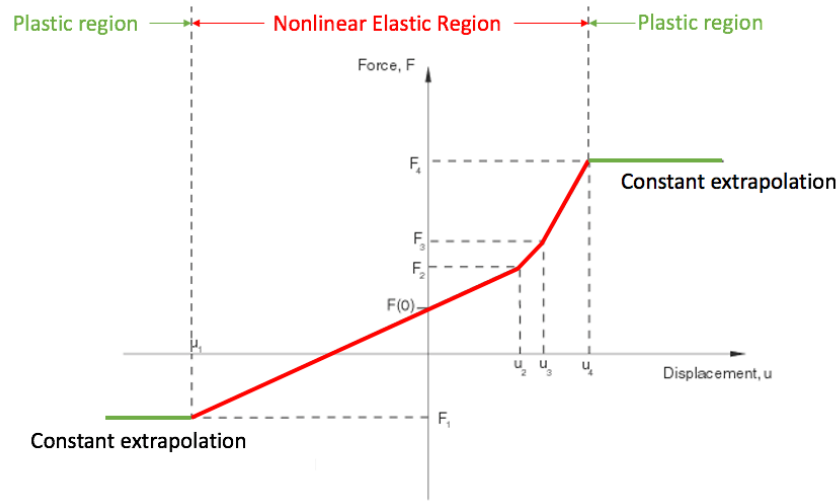


Fig 5.9: Definition of nonlinear spring connector behaviors in ABAQUS (Dassault Systèmes, 2014).

The nonlinear spring connector behavior was calibrated based on the experimental results. Table 5.2 displays the tabular data input for the nonlinear spring connector behaviors of the TEC6 and SEC models, where F indicates the spring force and U denotes the relative motion between the two nodes. Fig 5.10 shows the graphical representation of the spring connector behaviors. As the initial slip resistance of TEC6 specimen was much higher than that of the SEC specimen, the stiffness of the TEC6 spring connectors in the elastic region was set to be much higher than that of the SEC as well. The force at the constant region was approximately proportional to the peak force obtained from the experimental results. In this case, the peak force of the SEC specimen was slightly lower than that of the TEC6 specimen.

Table 5.2: Tabular data input for the spring connector behaviors of TEC6 and SEC models.

SEC		TEC6	
F (lb)	U (in)	F (lb)	U (in)
-1000	-0.023	-990	0.013
-500	-0.01	-935.625	-0.011
-300	-0.005	-650	-0.005
-200	-0.0025	-500	-0.0001
-150	-0.00125	0	0
0	0	950	0.0002
1000	0.008	-	-

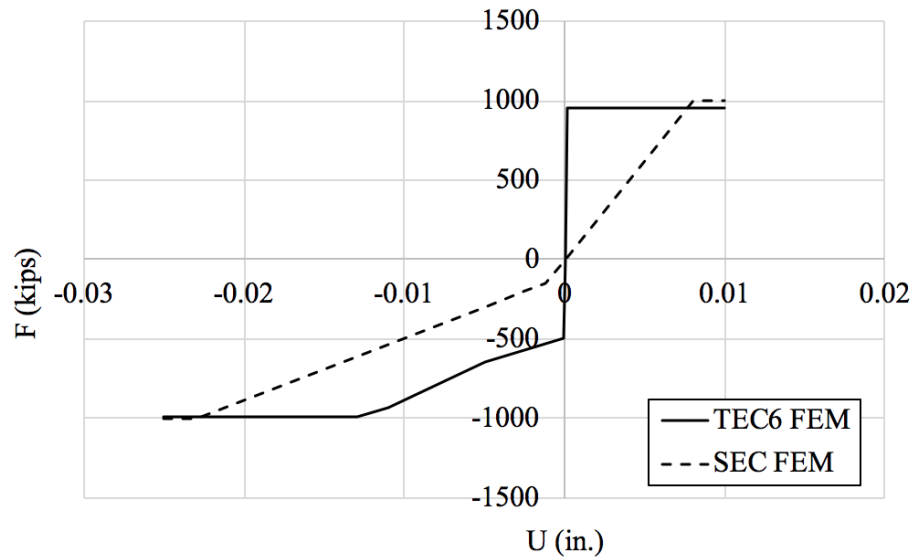


Fig 5.10: Graphical representation of nonlinear spring connector behaviors for TEC6 and SEC models.

5.2.3 Discussion of Results

Using the interaction properties specified in the last section, the FE analysis results matched well with the experimental results for both TEC6 and SEC specimens, as shown in Fig 5.11. Although the FE simulated results of the SEC specimen missed the small spike at the beginning of the force-slip curve, the rest of the simulated curve was a very close match with the experimental results. Therefore, the simplified FE model could be considered as an effective phenomenological approach to capture the bond-slip mechanism accurately. The computation time of the simplified model was also significantly shorter than that of the previous model with cohesive behaviors.

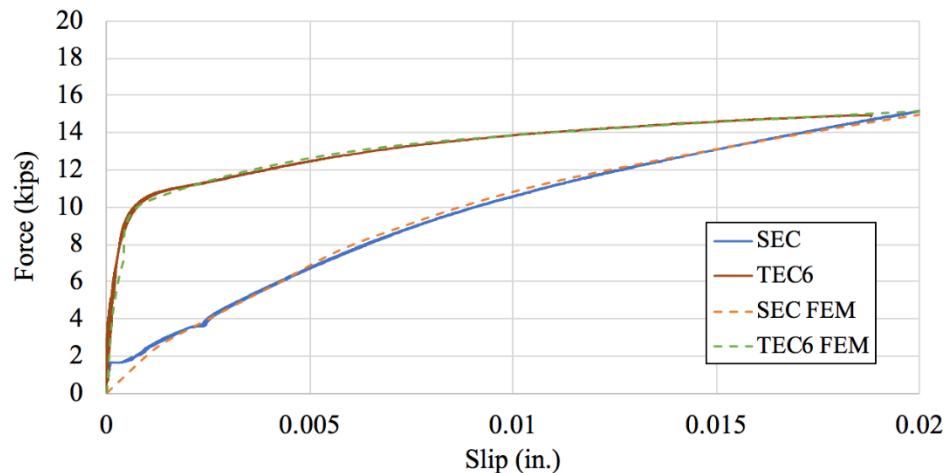


Fig 5.11: Comparison between the experimental results and simulated results for TEC6 and SEC specimens.

Apart from the comparison between the FE simulated and experimental results, the stress contour plots obtained from the simplified model were also examined. Four points were selected to represent different stages of the bond-slip curve, as can be seen in Fig 5.12. As the time increments for the SEC and TEC6 models were not exactly the same, the four points were selected so that the slips of each point on TEC6 and SEC models were as close as possible. Fig

5.13 and Fig 5.14 display the contour plots for shear stress and longitudinal tensile stress at the bonded region corresponding to four points on the force-slip curves for TEC6 and SEC specimens, respectively. From Fig 5.13 and Fig 5.14, both the shear stress and longitudinal tensile stress were concentrated at the bonded region. The magnitude of the shear stress at the bonded region of the SEC specimen was much smaller than that of the TEC6 specimen at points 1, 2 and 3, indicating that the initial slip resistance of the SEC specimen was much smaller than that of the TEC6 specimen. The shear stress distribution in the TEC6 specimen at the four points also showed that shear stress developed from the top of the bonded region. However, at point 4, which was right before splitting, the shear stress distribution for both SEC and TEC6 specimens were roughly the same. The same trend was also manifested in Fig 5.14 (a) and Fig 5.14 (b).

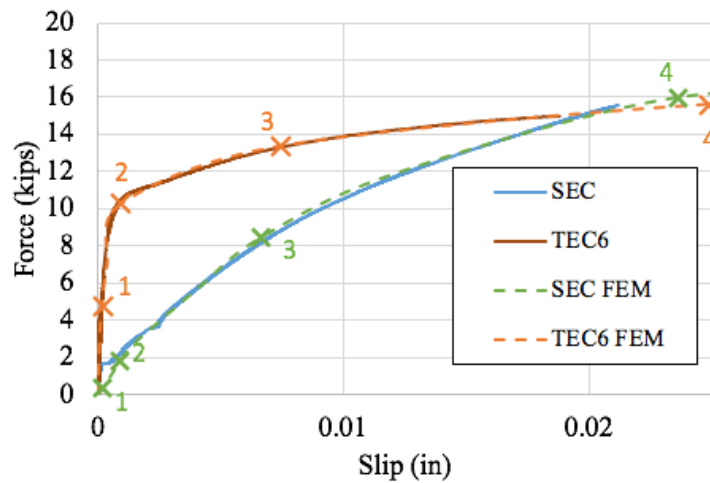
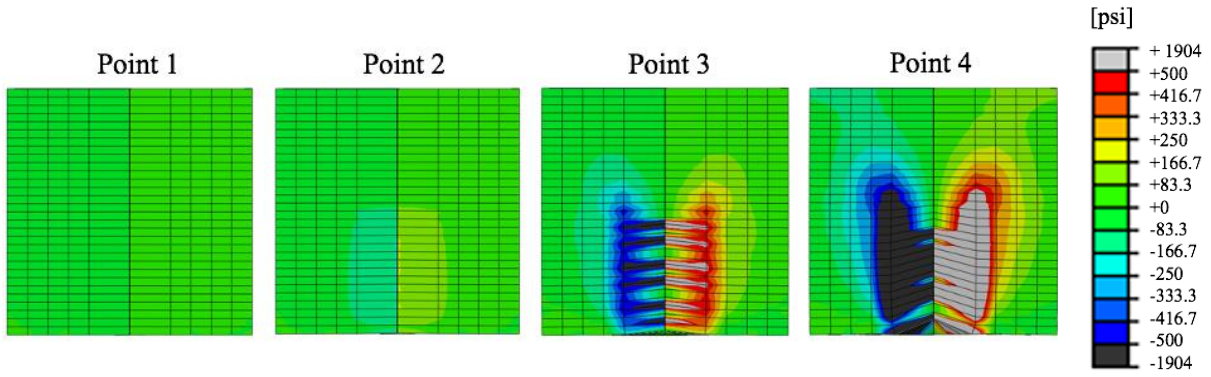
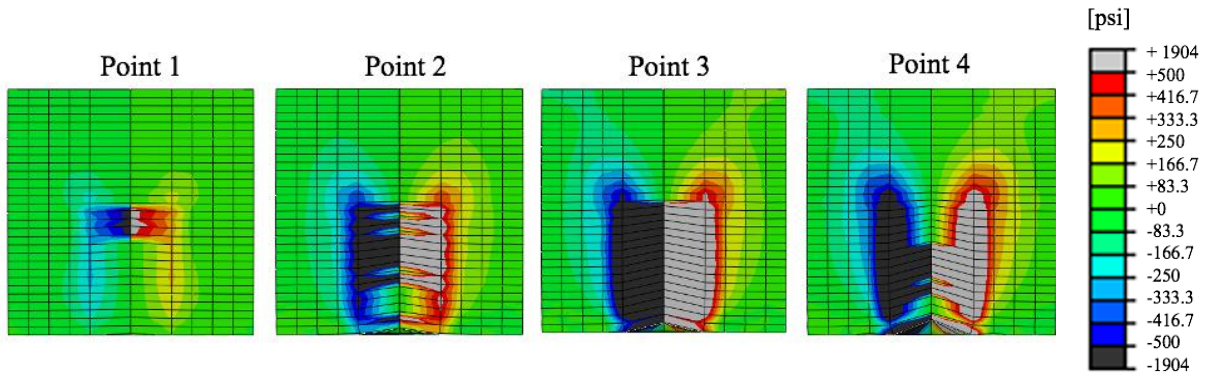


Fig 5.12: The four points on the force-slip curves of the SEC and TEC6 specimens where the contour plots were examined.

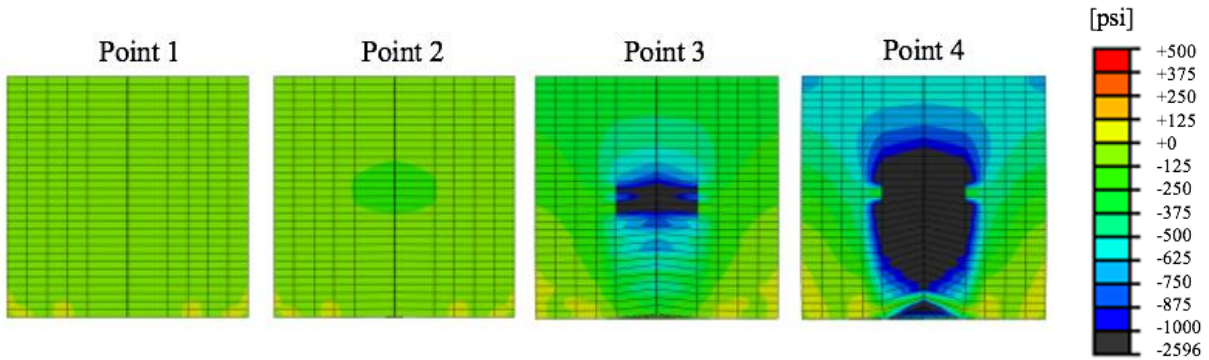


(a)



(b)

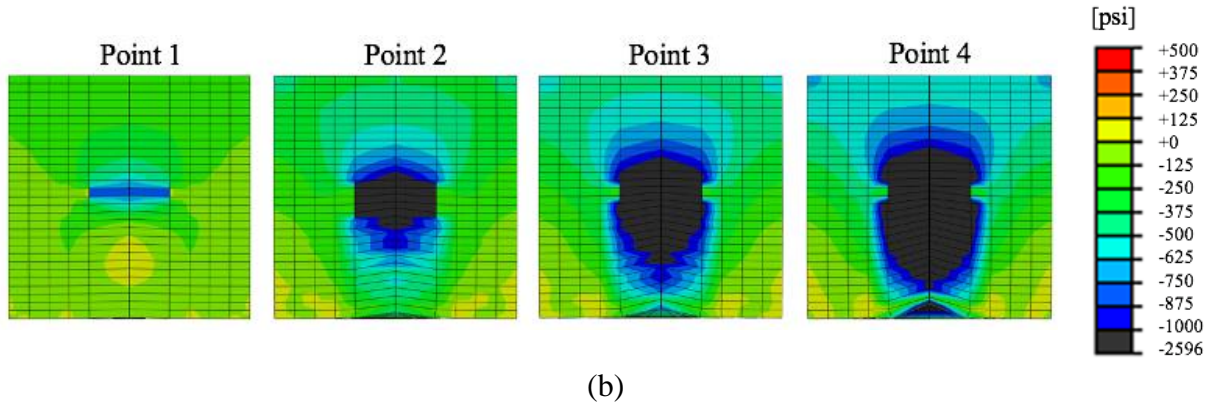
Fig 5.13: Shear stress contour plots for (a) SEC specimen and (b) TEC6 specimen.



(a)

Fig 5.14: Longitudinal tensile stress contour plots for (a) SEC specimen and (b) TEC6 specimen.

Fig 5.14 (cont.)



The advantage of the simplified model with spring connectors was that it showed stress development at the bonded region and produced a good match with the experimental results with a significantly shorter computation time. Although the simulated results from the previous modelling method with cohesive behaviors matched the experimental results well, the simulated results started to deviate a little after it reached the peak strength. However, since the rebar ribs were eliminated in the simplified model, the model provided no insights on the concentration of stress around the ribs. Neither could any stress concentration on the coating be observed and interpreted in the simplified model due to the lack of coating. Therefore, the first modelling method with detailed geometry and cohesive behavior gave more comprehensive and detailed insights on the bond-slip mechanism while the simplified model saved more computation time and generated a better match phenomenologically.

5.3 Analysis of Development length of TEC6 Rebar

One of the reasons for introducing TEC bars is to eliminate the increase of development length and potentially reduce the bridge deck cracking caused by the use of smooth epoxy-coated rebars. Therefore, it was important to evaluate the development length of TEC reinforcing bars in

bridge decks. For this purpose, a finite element model of a concrete member reinforced with a No.5 TEC6 bar under four-point bending was analyzed in ABAQUS using the interaction properties discussed in Section 5.1.

5.3.1 Model Description

A finite element model of a beam representing a typical portion of an actual bridge deck under four-point bending was created. The definition of the development length was the length needed for the reinforcing bar to develop its yield strength. In this study, the method of determining the development length of TEC6 bar was to adjust the location of the point loading along the beam length until the bar reached the yielding stage. To reduce the computation time and avoid convergence issues, only a quarter of the beam and its supports were modelled with symmetrical boundary conditions, shown in Fig 5.15. The beam was cut in half along both X and Z axes with point loading applied by a roller on top. The end of the beam was placed on a bearing support. Apart from achieving symmetry, the four-point bending also created a constant moment region at the middle portion of the beam without effects from the shear force.

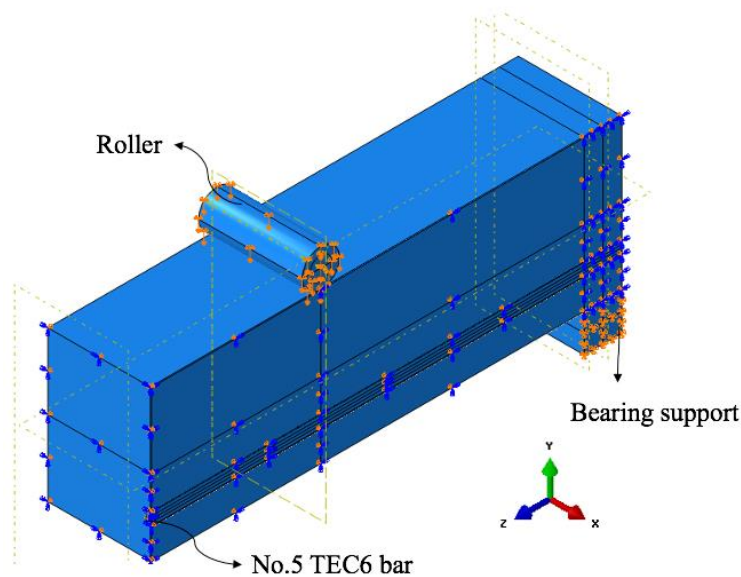


Fig 5.15: Finite element model of a beam under four-point bending.

The dimensions of the beam model, shown in Fig 5.16, were determined based on typical bridge deck dimensions and detailing in Illinois to achieve the best simulation of the real-life condition. The height of the beam was 8", which was equal to the bridge slab thickness. The width of the beam represented the typical spacing of the bottom tensile reinforcements. In bridges, both the lateral and longitudinal reinforcements resist loads along different load paths. The finite element model created in this study used the longitudinal bottom bar spacing, 11", as the width of the beam. The length of the beam measured from the centers of the bearing supports was 48". Since the finite element model represented only one-quarter of the actual beam, the height, width, and length of the beam in Fig 5.16 were only half of those specified values. The bottom cover of the beam was identical to that of the actual bridge considering the transverse reinforcements underneath. The geometry of the TEC6 bar was the same as what was used in the finite element model discussed in Section 5.1.

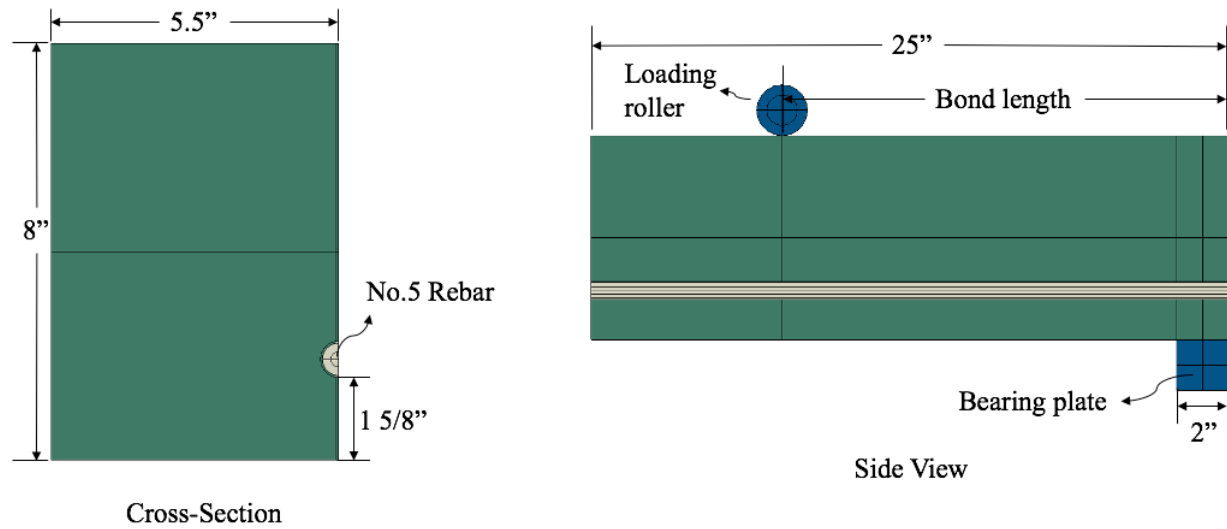


Fig 5.16: Geometry of the beam model.

The material properties of the bar and concrete were the same as what was shown in Fig 5.2. Likewise, the parameters of cohesive behavior and damage determined from the finite element model of the pull-out specimen discussed in Section 5.1 were assigned for the interaction between concrete and bar since it was the best representation of the actual bond-slip relationship for TEC6 bar.

5.3.2 Discussion of Results

The bond length, which was the distance from the beam end to the nearest point of loading, was adjusted by changing the location of the loading point until the reinforcing bar reached yielding. At first, the loading point was placed at 1.5 inches from the beam center (near the far end of the beam from the bearing support for the finite element model), then the loading point was moved away from the center at increments of 1.5 inches. After a total of 5 iterations, it

was found that the development length of TEC6 bar was between 17.5 inches and 19 inches. For each iteration, the yield moment, M_y , was calculated by multiplying the point load at bar yielding by the distance from the center of the bearing support to the point load. Table 5.3 displays the yield moment, point load at bar yielding and the corresponding bond length for each iteration.

Table 5.3: Yield moment, point load at bar yielding, and the corresponding bond length for each iteration.

Iteration	Bond length (in)	M_y (kip-in)	Bar yielded?
1	23.5	320.04	Yes
2	22	323.04	Yes
3	20.5	332.24	Yes
4	19	344.84	Yes
5	17.5	N/A	No

After numerical result of the development length was obtained, it was compared with the analytical results calculated based on the specifications in AASHTO (2017) shown in Equation 5.3-5.6 and ACI318-19 (2019) shown in Equation 5.7.

$$l_d = l_{db} \times \left(\frac{\lambda_{rl} \times \lambda_{cf} \times \lambda_{rc} \times \lambda_{er}}{\lambda} \right) \quad (5.3)$$

$$l_{db} = 2.4d_b \frac{f_y}{\sqrt{f'_c}} \quad (5.4)$$

$$\lambda_{rc} = \frac{d_b}{c_b + k_{tr}} \quad (0.4 \leq \lambda_{rc} \leq 1.0) \quad (5.5)$$

$$k_{tr} = 40A_{tr}/sn \quad (5.6)$$

where l_{db} is the basic development length, λ_{rl} is the reinforcement location factor, λ_{cf} is the coating factor, λ_{rc} is the reinforcement confinement factor, λ_{er} is the excess reinforcement factor calculated as the ratio of the required reinforcement amount and the provided reinforcement

amount, λ is the concrete density modification factor, f_y is the rebar yielding strength, f'_c is the concrete compressive strength, and d_b is the rebar diameter (AASHTO, 2017), c_b is the smaller of the distance from center of bar being developed to the nearest concrete surface and one-half of the center-to center spacing of bars being developed, k_{tr} is the transverse reinforcement index, A_{tr} is the total cross-sectional area of all transverse reinforcement within a spacing s crossing the potential plane of splitting through the reinforcement being developed, n is the number of bars developed along plane of splitting. For the epoxy coated bars with cover less than $3d_b$ or with clear spacing between the bars less than $6d_b$, λ_{cf} shall be taken as 1.5. For epoxy bars not covered as discussed above, λ_{cf} shall be taken as 1.2. (AASHTO, 2017). In this study, since the bottom cover was less than $3d_b$, the λ_{cf} of 1.5 was applied.

$$l_d = \frac{f_y \psi_t \psi_e \psi_g}{25 \lambda \sqrt{f'_c}} \quad (5.7)$$

where f_y is the rebar yielding strength, ψ_t is the casting position factor, ψ_e is the rebar coating factor, ψ_g is the rebar grade factor, λ is the concrete weight factor, and f'_c is the concrete compressive strength. The criteria of selecting ψ_e is the same as the one used in AASHTO (2017). In this case, ψ_e was still selected as 1.5 since the clear cover was less than $3d_b$.

The analytical development lengths based on ACI 318-19 (2019) and AASHTO (2017) was calculated for a No.5 Grade 60 BLK and TEC bars embedded in normal weight concrete. The analytical values of the SEC and BLK bars were then compared with the numeral value of the TEC6 bar. The values of the numerical development lengths for TEC6 bar and the analytical development lengths for the SEC and BLK bars are listed in Table 5.4. The numerical value obtained from finite element analysis was slightly smaller than the analytical value for the BLK bar based on ACI318-19 (2019) but was greater than the value of the BLK bar development

value calculated from AASHTO (2017) by around 22.5%. However, compared with the development length calculated for the SEC bar, TEC6 bars could save about 38% of the bar calculated from ACI 318-19 (2019) and 18% of the bar calculated from AASHTO (2017), which confirmed the potential of TEC6 bar to decrease the amount of the development length needed. Overall, the finite element analysis still proved that TEC6 bar had potential in decreasing the development length needed compared with the SEC bars.

Table 5.4: Numerical and analytical values of development length of TEC6 bars.

Specification	AASHTO (2017)		ACI 318-19 (2019)		Numerical
Bar Type	BLK	SEC	BLK	SEC	TEC6
Development length, l_d (in.)	14.9	22.3	19.6	29.4	17.5-19

Apart from the development length, some other model characteristics were also examined and compared among different bond lengths to see the behavior of TEC6-reinforced concrete beam under flexural loading. Fig 5.17 displays the concrete crack patterns at yielding for four different bond lengths. Fig 5.17a shows that the cracks originated from the bottom of the beam under the point load. As the loading points were located farther from the beam center, more cracks appeared in the constant moment region between the loads with roughly uniform spacing. The beam in all four cases failed in flexure. In the lower left corner of each contour plot in Fig 5.17, a small vertical crack was observed, which was due to the tensile force at the edge of the bearing support.

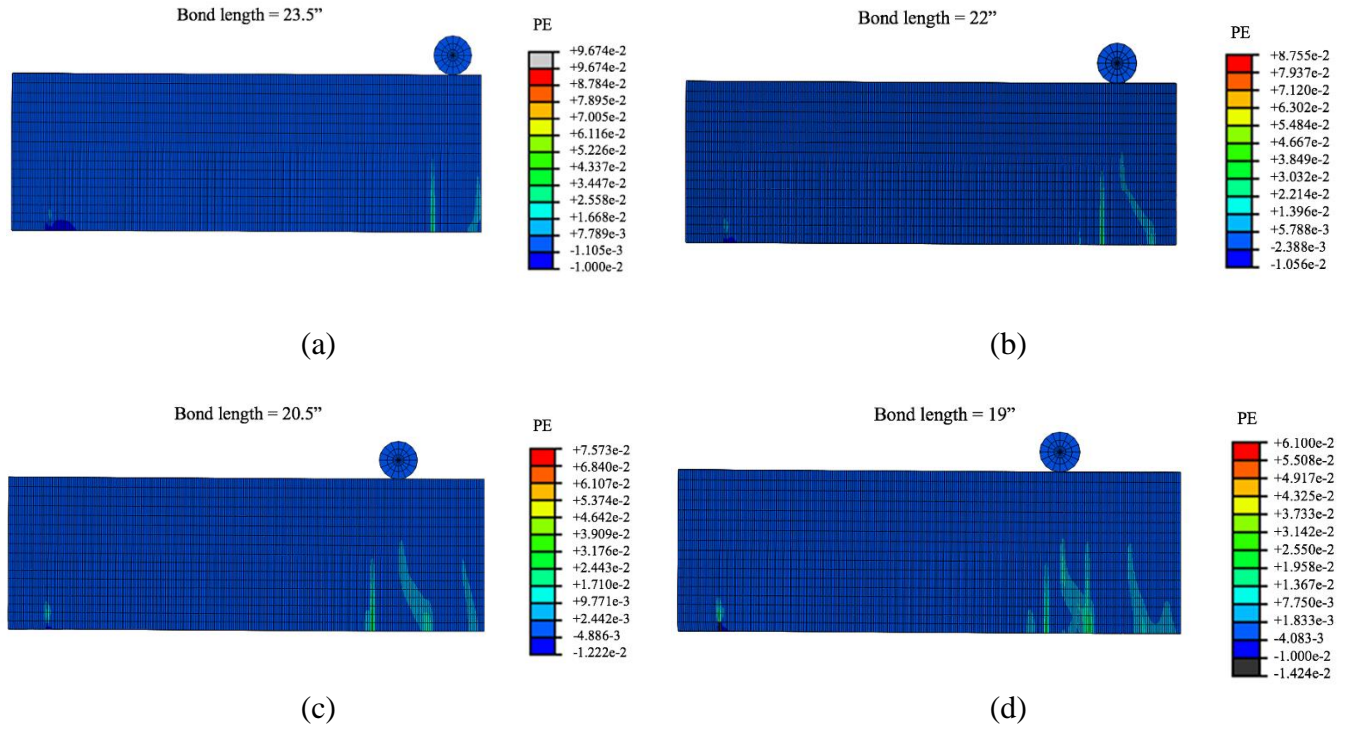


Fig 5.17: Crack pattern for a bond length of (a) 23.5"; (b) 22"; (c) 20.5"; (d) 19".

In addition, the shear stresses and longitudinal stresses at the central plane of the beam for the four different bond lengths were also examined and compared, as shown in Fig 5.18 and Fig 5.19. In Fig 5.18, a bottle-shaped compression strut, which was narrow at the ends and wide at the midsection, could be observed in all four cases connecting the point load and the bearing support. As the point load was moved further away from the center, the strut travelled with the point load and the compressive stress increased in magnitude. From Fig 5.19, it could be observed that the TEC6 reinforcing bar started yielding at the constant moment region at the center of the beam. As the point loading moved away from the center, the yielded region of the rebar travelled along with the point load. In conclusion, the finite element model illustrated that the TEC6 had great potential in effectively decreasing the required development length. After the stresses and crack patterns on the beam model were examined for all four cases of bond lengths,

their distribution was as expected. Therefore, the results obtained from the finite element model were deemed valid.

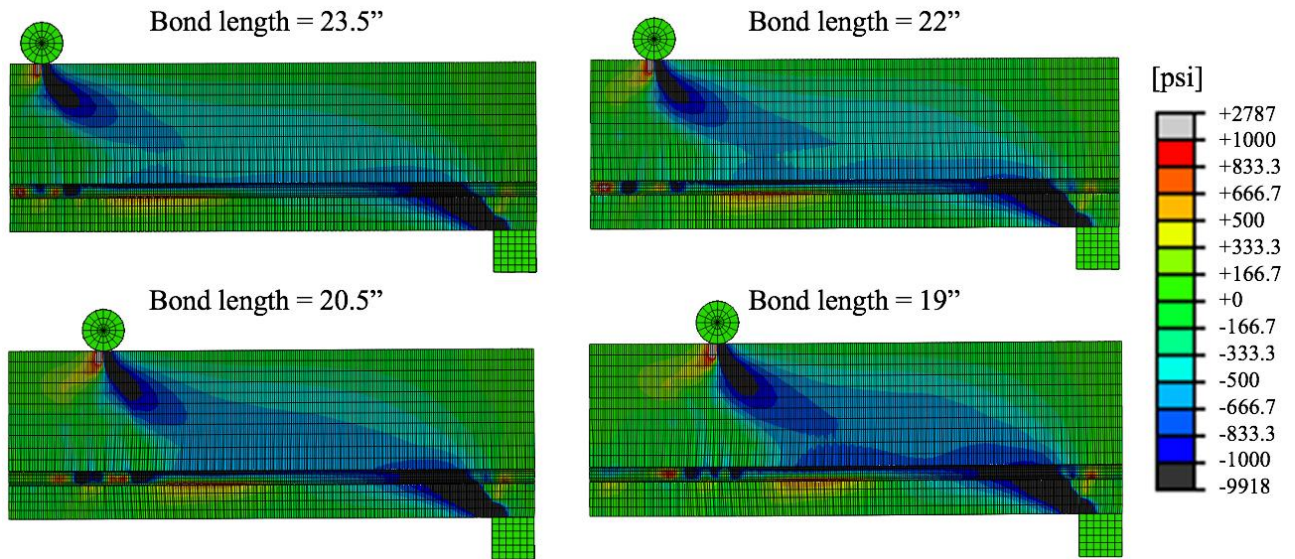


Fig 5.18: Shear stress distribution at the center plane of the beam for the four cases of bond lengths.

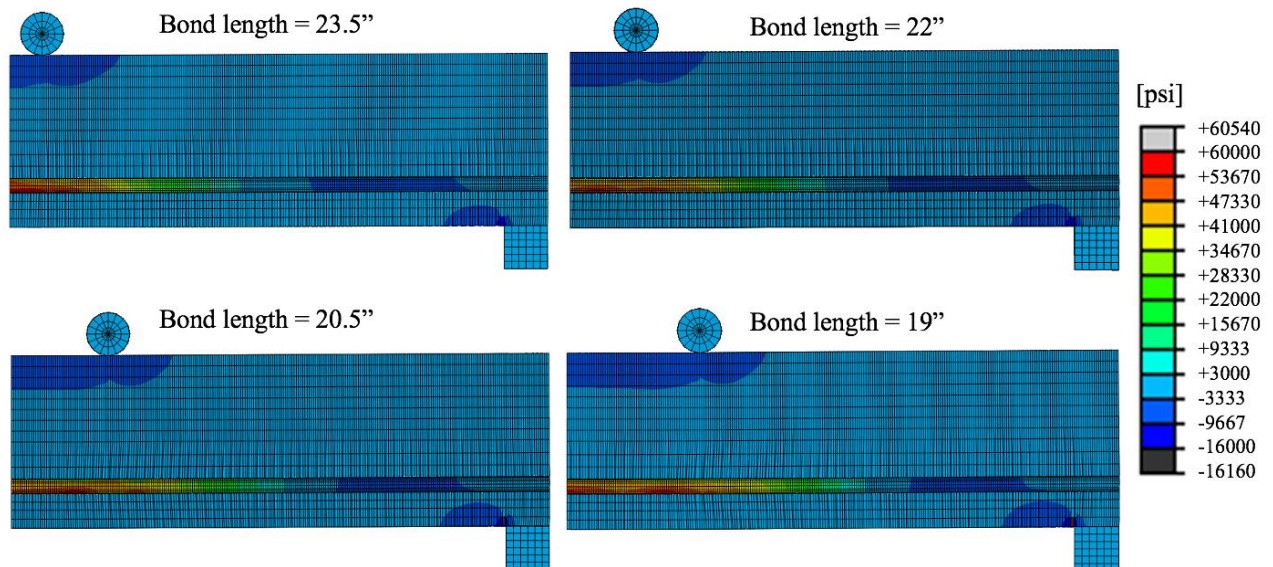


Fig 5.19: Longitudinal stress distribution at the center plane of the beam for the four cases of bond lengths.

Chapter 6: Shrinkage Test Design of Bridge Deck Reinforced with TEC Bars

After a series of small-scale experimental and numerical studies, the next phase of this study was to move up to large-scale laboratory tests. Based on the findings of the surface roughness quantification and the pull-out tests on BLK, SEC, and TEC bars, a new type of TEC bars, labelled TEC7, was manufactured with surface roughness close to that of TEC6 bar, which manifested the best overall bond-slip behavior. Plans are set to test two large-scale bridge deck specimens reinforced with SEC and TEC7 bars to explore the difference in their shrinkage and cracking behaviors. This chapter only discusses the design phase of the large-scale laboratory specimens and the planned experimental tests that will be performed in the future.

6.1 Test Plan

The objective of the large-scale bridge deck test was to monitor and compare the impact of two types of epoxy coated reinforcing bars, namely textured and non-textured bars, on the concrete shrinkage of two identical large-scale composite concrete bridge deck specimens. The tested specimens were in the form of eight-inch-thick concrete deck sitting on top of a steel I-shaped girder with two ends of the deck restrained. The two specimens were identical except in the type of reinforcing bars where SEC bars were used in one specimen while TEC7 bars were used in the other specimen. After the deck was casted, the shrinkage of the two specimens will be monitored using strain gages and digital image correlation (DIC).

During the shrinkage monitoring period, after the concrete develops sufficient strength, i.e. at 28 days, the specimens will be subjected to thermal loading. Both steel girders will be heated at both web sides to around 110 °F to simulate the effect of ambient temperature during summer. The goal of the thermal loading test is to examine the tendency of the bridge deck

reinforced with SEC and TEC7 bars to cracking due to temperature difference between concrete deck and steel girder. The heating of the specimens will be achieved through using a propane tank connected to long, stainless linear burners. The entire heating process should take only about a few hours. Overall, this large-scale laboratory test aims to highlight any difference in concrete deck shrinkage caused by the different reinforcing bars to provide insights on the shrinkage condition of actual bridge decks reinforced with SEC and TEC7 bars.

6.2 TEC7 Reinforcing Bar Surface Characteristics

From the pull-out test results discussed in Chapter 4, it was concluded that TEC2 and TEC6 exhibited the highest slip resistance among all the TEC bars, and TEC3 was the only type of bar which yielded in all three batches. Therefore, TEC2, TEC3, and TEC6 were recommended as they showed a higher potential in improving the bond-slip behaviors. Based on these results, since TEC2 and TEC3 were provided by one manufacturer and TEC6 was provided by another manufacturer, TEC7 bar was made by the first manufacturer with consultation from the second manufacturer to combine the advantages of the roughness application procedure from both manufacturers. Fig 6.1 shows images of the TEC7 and SEC bars used for the bridge deck test. The TEC7 and SEC bars used for this test were both Grade 60 No.5 bars.

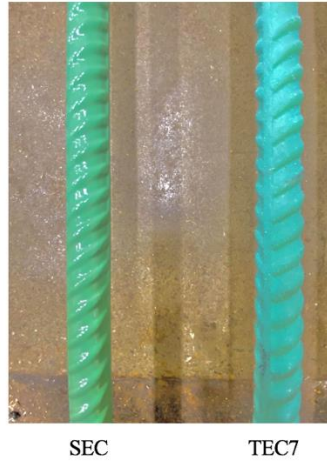


Fig 6.1: TEC7 and SEC bars used for the bridge deck shrinkage test.

Using the same surface roughness quantification procedure described in Chapter 3, the surface roughness of TEC7 bar was quantified and compared with that of the other TEC bars. Fig 6.2 shows the comparison of R_a , R_z , S_a and S_z values for TEC7 and the rest of the TEC bars. The 1-D parameters R_a and R_z showed that the roughness of TEC7 bar is the highest of all TEC bars. However, the 3-D parameters S_a and S_z indicated that the roughness of TEC7 was comparable to TEC6, but was still higher than the rest of the TEC bars.

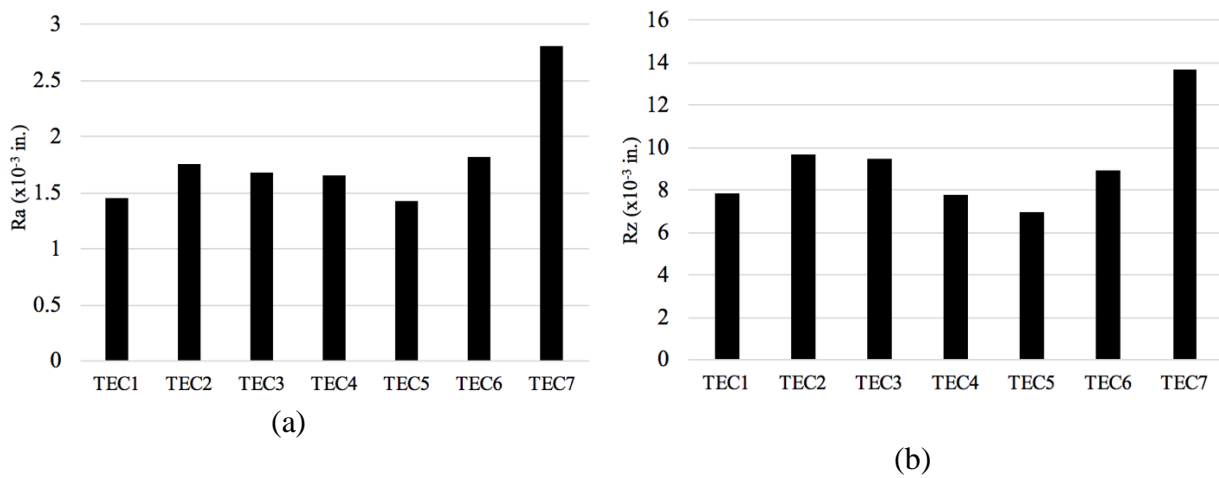
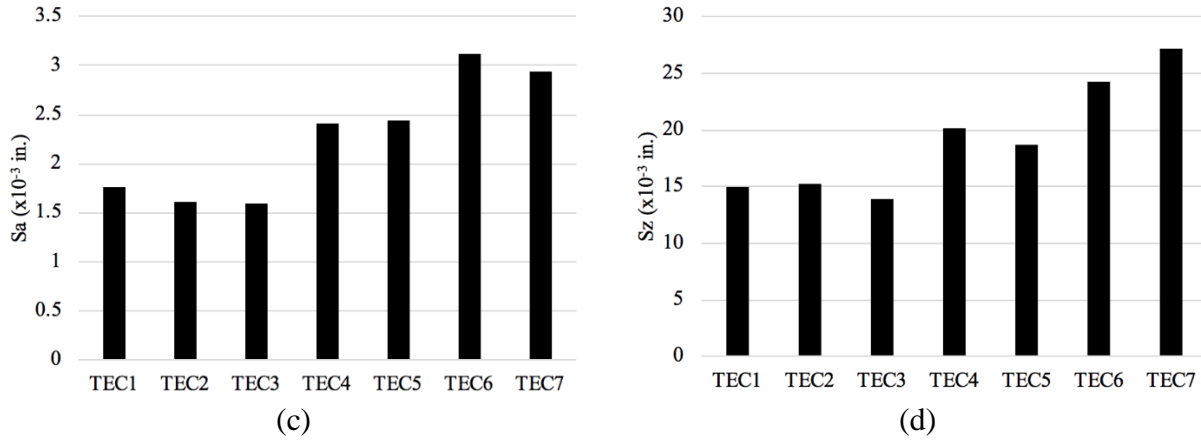


Fig 6.2: Comparison of (a) R_a ; (b) R_z ; (c) S_a and (d) S_z values for TEC7 and the rest of TEC bars.

Fig 6.2 (cont.)



6.3 Specimen Design

6.3.1 Specimen Description

The specimens used in this study were designed to represent the positive moment region of composite typical bridge decks in Illinois (see Fig 6.3). As shown in the figure, the specimens comprise a steel girder supporting an 8-in.-thick concrete deck. Each deck was reinforced longitudinally with No.5 TEC7 and SEC bars at the top and bottom. The concrete deck was constrained to the girder with shear studs. To allow easier propagation of cracks for more obvious observation, the shear studs at the middle region of the girder were removed. At both ends of the specimen, L8"x8"x1/2" steel angles were used to constrain the movements of the deck. The rebars extended through the angle at each end to keep its continuity and to prevent rebars from sliding at each end, the rebars were fastened with lock collars to the steel angles. Fig 6.4 presents a zoom-in view of the lock collars fastening the rebars. Both specimens were simply supported on the lab floor, with one bearing support and one roller support.

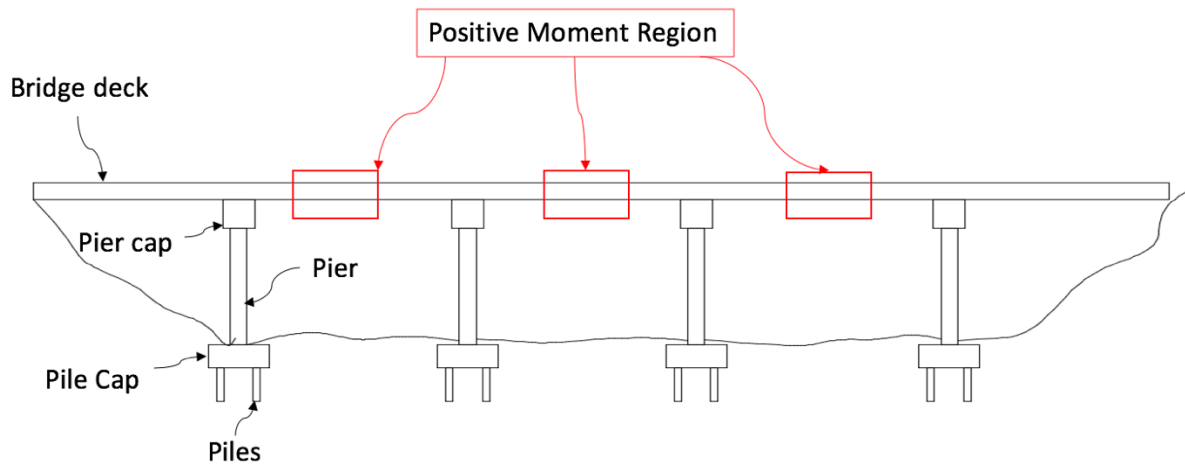


Fig 6.3: Graphic representation of positive moment regions on a typical bridge deck.

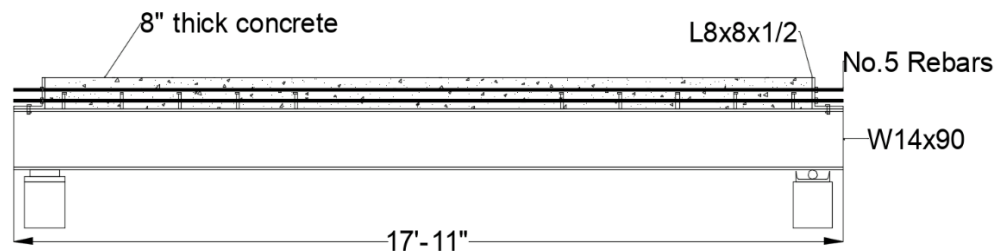


Fig 6.4: Detail of the lock collars at each end of the specimen.

The dimensions of the specimen were determined based on the dimensions of typical bridge decks in Illinois. Fig 6.5 shows the detail of the specimens through the side, top and cross-sectional views. The width of the specimen was 50", which was calculated as the effective flange width of the composite deck based on AASHTO (2017) specifications. To ensure that the

shrinkage will occur primarily along the longitudinal direction, the aspect ratio of the specimen was selected to be around 4:1 and therefore the deck length was determined to be 17'-11". The thickness and the reinforcing bar spacing at both top and bottom layers were design as per typical bridge deck designs in Illinois. The spacing of the top reinforcement of the 8"-thick deck was 12" and that of the bottom reinforcement was 11".

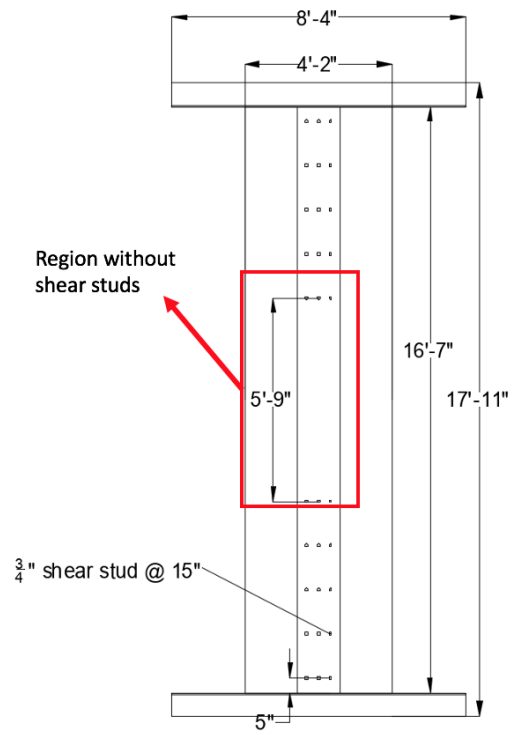
Fig 6.6 displays the girder elevation view of the actual bridge. The shear studs had different spacing at different regions of the bridge. In this study, a spacing of 15" between shear studs was selected as this type of shear stud distribution took up the longest region on the actual bridge. As the steel girder used on the actual bridge deck was a plate girder with a 14"-wide flange and 4-feet-tall web, it was considered unnecessary to make the steel girder as deep for this laboratory model. Therefore, a W14x90 model was selected to keep the flange width but with a shorter web depth.



(a)

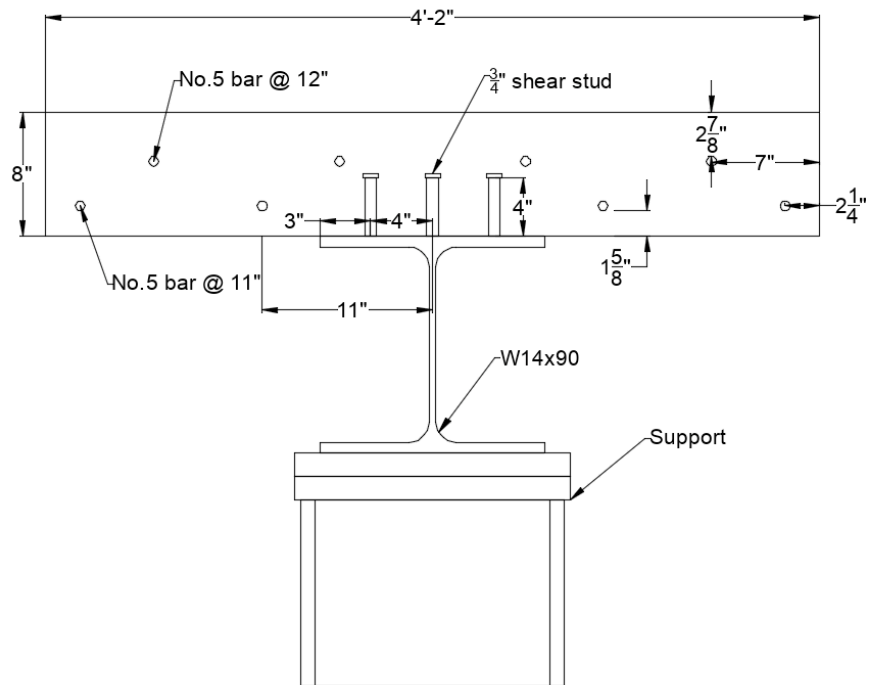
Fig 6.5: (a) Side view; (b) Plan view; (c) cross-sectional view; (d) reinforcement layout of the deck shrinkage specimen.

Fig 6.5 (cont.)



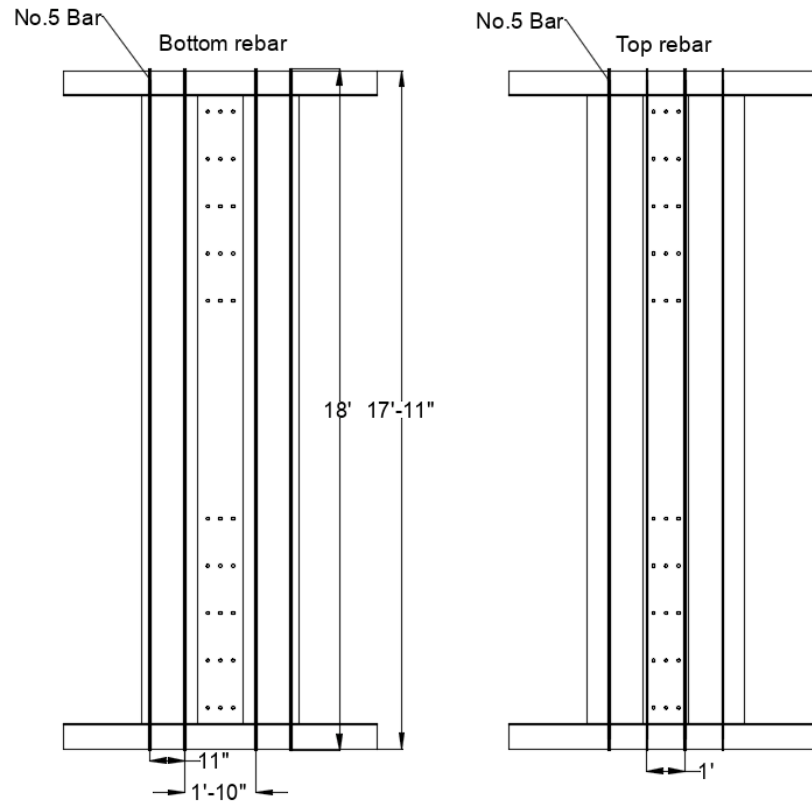
(b)

Fig 6.5 (cont.)



(c)

Fig 6.5 (cont.)



(d)

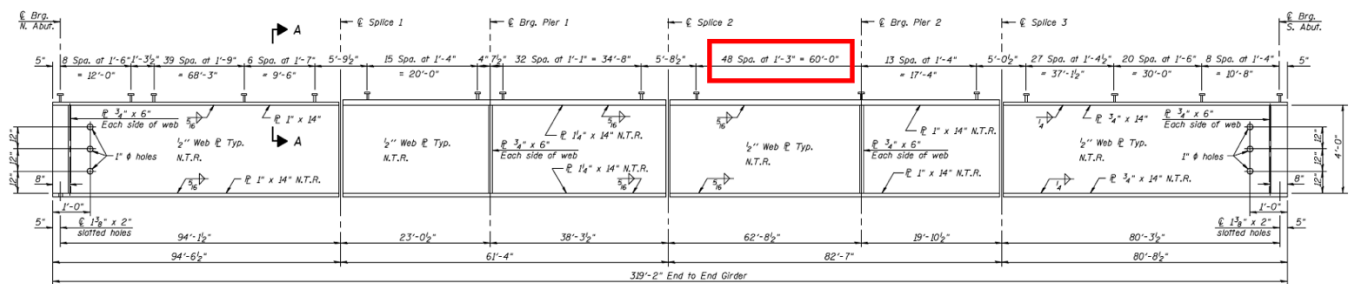


Fig 6.6: Shear stud spacing on actual bridge plans.

6.3.2 Specimen Fabrication

Fig 6.7 presents the different stages of constructing the formwork. The metal frame of the specimen, including the W14x90 steel girder, supports, angles at the ends, and the welded shear studs, were assembled first. The angles were bolted onto the steel girder. Then the metal frames for both specimens were placed next to each other at the designated space on the Newmark lab floor, shown in Fig 6.7a. The concrete deck forms were then constructed around the metal frames.

2"x4" lumbers were used as props to support the slab underneath the bottom of the slab, on top of which horizontal 2"x4" joists were placed to increase the gravity load capacity of the formwork, shown in Fig 6.7b. The formwork consisted of 3/4"-thick plywood used to form the bottom and sides of the deck. To strengthen both sides of the deck to prevent the side plywood formwork from bursting out, 2"x4" lumbers were screwed to the side plywood. In addition, to increase the stability of the formwork, long, transverse 2"x4" lumbers were screwed to the vertical supporting members and the side-strengthening members, as shown in Fig 6.7c. The completed formwork is presented in Fig 6.7d.



(a)



(b)

Fig 6.7: Images of (a) Metal frame; (b) support framing; (c) completed model; (d) top view of both completed specimen formworks.

Fig 6.7 (cont.)



(c)



(d)

After the formwork was completed, the 18-foot-long SEC and TEC7 bars were inserted through the predrilled holes on the angles and fastened using lock collars. To avoid the sagging of the bars without using large support objects that would occupy space in the specimen, nylon

threads were tied to the bars and wrapped around screws on the formwork. The threads were tightened until the bars were straight. Fig 6.8 displays the inserted bars tied with nylon threads.

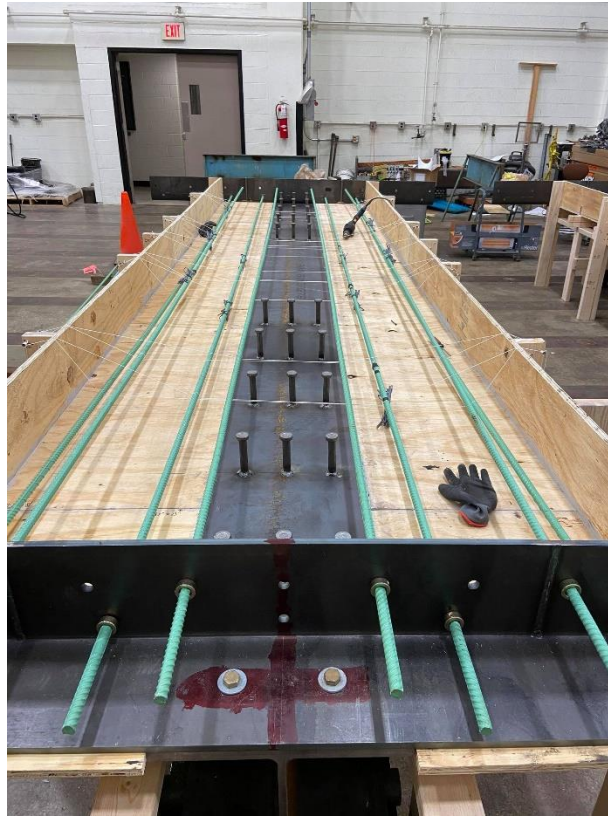


Fig 6.8: Inserted bars tied with nylon threads.

The concrete mix selected for casting the deck was a standard IDOT BS mix for bridge superstructure. The minimum 14-day strength specified by IDOT is 4.0 ksi. According to the strength data provided by the mix provider, the average 14-day strength of the provided BS mix was 5.8 ksi, which satisfied the IDO requirements. The slump of the mix was 4 inches and the air content was 5.5%, both meeting the IDOT specifications. The mix design is shown in Table 6.1 below.

Table 6.1: Mix design of the IDOT BS mix per cubic yard of concrete.

Materials	Amount
Fine Aggregate (FA 01)	1214 lb (SSD)
Coarse Aggregate (CM11)	1360 lb (SSD)
Coarse Aggregate (CM16)	453 lb (SSD)
Cement	460 lb
Class C Fly Ash	155 lb
Water	29.5 gal

In addition to the deck specimens, another six pull-out specimens were planned to be conducted using the same batch of concrete as the deck specimens, including two BLK, two SEC, and two TEC7 specimens. The purpose of conducting pull-out tests is to compare the bond-slip performance of the new TEC7 bar with SEC and BLK bars in a small scale, and to see whether there is any significant improvement on the slip resistance with regard to SEC and BLK bars. If the ratios of the slip resistance and peak strength of the TEC7 bar to those of SEC and BLK bar are much greater than the other TEC bars in the previous tests, it could be proved that TEC7 had a much greater potential in improving the bond-slip behaviors.

6.4 Instrumentation Plan

The instrumentation plan for this study was designed to investigate the transverse cracking of the deck slabs by monitoring the longitudinal deck shrinkage. Strain gages and Digital Image Correlation (DIC) (Rahman et al, 2018; Frosch et al, 2003; Brown et al, 2007; Gencturk et al, 2014; Salmanpour & Mojsilovic, 2013; Pickerd, 2013) were planned as means for monitoring the concrete deck shrinkage over time.

6.4.1 Strain Gages

Strain gages were placed on the bottom surface and both sides of the concrete deck as well as on the reinforcing bars (see Fig 6.9). For easier instrumentation and observation, strain gages are usually placed on the top of the concrete deck. However, since the DIC cameras will be capturing images of the deck's top surface, strain gages were installed on the bottom surface to avoid disturbing the DIC images. A total of 10 rebar strain gages (PL-60-11-5LJC-F) and 10 concrete strain gages (FLA-6-11-LJC) were ordered from Texas Measurements and used for each specimen. For the reinforcing bars, as displayed in Fig 6.9(a), strain gages were placed in a staggered manner to capture the shrinkage at various locations of concern on the deck, including the center, ends of the middle no-stud region, and the middle of the regions with studs. Since the ends of the specimen were constrained with angles, more strain gages were placed towards the center of the deck, where most longitudinal shrinkage was expected. On the bottom surface of the deck, the locations of the strain gages aligned with the reinforcing bars at the top and bottom layers in the transverse direction. Along the longitudinal direction, the strain gages were placed in five layers, which corresponded with layers 1, 2, 4, 6, and 7 on the reinforcing bars, as shown in Fig 6.9(b).

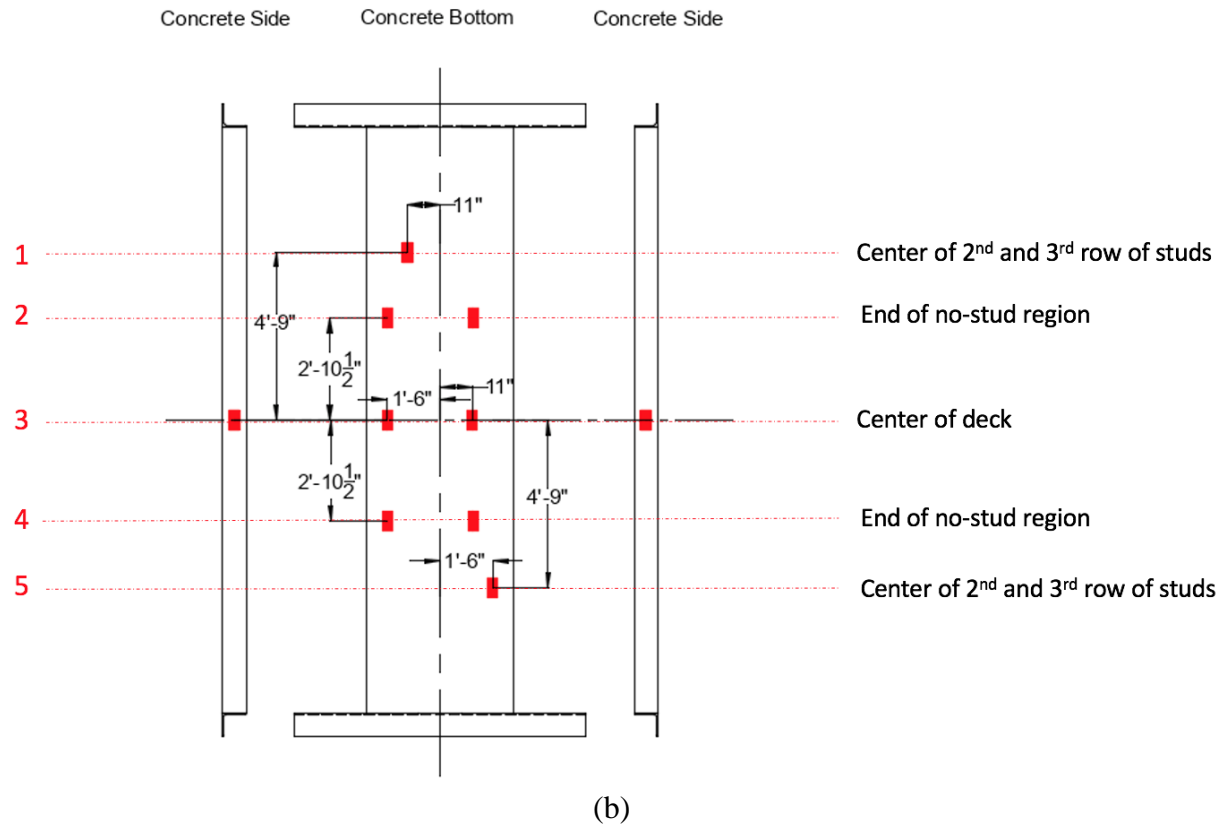
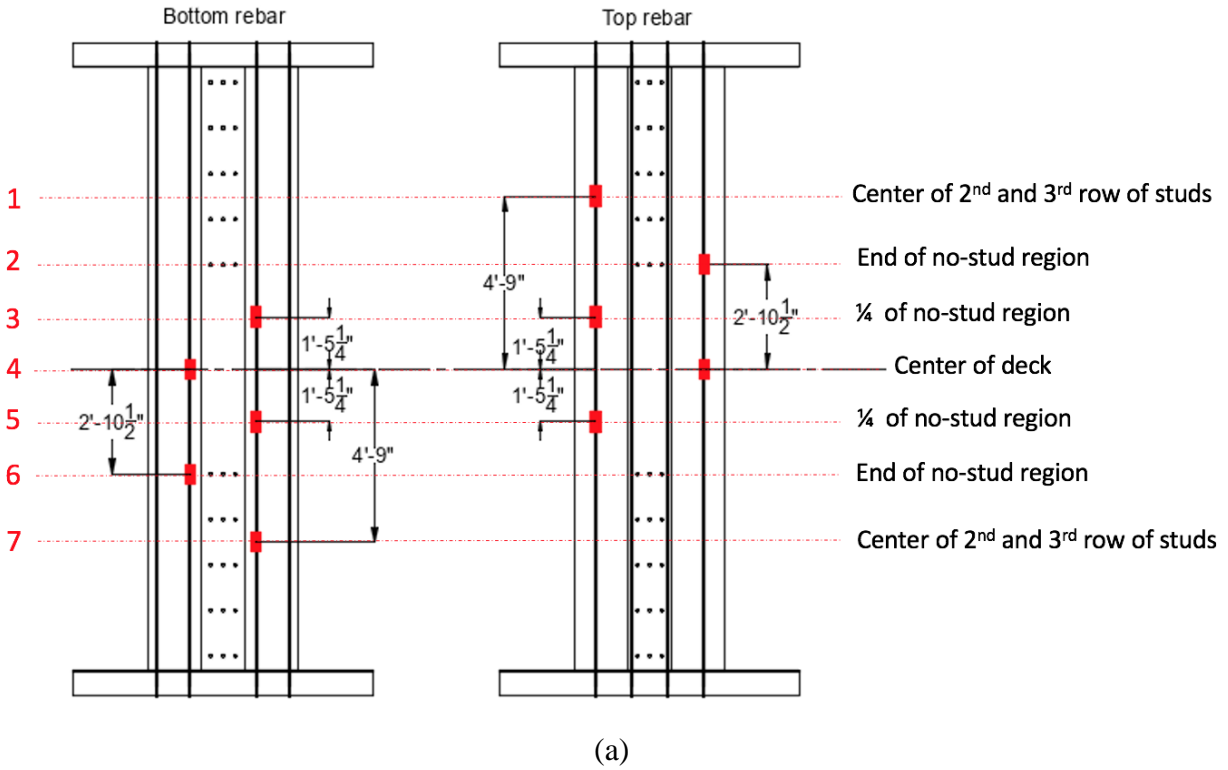


Fig 6.9: Strain gage layout on (a) top and bottom layers of rebar; (b) bottom of concrete deck.

A plan was set for using National Instruments (NI) data acquisition system to collect the strain data. The ends of the strain gages will be connected to a SXCI-1521B eight-channel module inserted into a SCXI-1001 chassis. Since there are a total of 40 strain gages, five modules are needed. The data collection settings are controlled with the NI MAX software.

6.4.2 Digital Image Correlation (DIC)

Strain gages can only record local strains at discrete locations across the deck. To obtain a more comprehensive picture of deck deformation, a plan for utilizing digital image correlation (DIC) to capture strain at the top surface of the deck was implemented. Random black dots (speckle dots) are applied on deck surface after painting it white. The DIC technique tracks the changes of patterned dots in small subsets, during the deformation of the deck through consecutively taken images (Correlated Solutions, 2020). The concept of DIC is shown in Fig 6.10. The advantage of this method is that it is a non-contact technique applicable for both small and large-scale deformations. And the strain contour of the entire surface can be obtained.

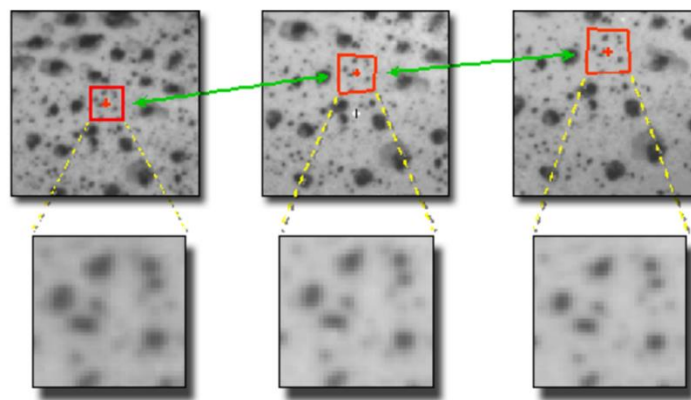


Fig 6.10: DIC point movement tracking concept (Correlated Solutions, 2020).

In this study, the DIC images is taken with a Nikon D90 looking down from above at the top deck surface of each specimen and the VIC-2D software developed by Correlated Solutions is used to post-process the images. The key factors which affect the accuracy of the results include camera & lighting, speckle dots pattern, and image resolution. The camera has to be right in front of the subject surface, in this case, right above the deck, with bright lighting preferably with no shadows. The camera field of view has to cover the critical dimensions of the measured sample. The application of the speckle dots and the white paint can also significantly affect the strain measurements since they are the input for the DIC post-processing. The white paint on the surface has to be matte-finished so that it does not reflect the light. Since a higher contrast between the speckle dots and their background is desirable, black speckle dots is typically applied.

The size, density, and pattern of the speckle dots are all extremely important for the accuracy of post-processing. From the “Application Note AN-1701: Speckle Pattern Fundamentals” issued by Correlated Solutions, 50% coverage of the black dots and consistent speckle sizes ideally 3-5 pixels are desirable. If the speckle dots are too large, the large point may cover the entire area of certain subsets, making everywhere in the region a good match and therefore preventing good correlation. If the speckle dots are too small, the resolution of the camera may not represent the specimen accurately, causing aliasing (Correlated Solutions, 2020). The resolution of the Nikon D90 camera is 4288x2848 pixels. Since the critical dimensions was determined to be 50”x75”, which covers the entire width of the specimen, shown in Fig 6.11. Speckle dots with a diameter of 0.1” are adopted, whose size was calculated using Equation 6.1 to be 5.70 pixels. The speckle dot size falls within the desired range of 5-8 pixels.

$$\text{Speckle dot size} = \frac{\text{Speckle dot diameter}}{\text{Critical dimension/camera resolution}} = 5.70 \text{ pixels} \quad (6.1)$$

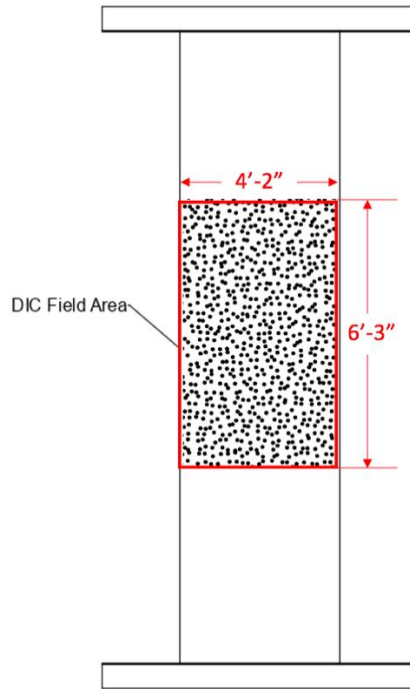


Fig 6.11: Critical dimension of the view field for DIC measurement.

Furthermore, the pattern of the speckle dots can neither be completely orthogonal nor be too randomized. Multiple methods are used to apply the speckle dots, including the VIC speckle dot kit by Correlated Solutions, spray paint, sharpie, and stencil. Since the speckle dot kit does not have the size used in this study, and both of the spray paint and sharpie methods are either too labor-intensive due to the large surface or hard to control, a stencil was created on a mylar sheet with 0.1" dots cut off by a laser cutter. The pattern of the dots was generated from a speckle dot generator software developed by Correlated Solutions.

6.4.3 Temperature Effect Simulation Test

Apart from the internal and external restraints, the ambient temperature cycles can also affect the deck cracking condition. At Illinois, the temperature difference between summer and winter can reach as high as 70 °F (Weather Atlas, 2020). This temperature change can cause different responses in the concrete and steel, resulting in significant internal tensile stress in the concrete deck. The behavior of concrete during the temperature change is complicated and vary with different mixtures (Johnson, 2005). Since concrete has a low thermal conductivity, the temperature inside and on the surface of the deck varies. The thermal expansion of concrete can vary with different factors such as aggregate type, cement content, water-cement ratio, and concrete age (Kosmatka et al, 2002). In addition, the thermal expansion coefficient of the steel girder can be much greater than that of concrete, causing a significant difference in strain between concrete and steel, which can result in transverse cracking. This test simulates this temperature difference between steel and concrete by heating the middle 6' of the steel girder of the specimen with a linear steel burner connected to a propane tank. Fig 6.12 displays a graphic representation of the heating test setup. The response of SEC and TEC7 reinforced specimens to the temperature effect will be monitored using strain gages and DIC.

The heating test will be conducted after the deck develops its full strength at 28 days after casting. The target temperature of the steel girder is 110 °F, which is close to the highest temperature in the hot summer. Two linear stainless burners each supported by a custom-made stand are placed at both sides of the web. The elevation of the steel burner matches the height of the center point of the girder's web depth. The two steel burners are connected to a propane tank with 12-foot-long hoses and a split tee adaptor. The heat from the propane tank can be adjusted with a thermostat. The temperature on the girder is continuously monitored with a handheld

infrared thermometer and the propane tank shall be immediately turned off after the girder web reaches the target temperature.

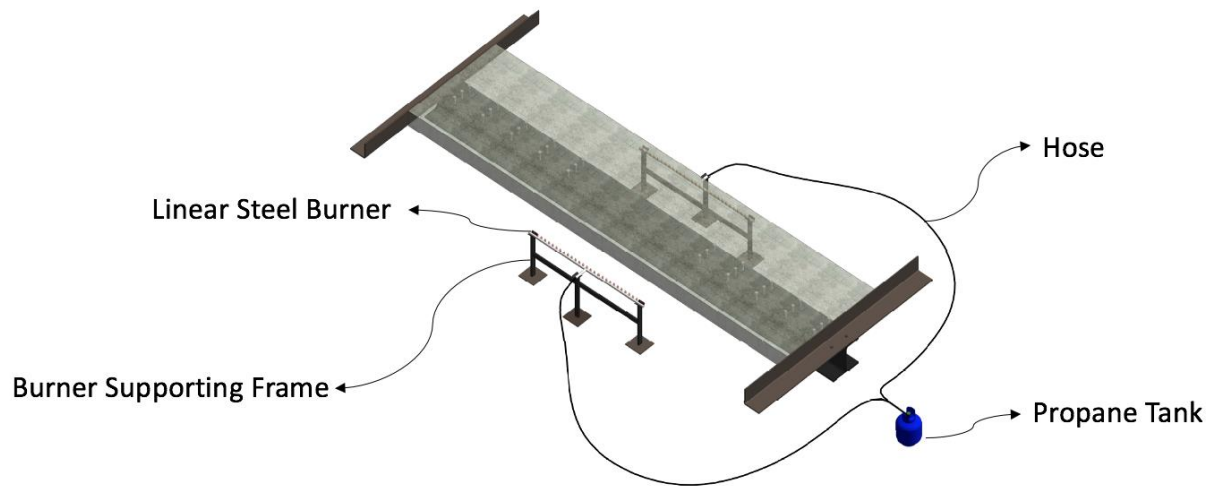


Fig 6.12: Graphic rendering of the heating test set-up.

Chapter 7: Conclusions

The goal of this study was to investigate the impact of applied roughness on epoxy-coated bars on the bond-slip behavior of the bars with concrete. First, a comparative study of the quantified surface roughness was conducted on BLK bars and six types of TEC bars with different surface roughness. Secondly, a comprehensive set of pull-out tests were also conducted in two phases to compare the bond strength and initial slip of TEC, BLK, and SEC bars with concrete of various compressive strengths. Then, several finite element models incorporating the interfacial properties between TEC bars and concrete using different approaches were developed and calibrated using experimental results from the pull-out tests. Finally, the design of a laboratory experiment was conducted to test two large-scale bridge deck specimens reinforced with SEC and TEC bar to study the difference in their long-term shrinkage. The main findings from this study are summarized as follows:

1. The TEC bars generally had R_a and R_z values 3-4 times that of the BLK bar, with TEC2 and TEC6 bars resulting in higher surface roughness than the other TEC bars.
2. Based on the quantified surface roughness and the pull-out test results, TEC2, TEC3, and TEC6 bars showed higher potential for improving the bond-slip behavior than the rest of the bars.
3. Examining the microstructure of the TEC bars surface revealed that, with the exception of TEC1 bar, all TEC bars coating surfaces incorporated voids of various sizes and amounts. These voids were proven to help with improving the initial slip resistance of TEC bars. However, they did not seem to have a major impact on the rebar's peak bond strength.

4. The method adopted in this study of using polymeric powder to add roughness to the surface of epoxy coated bars did not necessarily exhibit a major impact on increasing the peak bond strength of bars.
5. TEC bars generally manifested higher initial slip resistance than BLK and SEC bars with TEC2 and TEC6 bars showing the highest initial slip resistance compared to other TEC bars.
6. Both of the FE models of the pull-out specimens can accurately simulate the experimental results of the force versus slip. However, the computational time of the simplified FE model using the axial spring connectors to simulate the concrete-bar interface was significantly less than that of the detailed FE model using cohesive behaviors. That said, only the detailed FE model was able to adequately capture the stress distribution at the coating-steel and coating-concrete interfaces in addition to the damage progression in the coating layer and the surrounding concrete.
7. The calibrated curves of the force versus relative displacement for the SEC and TEC bars from the simplified FE model with the axial spring connectors demonstrated that in the nonlinear elastic stage, the slip resistance of the TEC bar was significantly higher than that of the SEC bar.
8. The FE model of the simply-supported beam subjected to four-point-bending adequately captured the longitudinal and shear stress distribution on the TEC bar and the concrete, as well as the crack pattern of the concrete when the point load was imposed on different locations along the beam.
9. The development length of the TEC bar obtained from numerical modelling was approximately 38% less than the analytical values calculated based on ACI 318-19

(2019) and 18% less than the analytical value based on AASHTO (2017) for the SEC bar. For the BLK bar, the numerical value was also slightly less than the analytical development length calculated from ACI318-19 (2019) and was about 22.5% more than the analytical value from AASHTO (2017). Overall, it could be demonstrated that the TEC bar had potential in decreasing the amount of rebars needed to satisfy the requirement of development length compared with the SEC bars.

References

American Association of State Highway and Transportation Officials. (2017). *AASHTO LRFD bridge design specifications*.

Abaqus, F. E. A. (2014). Analysis User's Manual 6.14. *Dassault Systemes Simulia Corp., Providence, RI*.

ACI Committee, & International Organization for Standardization. (2019). Building code requirements for structural concrete (ACI 318-19) and commentary. American Concrete Institute.

Al-Zahrani, M. M., Al-Dulaijan, S. U., Ibrahim, M., Saricimen, H., & Sharif, F. M. (2002). Effect of waterproofing coatings on steel reinforcement corrosion and physical properties of concrete. *Cement and Concrete Composites*, 24(1), 127-137.

American Concrete Institute. Committee 440. (2015). Guide for the Design and Construction of Concrete Reinforced with FRP Bars: ACI 440.1 R-15. *American Concrete Institute*.

American Society of Civil Engineers. (2017). *Bridges*. 2017 Infrastructure Report Card. <https://www.infrastructurereportcard.org/cat-item/bridges/>. (Accessed 22 July, 2020).

American Society of Civil Engineers. (2017). *What Makes a Grade?*. 2017 Infrastructure Report Card. <https://www.infrastructurereportcard.org/making-the-grade/what-makes-a-grade/>. (Accessed 22 July, 2020)

American Society of Mechanical Engineers. (2010). *Surface Texture: (surface Roughness, Waviness, and Lay): ASME B46. 1-2009*. American Society of Mechanical Engineers.

ASTM International. (2017). *ASTM D3359-17: Standard Test Methods for Rating Adhesion by Tape Test*, West Conshohocken, PA: American Society for Testing and Materials.

ASTM International. (2018). *ASTM D6677-18: Standard Test Method for Evaluating Adhesion by Knife*. West Conshohocken, PA: American Society for Testing and Materials.

ASTM International. (2015). *ASTM D6943-15: Standard Practice for Immersion Testing of Industrial Protective Coatings and Linings*, West Conshohocken, PA: American Society for Testing and Materials.

Basham, K (2014) Plastic Shrinkage Cracks [Online Image] for Construction Pros. <https://www.forconstructionpros.com/concrete/equipment-products/article/11487540/plastic-shrinkage-cracking>.

Bentz, D. P., & Jensen, O. M. (2004). Mitigation strategies for autogenous shrinkage cracking. *Cement and Concrete Composites*, 26(6), 677-685.

Berg, A. C., Bank, L. C., Oliva, M. G., & Russell, J. S. (2006). Construction and cost analysis of an FRP reinforced concrete bridge deck. *Construction and Building Materials*, 20(8), 515-526.

Bertolini, L., Elsener, B., Pedferri, P., Redaelli, E., & Polder, R. (2004). *Corrosion of steel in concrete* (Vol. 392). Weinheim, Germany: Wiley-Vch.

Bhushan, B. (2000). *Modern tribology handbook, two volume set*. CRC press.

Brown, M., Sellers, G., Folliard, K. J., & Fowler, D. W. (2001). *Restrained shrinkage cracking of concrete bridge decks: State-of-the-Art Review* (No. FHWA/TX-0-4098-1).

Brown, M. D., Smith, C. A., Sellers, J. G., Folliard, K. J., & Breen, J. E. (2007). Use of alternative materials to reduce shrinkage cracking in bridge decks. *ACI Materials Journal*, 104(6), 629.

Cheng, T. T., & Johnson, D. W. (1985). Incidence assessment of transverse cracking in bridge decks: Construction and material consideration. *North Carolina State University*, 85-002.

Choi, O. C., Choi, H. J., & Hong, G. H. (2010). Bearing angle model for bond of reinforcing bars to concrete. *Fracture mechanics of concrete and concrete structures*, 807-810.

Choi, O. C., Hadje-Ghaffari, H., Darwin, D., & McCabe, S. L. (1991). Bond of epoxy- coated reinforcement: bar parameters. American Concrete Institute.

Cleary, D. B., & Ramirez, J. A. (1991). Bond strength of epoxy-coated reinforcement. *Materials Journal*, 88(2), 146-149.

Collepardi, M., Borsoi, A., Collepardi, S., Olagot, J. J. O., & Troli, R. (2005). Effects of shrinkage reducing admixture in shrinkage compensating concrete under non-wet curing conditions. *Cement and Concrete Composites*, 27(6), 704-708.

Combrinck R., Steyl, L. & Boshoff, W. P. (2018). *Crack pattern linked to steel reinforcement layout*[Photograph]. In R. Combrinck, L. Steyl, & W. P. Boshoff , Interaction between settlement and shrinkage cracking in plastic. *Construction and Building Materials*, 185, 1-11.

Correlated Solutions. (2017). Application Note AN-1701 Speckle Pattern Fundamentals. *línea*]. Available: <https://www.correlatedsolutions.com/support/index.php>.

Correlated Solutions. (2020). *Principle of Digital Image Correlation*. <https://www.correlatedsolutions.com/digital-image-correlation/>

Crack caused by restraint to drying shrinkage [Online Image]. (n.d.). The Concrete Society. <http://www.concrete.org.uk/fingertips-nuggets.asp?cmd=display&id=22>

DalSoglio, M. S. (2017). Investigation of Bridge Decks. *Montana Department of Transportation, Northbrook, Illinois*.

Dybeł, P., & Furtak, K. (2017). The influence of high-strength concrete–rebars bond conditions on the mechanism of its failure. *Magazine of Concrete Research*, 69(4), 163-174.

EPOXY INTEREST GROUP. (n.d.). *HISTORY OF EPOXY-COATED REBAR*. Retrieved September 13, 2020. from <http://www.epoxyinterestgroup.org/about/history-of-epoxy-coated-rebar/>

Fernandes, F., Manari, S., Aguayo, M., Santos, K., Oey, T., Wei, Z., ... & Sant, G. (2014). On the feasibility of using phase change materials (PCMs) to mitigate thermal cracking in cementitious materials. *Cement and Concrete Composites*, 51, 14-26.

Folliard, K., Smith, C., Sellers, G., Brown, M., & Breen, J. E. (2003). *Evaluation of alternative materials to control drying-shrinkage cracking in concrete bridge decks* (No. FHWA/TX-04/0-4098-4,).

Frosch, R. J., Blackman, D. T., & Radabaugh, R. D. (2003). *Investigation of bridge deck cracking in various bridge superstructure systems* (No. FHWA/IN/JTRP-2002/25,).

Gadelmawla, E. S., Koura, M. M., Maksoud, T. M. A., Elewa, I. M., & Soliman, H. H. (2002). Roughness parameters. *Journal of materials processing Technology*, 123(1), 133-145.

Gencturk, B., Hossain, K., Kapadia, A., Labib, E., & Mo, Y. L. (2014). Use of digital image correlation technique in full-scale testing of prestressed concrete structures. *Measurement*, 47, 505-515.

Goyal, A., Pouya, H. S., Ganjian, E., & Claisse, P. (2018). A review of corrosion and protection of steel in concrete. *Arabian Journal for Science and Engineering*, 43(10), 5035-5055.

Güneyisi, E., Gesoğlu, M., & Özbay, E. (2010). Strength and drying shrinkage properties of self-compacting concretes incorporating multi-system blended mineral admixtures. *Construction and Building Materials*, 24(10), 1878-1887.

Hadidi, R., & Saadeghvaziri, M. A. (2005). Transverse cracking of concrete bridge decks: State-of-the-art. *Journal of Bridge Engineering*, 10(5), 503-510.

Harajli, M., Hamad, B., & Karam, K. (2002). Bond-slip response of reinforcing bars embedded in plain and fiber concrete. *Journal of Materials in Civil Engineering*, 14(6), 503-511.

Hognestad, E., Hanson, N. W., & McHenry, D. (1955, December). Concrete stress distribution in ultimate strength design. In *Journal Proceedings* (Vol. 52, No. 12, pp. 455-480).

Hopper, T., Manafpour, A., Warn, G., Rajabipour, F., Morian, D., & Jahangirnejad, S. (2015). *Bridge deck cracking: effects on in-service performance, prevention, and remediation* (No.

FHWA-PA-2015-006-120103). Pennsylvania. Dept. of Transportation. Bureau of Planning and Research.

Ibrahim, M., Al-Gahtani, A. S., Maslehuddin, M., & Dakhil, F. H. (1999). Use of surface treatment materials to improve concrete durability. *Journal of Materials in Civil Engineering*, 11(1), 36-40.

Inspection Light Microscope [Online image]. (2020). The Imaging Technology Group. https://itg.beckman.illinois.edu/microscopy_suite/equipment/details/inspection-light-microscope

ISO 16610-21. (2011). Geometrical product specifications (GPS)—filtration—Part 21: linear profile filters: Gaussian filters. *International Organization for Standardization*.

ISO, E. (1996). 4288—Geometrical product specifications (GPS)—surface texture: profile method—rules and procedures for the assessment of surface texture. *International Organization for Standardization: Geneva, Switzerland*.

Issa, C. A., & Masri, O. (2015). Numerical simulation of the bond behavior between concrete and steel reinforcing bars in specialty concrete. *International Journal of Civil and Environmental Engineering*, 9(6), 767-774.

Johnson, J. K. (2005). *Concrete bridge deck behavior under thermal loads* (Doctoral dissertation, Montana State University-Bozeman, College of Engineering).

Johnston, D. W., & Zia, P. (1982). *Bond characteristics of epoxy coated reinforcing bars* (No. FHWA/NC/82-002 Final Rpt.).

Kabir, M. R., & Islam, M. M. (2014). Bond stress behavior between concrete and steel rebar: Critical investigation of pull-out test via Finite Element Modeling. *International Journal of Civil and Structural Engineering*, 5(1), 80-90.

Kassem, C., Farghaly, A. S., & Benmokrane, B. (2011). Evaluation of flexural behavior and serviceability performance of concrete beams reinforced with FRP bars. *Journal of Composites for Construction*, 15(5), 682-695.

Kepler, J. L., Darwin, D., & Locke Jr, C. E. (2000). *Evaluation of corrosion protection methods for reinforced concrete highway structures*. University of Kansas Center for Research, Inc.

Khalefa, R., & Kaska, S. E. (2017) Friction Power Modeling As A Function Of Diesel Engine Speed And Geometry With Predicting Their Effects On Some Performance Parameters. *Journal of Engineering Sciences* 8(1): 55-64.

Kim, K. H. E., & Andrawes, B. (2019). Exploratory Study on Bond Behavior of Textured Epoxy-Coated Reinforcing Bars. *Journal of Materials in Civil Engineering*, 31(8), 04019151.

- Kim, G. M., Yang, B. J., Ryu, G. U., & Lee, H. K. (2016). The electrically conductive carbon nanotube (CNT)/cement composites for accelerated curing and thermal cracking reduction. *Composite Structures*, 158, 20-29.
- Klemczak, B. A. (2014). Modeling thermal-shrinkage stresses in early age massive concrete structures—comparative study of basic models. *Archives of Civil and Mechanical Engineering*, 14, 721-733.
- Klemczak, B., & Knoppik-Wróbel, A. (2011). Early age thermal and shrinkage cracks in concrete structures—description of the problem. *Architecture-Civil Engineering-Environment*, 4(2), 35-48.
- Kobayashi, K., & Takewaka, K. (1984). Experimental studies on epoxy coated reinforcing steel for corrosion protection. *International Journal of Cement Composites and Lightweight Concrete*, 6(2), 99-116.
- Kosmatka, S. H., Kerkhoff, B., & Panarese, W. C. (2002). *Design and control of concrete mixtures* (Vol. 5420, pp. 60077-1083). Skokie, IL: Portland Cement Association.
- Krauss, P. D., & Rogalla, E. A. (1996). *Transverse cracking in newly constructed bridge decks* (No. Project 12-37 FY'92).
- Lin, H., Zhao, Y., Feng, P., Ye, H., Ozbolt, J., Jiang, C., & Yang, J. Q. (2019). State-of-the-art review on the bond properties of corroded reinforcing steel bar. *Construction and Building Materials*, 213, 216-233.
- Lindquist, W. D., Darwin, D., Browning, J., & Miller, G. G. (2006). Effect of cracking on chloride content in concrete bridge decks. American Concrete Institute.
- Luccioni, B. M., López, D. E., & Danesi, R. F. (2005). Bond-slip in reinforced concrete elements. *Journal of structural engineering*, 131(11), 1690-1698.
- Lundgren, K. (2005). Bond between ribbed bars and concrete. Part 1: Modified model. *Magazine of concrete research*, 57(7), 371-382.
- Lutz, L. A., & Gergely, P. (1967, November). Mechanics of bond and slip of deformed bars in concrete. In *Journal Proceedings* (Vol. 64, No. 11, pp. 711-721).
- Markeset, G., Rostam, S., & Klinghoffer, O. (2006). *Guide for the use of stainless steel reinforcement in concrete structures*. Norwegian Building Research Institute.
- Mathey, R. G., & Clifton, J. R. (1976). Bond of coated reinforcing bars in concrete. *Journal of the Structural Division*, 102(ASCE# 11855).
- McDonald, D. (2010). Do epoxy-coated bars provide cost-effective corrosion protection. *Epoxy Interest Group of CRSI*, (847), 517-1200.

Murcia-Delso, J., Stavridis, A., & Shing, B. (2011, May). Modeling the bond-slip behaviour of confined large-diameter reinforcing bars. In *III ECCOMAS thematic conference on computational methods in structural dynamics and earthquake engineering*.

Otieno, M. B., Alexander, M. G., & Beushausen, H. D. (2010). Corrosion in cracked and uncracked concrete—influence of crack width, concrete quality and crack reopening. *Magazine of Concrete Research*, 62(6), 393-404.

Pereira, H. F. S. G., Cunha, V. M., & Sena-Cruz, J. (2015). Numerical simulation of galvanized rebars pullout. *Frattura ed Integrità Strutturale*, 9(31), 54-66.

Pickerd, V. (2013). *Optimisation and validation of the ARAMIS digital image correlation system for use in large-scale high-strain-rate events* (No. DSTO-TN-1203). DEFENSE SCIENCE AND TECHNOLOGY ORGANIZATION VICTORIA (AUSTRALIA) MARITIME PLATFORMS DIV.

Purvis, R., Babei, K., Udani, N., Qanbari, A., & Williams, W. (1995). Premature cracking of concrete bridge decks: Causes and methods of prevention. In *Proceedings of the 4th International Bridge Engineering Conference, Washington, DC*.

Rahman, M., Chen, Y., Lindquist, W., Ibrahim, A., & Hindi, R. (2018, April). Mitigation of shrinkage cracking in bridge decks using Type-K cement. In *Structures Congress 2018: Bridges, Transportation Structures, and Nonbuilding Structures* (pp. 125-132). Reston, VA: American Society of Civil Engineers.

RILEM, T. (1994). RC 6 Bond test for reinforcement steel. 2. Pull-out test, 1983. *RILEM recommendations for the testing and use of constructions materials*, 218-220.

Rubinsky, I. A., & Rubinsky, A. (1954). A preliminary investigation of the use of fibre-glass for prestressed concrete. *Magazine of concrete research*, 6(17), 71-78.

Salmanpour, A., & Mojsilovic, N. (2013, December). Application of Digital Image Correlation for strain measurements of large masonry walls. In *Conference Proceedings. APCOM & ISCM, Singapore*.

Šavija, B., & Schlangen, E. (2016). Use of phase change materials (PCMs) to mitigate early age thermal cracking in concrete: Theoretical considerations. *Construction and Building Materials*, 126, 332-344.

Schmitt, T. R., & Darwin, D. (1999). Effect of material properties on cracking in bridge decks. *Journal of Bridge Engineering*, 4(1), 8-13.

Sherman, Matthew R., Carrasquillo, R. L., and Fowler, D. W. (1993). Field Evaluation of Bridge Corrosion Protection Measures. *Report No. FHWA/TX-93+1300-1*, Texas Department of Transportation, Austin, Texas.

Sonnenschein, R., Gajdosova, K., & Holly, I. (2016). FRP composites and their using in the construction of bridges. *Procedia engineering*, 161, 477-482.

Specifications, G. P. (1996). Surface Texture: Profile Method—Nominal Characteristics of Contact (Stylus) Instruments. *Standard ISO*, 3274.

Standard, I. S. O. (1997). Geometrical Product Specifications (GPS)—Surface texture: Profile method—Terms, definitions and surface texture parameters. *Int Organ Stand*, 4287.

Standard Specification for Epoxy-Coated Steel Reinforcing Bars. (2019). *Annual Book of ASTM Standards*, 01.04.

Standard Test Method for Pull-Off Strength of Coatings Using Portable Adhesion Testers. (2017). *Annual Book of ASTM Standards*, 06.02.

Stewart, C. F., and Gunderson, B. J. (1969). Factors affecting the durability of concrete bridge decks. *Interim Rep. No. 2*, Research and Development Section of Bridge Department, California Department of Transportation, Sacramento, California.

Tang, C. W. (2015). Local bond stress-slip behavior of reinforcing bars embedded in lightweight aggregate concrete. *Comput. Concrete*, 16(3), 449-466.

Texas Department of Transportation. (1995). *Test Method Tex-739-I: Sampling and Testing Epoxy Coated Reinforcing Steel*. Manual of Testing Procedures. Vol. III. Texas Department of Transportation. Materials and Test Division. Austin: TxDOT

Treece, R. A., & Jirsa, J. O. (1989). Bond strength of epoxy-coated reinforcing bars. *Materials Journal*, 86(2), 167-174.

Vaca-Cortés, E., Lorenzo, M. A., Jirsa, J. O., Wheat, H. G., & Carrasquillo, R. L. (1998). Adhesion testing of epoxy coating. *Center for transportation Research, Research Report*, (1265-6), 1-129.

Wan, B. (2014). Using fiber-reinforced polymer (FRP) composites in bridge construction and monitoring their performance: an overview. In *Advanced composites in bridge construction and repair* (pp. 3-29). Woodhead Publishing.

Weather Atlas. (2020). *Monthly weather forecast and climate Illinois, USA*. Retrieved November 19, 2020. from <https://www.weather-us.com/en/illinois-usa-climate#:~:text=Summers%20tend%20to%20be%20humid,extreme%20temperatures%20during%20a%20heatwave.&text=Low%20temperatures%20in%20winter%20often,latter%20part%20of%20the%20season>

Weyers, R. E., & Cady, P. D. (1987). Deterioration of concrete bridge decks from corrosion of reinforcing steel. *Concrete International*, 9(1), 15-20.

Williams, A., Markandeya, A., Stetsko, Y., Riding, K., & Zayed, A. (2016). Cracking potential and temperature sensitivity of metakaolin concrete. *Construction and Building Materials*, 120, 172-180.

Wu, L., Farzadnia, N., Shi, C., Zhang, Z., & Wang, H. (2017). Autogenous shrinkage of high performance concrete: A review. *Construction and Building Materials*, 149, 62-75.

Xing, G., Zhou, C., Wu, T., & Liu, B. (2015). Experimental study on bond behavior between plain reinforcing bars and concrete. *Advances in Materials Science and Engineering*, 2015.

Xiong, Y., Wang, K., Liu, Z., & Yang, Z. (n.d.). Effect of coating thickness on bond behaviors of polymer cement coated plain steel bar with concrete and finite element modeling. *Open Civil Engineering Journal*, 10, 571–577.

Yuan, J., Lindquist, W. D., Darwin, D., & Browning, J. (2015). Effect of slag cement on drying shrinkage of concrete. American Concrete Institute.

Zhang, W., Zakaria, M., & Hama, Y. (2013). Influence of aggregate materials characteristics on the drying shrinkage properties of mortar and concrete. *Construction and Building Materials*, 49, 500-510.

Zinelis, S., Eliades, T., Eliades, G., Makou, M., & Silikas, N. (2005). Comparative assessment of the roughness, hardness, and wear resistance of aesthetic bracket materials. *Dental Materials*, 21(9), 890-894.

[Untitled image of stainless steel reinforcing bars]. (2017). Concrete Construction. https://www.concreteconstruction.net/how-to/materials/stainless-steel-fabrication-standard_o

[Untitled image of speckle dots for digital image correlation]. Correlated Solutions. <https://www.correlatedsolutions.com/digital-image-correlation/>

[Untitled image of concrete deck coating being applied]. Master Builders Solution. <https://www.master-builders-solutions.com/en-us/products/deck-coatings>

[Untitled image of galvanized steel reinforcing bars]. International Zinc Association. <http://zinc.org.in/zinc-uses/cgr/>

Appendix A: Rebar Surface Roughness Parameter Values

This appendix contains tables of the numerical values of the roughness parameters discussed in Chapter 3 for both phase I and phase II studies. The measurements for the coating thickness and the opening width for the coating adhesion strength test are also included in this appendix. Tables A.1-A.3 present the average values of 2-D and 3-D roughness parameters for TEC and BLK bars in Phase I study. Table A.4-A.5 displays the measured coating thickness for No.5 and No.8 SEC and TEC1 bars. Table A.6-A.7 presents the average values of 2-D and 3-D roughness parameters for No.5 TEC1-6 and BLK bars in Phase II study. Table A.8 shows the measured opening widths of No.5 TEC1-3 and SEC bars for the coating adhesion strength test.

Table A.1: Average values of the 2-D amplitude roughness parameters R_a , R_z , and R_{ku} of TEC1 and BLK bars in Phase I study.

$\times 10^{-4}$ in.	No.5 TEC1	No.8 TEC1	No.5 BLK	No.8 BLK
R_a	15.20	14.60	1.55	3.30
R_z	79.70	78.70	8.41	18.20
R_{ku}	2.68	2.69	1.73	2.96

Table A.2: Average values of the 2-D spacing roughness parameters HSC and R_{sm} of No.5 and No.8 TEC1 bars in Phase I study.

	No.5 TEC1	No.8 TEC1
HSC	6.04	5.89
R_{sm}	0.45	0.46

Table A.3: Average values of the 2-D and 3-D roughness parameters R_a , S_a , R_z , and S_z of No.5 and No.8 TEC1 bars in Phase I study.

$\times 10^{-3}$ in.	No.5 TEC1	No.8 TEC1
R_a	1.52	1.46
S_a	1.88	1.49
R_z	7.97	7.87
S_z	15.28	12.83

Table A.4: Measurements of coating thickness for No.5 SEC and TEC1 bars.

		Coating thickness ($\times 10^{-3}$ in)					
Measurement Location		1	2	3	4	5	Average
No.5	SEC	11.17	6.61	17.36	6.06	11.09	10.46
	TEC green	10.79	11.94	8.19	9.72	12.76	10.68
	TEC1 overall	16.35	19.82	12.45	16.97	16.10	16.34

Table A.5: Measurements of coating thickness for No.8 SEC and TEC1 bars.

Measurement Location		Coating thickness ($\times 10^{-3}$ in)										
		1	2	3	4	5	6	7	8	9	10	Avg
No.8	SEC	11.02	17.68	8.45	11.09	8.18	6.94	15.09	8.00	13.12	18.97	11.85
	TEC green	7.81	9.81	9.44	11.24	9.99	8.96	13.03	9.53	10.09	10.45	10.03
	TEC overall	17.78	13.61	17.28	17.20	16.92	16.08	19.77	14.50	15.08	14.70	16.29

Table A.6: Average values of the 2-D roughness parameters R_a and R_z of the No.5 TEC and BLK bars in Phase II study.

$\times 10^{-3}$ in.	TEC1	TEC2	TEC3	TEC4	TEC5	TEC6	TEC7	BLK
R_a	1.46	1.76	1.69	1.66	1.42	1.83	2.80	0.33
R_z	7.87	9.67	9.51	7.77	6.97	8.93	13.70	1.82

Table A.7: Average values of the 3-D roughness parameters S_a and S_z of the No.5 TEC bars in Phase II study.

$\times 10^{-3}$ in	TEC1	TEC2	TEC3	TEC4	TEC5	TEC6	TEC7
S_a	1.76	1.60	1.60	2.42	2.43	3.12	2.93
S_z	14.95	15.28	13.88	20.12	18.73	24.22	27.21

Table A.8: Measurements of opening width of No.5 SEC and TEC1-3 bars for the adhesion strength test

Opening Width (x10 ⁻³ in.)		Location	TEC1-1	TEC1-2	TEC2-1	TEC2-2	TEC3-1	TEC3-2	SEC-1	SEC-2
S1	RIB1	1	9.35	11.79	15.30	26.12	22.81	6.72	37.67	30.45
		2	9.15	12.42	11.24	22.11	17.26	13.94	31.10	19.41
	RIB2	1	16.71	12.93	16.36	28.26	35.58	11.90	35.44	22.68
		2	18.81	20.09	19.59	29.52	6.61	19.22	28.35	14.14
	RIB3	1	14.36	10.09	20.03	16.72	12.14	6.64	34.24	9.61
		2	6.61	12.58	14.56	30.91	8.53	8.63	17.10	10.08
	RIB4	1	7.39	8.97	37.80	36.25	12.19	7.26	25.19	24.31
		2	17.28	9.15	9.69	9.03	2.56	8.85	13.01	32.62
S2	RIB1	1	14.22	16.01	30.79	10.24	4.96	28.11	26.95	23.41
		2	11.57	8.10	21.53	11.46	3.24	22.07	18.51	29.61
	RIB2	1	11.69	14.04	11.31	17.34	7.43	5.28	23.81	28.28
		2	16.34	15.56	19.31	15.82	4.64	12.03	17.25	25.51
	RIB3	1	6.94	7.73	17.80	21.11	10.97	9.89	34.08	19.82
		2	10.18	12.88	39.03	21.28	24.34	9.07	21.24	26.82
	RIB4	1	10.88	4.04	34.24	33.72	24.52	4.33	25.49	35.45
		2	10.46	9.74	33.01	12.86	16.42	12.31	19.74	35.83
S3	RIB1	1	8.58	16.52	8.58	16.37	6.87	3.22	25.73	29.92
		2	16.33	15.50	7.33	17.88	21.53	7.80	28.98	32.97
	RIB2	1	14.30	6.48	23.47	27.81	14.23	6.87	32.59	48.43
		2	5.15	14.93	20.77	13.09	14.36	23.25	25.91	15.90
	RIB3	1	9.11	11.94	26.75	14.30	21.00	17.01	22.82	31.78
		2	9.97	8.95	14.54	9.76	25.80	24.01	22.42	12.65
	RIB4	1	18.72	11.90	14.71	18.50	8.98	19.16	29.47	21.09
		2	11.46	4.92	22.79	20.45	17.37	16.54	8.80	35.02
Bar Average			11.90	11.55	20.44	20.04	14.35	12.67	25.25	25.66
Pack Average			11.73		20.24		13.51		25.45	

Appendix B: Pull-Out Test Data

This Appendix presents the numerical values of the peak strength and secant slope of each type of the bar in three batches in Phase II study. Table B.1 displays the peak strength of different types of bars in all three batches while Table B.2 displays the secant slope values at three different slip ranges for each type of bar in all three batches.

Table B.1: Peak strength of each bar type for all three batches in Phase II study.

Peak Strength (kip)	Batch 1	Batch 2	Batch 3
BLK	18.07	22.38	24.33
SEC	15.61	23.40	23.63
TEC1	16.57	18.05	21.69
TEC2	18.56	15.27	24.83
TEC3	19.22	21.79	23.36
TEC4	14.72	19.58	22.61
TEC5	15.38	19.27	22.47
TEC6	14.98	19.86	23.39

Table B.2: Secant slope values of each bar type in all three batches at three different ranges of slip in Phase II study.

Slip Range	Secant Slope ($\times 10^4$ kip/in)								
	0-0.0001"			0-0.0014"			0-0.0028"		
Batch	Batch 1	Batch 2	Batch 3	Batch 1	Batch 2	Batch 3	Batch 1	Batch 2	Batch 3
BLK	3.44	2.80	4.31	0.32	0.33	0.66	0.19	0.27	0.53
SEC	1.66	0.35	2.75	0.21	0.18	0.42	0.16	0.16	0.35
TEC1	3.91	5.59	5.51	0.72	0.58	0.85	0.37	0.35	0.47
TEC2	4.11	8.11	5.90	0.69	1.06	1.30	0.38	N/A	0.72
TEC3	4.00	3.93	6.08	0.79	0.76	1.11	0.44	0.47	0.64
TEC4	3.69	0.93	5.76	0.76	1.12	1.20	0.40	0.60	0.65
TEC5	2.08	3.61	6.09	0.68	0.95	1.13	0.38	0.53	0.62
TEC6	5.07	8.39	7.47	0.78	1.08	1.36	0.41	0.59	0.73